Micropulse Lidar Observations of Free Tropospheric Aerosols over the Atmospheric Radiation Measurement site at Barrow, Alaska

By

Ramaswamy Tiruchirapalli

RECOMMENDED: _____

_____

_____

_____

_____
Advisory Committee Chair

_____
Head, Program in Atmospheric Sciences

APPROVED: _____
Dean, College of Natural Sciences and Mathematics

_____
Dean of the Graduate School

_____
Date

Micropulse Lidar Observations of Aerosols over the Atmospheric Radiation Measurement site at Barrow

A

THESIS

Presented to the Faculty

of the University of Alaska Fairbanks

in Partial Fulfillment of the Requirements

for the Degree of

MASTER OF SCIENCE

By

Ramaswamy A.S.R. Tiruchirapalli, B.E.

Fairbanks, Alaska

December 2006

Abstract

Micropulse lidar (MPL) is a ground-based optical remote sensing system designed to determine the vertical structure of clouds and aerosols in the atmosphere. An MPL has operated at Barrow, Alaska since November 2002. From these data, we seek to determine the altitude of aerosol layers in the free troposphere from lidar backscatter profiles. Layer heights are then fed into the HYSPLIT (Hybrid Single-Particle Lagrangian Integrated Trajectory Model) model, a back-trajectory model developed by NOAA (National Oceanic and Atmospheric Administration) to compute isentropic back-trajectories. The model is run interactively using the READY interface and can calculate trajectories from multiple heights within a layer. Case analyses are done correlating dates and trajectory coordinates, synoptic weather charts and events reported from satellites and other remote sensing instruments to determine aerosol sources (e.g. forest fire, volcano eruption or dust storm). All the aerosol events detected by the MPL were categorized into five common atmospheric flow patterns identified from the NCEP (National Centers for Environmental Prediction) / NCAR (National Center for Atmospheric Research) reanalysis charts. We conclude that most of the MPL-identified free-tropospheric aerosol layers could be attributed to Siberian/Alaskan forest fires and Asian dust storms.

Table of Contents

Page

Page

List of Figures

Page

Page

Page

List of Appendices

Acknowledgements

There are a lot of people I would like to thank for a variety of reasons.

I would like to thank my advisor Dr. Kenneth Sassen for giving me an opportunity to work on this project. Without his inspiration and patient guidance, I would not have finished this work. I would like to thank Dr. David Atkinson, Dr. Dana Truffer Moudra, Dr. Glenn Shaw, and Dr. Richard Collins for their constructive suggestions and guidance on this work. I would also like to thank all the faculty members of the Atmospheric Sciences group at the University of Alaska Fairbanks for their help to me in comprehending my graduate coursework and kindling my research interests in this field.

I would like to thank Dr. Connor Flynn for his inputs on various correction parameters on the instrument and his efforts to make the second channel in the lidar work.

I wish to thank my friend James Campbell for helping me in understanding the micropulse lidar instrument and his moral support whenever I needed. Thanks are due to all the students of the Atmospheric Sciences group, especially my previous and current group members - Likun, Patrick, Lilia, Pavan, and Jiang - for creating a fun environment to learn.

I consider myself lucky to be blessed with a friend like Srivathsan, who has been guiding and consoling me at every obstacle I faced during my study. I am grateful to my friends - Arun, Ashok, Gandeeban, Usha, Jeevana, Ashish, Tipsy, Thangamani, Saraswathi, and Jeyashree, for being the surrogate family during my stay in Fairbanks.

Finally, I am forever indebted to my parents, grandparents and my sister for their endless patience, and encouragement throughout my life.

This work was supported by the Department of Energy grants DE-FG-02-03ER 63530 and NSA/AAO UAF Instrument Specialist from the Atmospheric Radiation Measurement Program.

Chapter 1 Introduction

Aerosols are fine particles of solid and liquid suspended in the air. The size of aerosols varies from 0.1 to several tens of microns (μm, micro-meters). They constitute only 0.01% of the earth's atmosphere, their concentrations varying with time and location. They can absorb, reflect and scatter visible radiation affecting visibility, apart from aiding cloud formation by acting as cloud condensation nuclei (CCN). Hence, they interact with the radiation budget and the climate of the earth. Besides from their climatic effects, when present in large sizes and concentrations, they can get deposited in the respiratory system, and cause health problems. They can also severely affect visibility by fog or haze formation.

Aerosol particles can be categorized according to their sources of origin as natural and anthropogenic (man-made). Major natural sources of aerosols include volcanoes, forest fires and desert dust storms. Anthropogenic sources include industrial pollution, biomass burning and dust. The aerosol sources can also be classified as surface and spatial. According to size, Junge classified aerosols as Aitken particles ($r < 0.1$ μm), large particles ($0.1\mu m < r < 1.0\mu m$) and giant particles ($r > 1.0\mu m$). Whitby, 1978 found multimodal distributions of aerosols and categorized them according to mode as the nuclei mode ($r < 0.1\mu m$), the accumulation mode ($0.1\mu m \leq r \leq 1\mu m$) and the coarse mode ($r > 1\mu m$). The particles in nuclei mode grow to accumulation mode, where the particles are aerodynamically stable and are removed by scavenging by rain droplets. The coarse particles can be removed either by sedimentation or rain-out. Aerosols in the accumulation mode are of importance, as they can be transported over a long range.

Aerosols can also be classified as tropospheric (aerosols in troposphere) and stratospheric (aerosols in stratosphere) aerosols. It is estimated that about sixty percent of aerosols in the atmosphere are located in the bottom first kilometer.

1.1 Climatic Effects of Aerosol: Direct and Indirect

Aerosols reflect incoming solar radiation, and tend to cool the surface underneath it. The magnitude of this "direct" cooling depends on the size, composition and concentration of aerosols. The aerosols also serve as cloud condensation nuclei (CCN) for cloud droplet formation. As the concentration of aerosols increases, more cloud droplets of relatively small size tend to form, since the available water vapor has to be shared among the aerosols. These clouds tend to reflect more sunlight than clouds with small amounts of large cloud droplets. Also, the smaller droplets take more time to coalesce and to form large enough droplet to fall. So, aerosols affect the frequency of cloud occurrence, their chances of precipitation and the cloud thickness, which "indirectly" affects the amount of sunlight reaching the Earth surface. According to the IPCC (Intergovernmental Panel on Climate Change), (Houghton et al. 2001), the magnitude of the indirect radiative effects of aerosol are not known.

Coulier and Aitken concluded from laboratory experiments that water vapor super saturations of several hundred percent are required to form droplets in a particle-free atmosphere (homogeneous nucleation). In the presence of aerosols, two percent of super saturation is more than enough to form cloud droplets through the heterogeneous nucleation process.

William Thomson (Lord Kelvin) derived that the equilibrium vapor pressure over the surface of a cloud droplet depends on its curvature, and there is an inverse dependence on the vapor pressure required for equilibrium of the droplet and its size (Kelvin effect).

Raoult derived an equation relating the reduction in the vapor pressure (due to a presence of non-volatile solute), the number of molecules of the solute and the number of molecules of the solution (Rogers and Yau, 1996).

Köhler incorporated both the Kelvin and the Raoult effects in Köhler curves, which predict the growth of droplets in an environment of fixed super saturation. The curve can be approximated by the following equation (Rogers and Yau, 1996),

$$\frac{e_s(r)}{e_s(\infty)} = 1 + a/r - b/r^3, \qquad \textbf{(1.1)}$$

where, $e_s(r)$ is the equilibrium vapor pressure of the solution droplet, $e_s(\infty)$ is the saturation vapor pressure over bulk water, and a and b are constants. The a/r term is the "curvature term" (Kelvin effect) and b/r^3 is the "solution term" (Raoult effect). The above equation suggests that the solution term dominates when the radius is small, and the curvature effect dominates when the radius is large. The critical radius and the critical saturation are given by the following relations, respectively:

$$r^* = \sqrt{3\frac{b}{a}}, \qquad \textbf{(1.2)}$$

$$S^* = 1 + \sqrt{4a^3/27b}\,. \qquad \textbf{(1.3)}$$

Before reaching the critical radius, the droplet is called haze and any change in the saturation ratio would cause the droplet to evaporate or grow. Beyond the critical radius, the droplet is said to be activated and the droplet grows without any further increase in the ambient saturation ratio as long as the environment remains super saturated.

Twomey fitted a curve for concentration (n) of CCN active at a super saturation S,

$$n = cS^k, \tag{1.4}$$

where c and k are constants. It also eliminates the need for the chemical composition of the CCN (e.g., c=600 and k=2/5 for continental air) (Jennings, 1993).

Sassen and Dodd (1988) and Khvorostyanov and Sassen (1998), among others, developed computer models describing the microphysical and radiative properties of various clouds, and the effect of atmospheric variables (such as updraft velocity, n and initial super saturation) on these properties.

Twomey derived a relation for the optical thickness of the cloud, in terms of concentration of droplets and their radii, which are directly related to the concentration and the size of aerosols. As mentioned earlier, high aerosol concentrations tend to yield clouds with high droplet concentrations, which enhance short wave albedo of clouds and longer lifetime of clouds. But, increase in droplet concentrations in a cloud does not change the absorption of terrestrial radiation by clouds appreciably. These effects tend to cool the Earth's surface. On the other hand, light absorbing aerosols (like carbon) present in these droplets, would tend to warm the Earth's atmosphere. Twomey et al. (1984) concluded that the cooling caused by the increase in anthropogenic aerosols is comparable to the global warming due to this increase.

Increasing global temperatures are also suspected to have feedback effects. Rising temperatures would increase the amount of water vapor the atmosphere can hold. Water vapor, being a greenhouse gas, tends to have a direct warming effect on the Earth-atmosphere system and other effects related to cloud liquid water content. Also, the frequency of cloud occurrences and thickness of clouds could affect the hydrological cycle and energy balance of the planet.

Aerosols from biomass burning directly reflect sunlight, and indirectly increase the albedo of the clouds (by acting as CCN), both leading to cooling of the planet (Jennings, 1993).

According to Shaw (1976a), "The aerosols cause heating of the Earth-atmosphere system at poles and cooling at low latitudes".

1.2 A Review of Arctic Air Pollution

According to Arctic Climate Impact Assessment (ACIA), the Arctic has experienced the greatest warming (2° to 3°C since 1950s), with more changes (about 4°C) in winter. The warming results in melting of glaciers in the Arctic, decreases the extent of sea-ice, and decrease in snow cover. These affect the Earth's energy balance and the ocean-atmosphere circulations. Hence, the change in climate in Arctic affects the global climate and vice versa.

Raatz and Shaw (1984) reported that haze of "unknown origin" occurred in the Alaskan Arctic, mostly in late winter. This "Arctic haze" phenomenon was more predominant at higher latitudes (75^0 – 80^0 N). Several experiments in the Alaskan Arctic (Shaw 1980a, 1980b, Rahn 1981a, 1981b, Raatz 1984), Canadian Arctic (Barrie et al.

1981) and Norwegian Arctic (Heintzenberg 1980, Heintzenberg et al. 1981, Rahn et al. 1980) revealed that the Arctic is polluted by long range transport of aerosols from mid-latitudes. Rahn (1981a, 1981b, 1985) analyzed the aerosols in the Arctic atmosphere by neutron activation at the nuclear reactor facility at the University of Rhode Island and found that they contained metals like manganese and vanadium indicating the aerosols originated from a distant industrial source (erstwhile Soviet Union). The concentration of these aerosols tends to peak out during late spring (February to April), with very low concentrations during summer and early autumn months. The synoptic factors contributing to the long range transport are discussed in Chapter 3.

In the 1970s, the Norwegian Institute for Air Research (NILU) conducted a program to identify and characterize the pollutants and their pathways (Ottar et al 1986). The analysis of aircraft and ground based data indicated polluted layers above 2000 m (in summer) and 2,500 m (in winter). The polluted layers below 1,500 m were related to Arctic air mass movements. These aerosols were mostly anthropogenic in nature originating mainly from Eurasia, and occasionally from North America.

Similar experiments (Heidam, 1984, 1985) in Greenland indicate that the aerosols contain crustal elements (from mid-latitudes) like Al, Si, K, Ca, Mn and Fe and marine salts. The anthropogenic aerosols that reach Greenland include metals (from the Ural region in Russia) and fossil fuel combustion products (from mid-latitudes). In accordance with other Arctic aerosols, the aerosol concentration tend to peak in mid-winter, with much cleaner air in the summer months.

Raatz and Shaw(1984) concluded that there is very little contribution by North American sources to the Arctic pollution.

Measurements taken in 1976 show that the American Arctic has around 20 times more haze than found in the Antarctic (Shaw, 1976b). Shaw (1976a) estimated the mean particle radius is 0.04 μm. Shaw (1975) compared the vertical distributions of aerosols in Barrow, Alaska during April and July 1972 and reported that the aerosol concentrations decrease exponentially with a scale height of 1.7km in both cases, with a seasonal variation in turbidity.

The reasons for the occurrence of Arctic haze are the strong temperature inversions (which inhibit the turbulent mixing of atmospheric layers), insufficient water vapor to wash out the aerosols (the amount of water vapor that air can hold decreases non-linearly with temperature), and "quiescent" meteorological conditions (does not aid in dry deposition of aerosols) (Shaw 1995).

The climatic effects of Arctic aerosol depend strongly on their composition (Hu et al/ 2005).Also, they vary strongly regionally and their inter-annual variation depends on the year-specific atmospheric conditions (Rinke et al. 2004).

1.3 Rayleigh and Mie Scattering

The scattering of light by particles depends on the size parameter (x), which can be defined as

$$x = 2\pi a / \lambda , \qquad \textbf{(1.5)}$$

where a is the particle radius and λ is the wavelength of light. If x is very small ($x<<1$), the scattering is referred to as Rayleigh scattering. The scattering of sunlight by the

molecules in the atmosphere is a good example of Rayleigh scattering. The situation is analogous to scattering of sunlight by a dipole. The total scattered intensity of the sunlight has the following empirical relation:

$$I_\lambda \propto 1/\lambda^4 , \qquad \textbf{(1.6)}$$

Blue light ($\lambda \approx 0.425$ μm) has a much shorter wavelength than red light ($\lambda \approx 0.650$ μm) and so scatters more than red. The sky appears blue because of the aforementioned reason. In addition to the wavelength, the scattered intensity also depends on the polarizability, the scattering angle of light and the distance between the molecule and the point of observation.

If $x \geq 1$, the scattering is referred to as Lorenz-Mie scattering. The scattering of visible light by aerosols and hydrometeors is an example of Mie scattering. In contrast to Rayleigh scattering, Mie scattering is complex, and the intensity of scattered light is not strongly dependent on wavelength. Due to this fact, a lot of particulate material in the atmosphere gives a white glare.

1.4 Lidar

Lidar, an acronym for 'Light Detection And Ranging', works on a similar principle as radar, except that it uses light, instead of radio waves. Lidar transmits light into the atmosphere, which undergoes a scattering by the molecules and particles in the atmosphere. The backscattered light is analyzed and the change in the properties of the received light is used to determine the properties of the particles in the atmosphere.

A block diagram of a lidar system is shown in Fig. 1.1 (http://aolab.phys.dal.ca/pages/LidarBasics). A laser transmits a very short and high

energy pulse of light (of a particular wavelength) into the atmosphere.

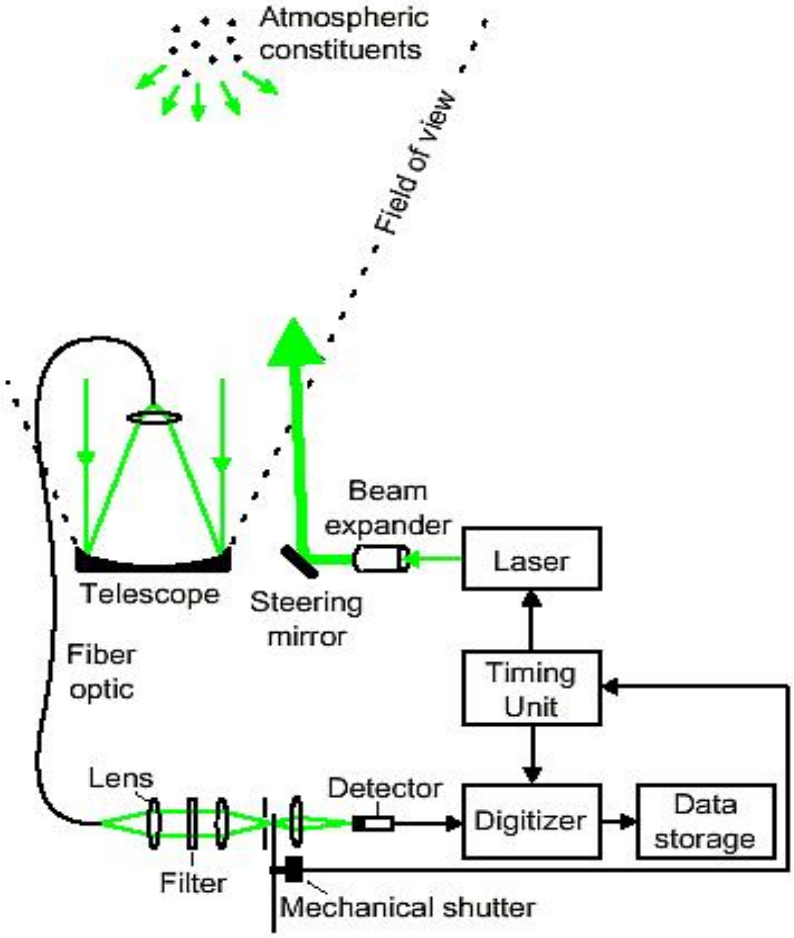

Figure 1.1: Block diagram of a lidar. (Courtesy: The Atmospheric-Optics Laboratory, Dalhousie University).

Though lasers have very low divergence, a beam expander (optional component) is normally used in the transmit path to expand the beam to minimize the divergence of the beam. A small beam divergence ensures that the entire backscattered laser beam is within the field of view (FOV) of the receiver at all altitudes (range). The light backscattered by the molecules and particles in the atmosphere is channeled by the

telescope, which acts as a receiver. The scattered laser light is directed into a photo detector. For some applications, the area of the detector is kept small to reduce the background light (light other than the signal). The photo detector converts the light into an electric signal, and this is recorded to a recording device. The signal on its receive path passes through several filters to reduce the noise and other wavelength components in the signal. The length of the pulse is twice the length of the minimum range resolution. The pulse repetition frequency, (PRF, the inverse of the number of pulses transmitted per second) should be low enough for the light pulses to reach the desired maximum range, and the backscattered light (from all ranges) should reach the detector before the next pulse is fired. This means that the time between successive pulses is long enough that there is no backscatter signal from the previous pulse before a new pulse is shot. A lower PRF ensures low observation times, and hence low background. A very high PRF system could make a lidar "eye-safe", since the average energy per pulse is low (Chapter 2).

Lidars can be used for a variety of applications, including the active remote sensing of atmosphere, topographic mapping, pollution detection and measurements of trace metals at high latitudes. Developments in solid-state devices and optical instruments have led to developments of several lidars based on these applications. In the 1960s, "polarization" (borrowed from radar) in lidar was of much interest, after stronger depolarization (compared to radar) was observed by lidar. Most lasers inherently produce linearly polarized light radiation. When the light is backscattered by particles and molecules in the atmosphere, the backscattered signal is received in two channels, the plane of polarization parallel to the laser and plane of polarization perpendicular to the

laser. To analyze the polarization effects of the backscatter, a quantity called the linear depolarization ratio (δ) is defined as (Schotland et al. 1971),

$$\delta(r) = \frac{P_{\perp}}{P_{\Pi}}, \qquad \textbf{(1.7)}$$

where $P_{\perp}$ and P_{Π} are the backscatter intensities orthogonal and parallel to the plane of polarization of the laser. The δ is a very useful quantity in determining the type and characteristics of aerosols and clouds. For example, LDR for cirrus clouds is around 0.4; for water clouds, thin ice plates and smoke it's nearly zero; for Asian dust it's around 0.25. A detailed discussion on the topic can be seen in Sassen (1974, 1991, 1994).

The power of the backscatter signal is given by the lidar equation,

$$P(R,\lambda) = \{P_0(\frac{c\tau}{2})A\}\{\frac{O(R)}{R^2}\}\{\beta_m(R,\lambda) + \beta_p(R,\lambda)\}\{\exp[-2\int_0^R \alpha(R,\lambda)dR]\}, \qquad \textbf{(1.8)}$$

where P_0 represents the average power of a single laser pulse, c is the speed of light (3 x 10^8 m/s), τ is the laser pulse width, A is the area of telescope, O is the overlap function of the laser beam, a function of range R(m), β_m and β_p are volume backscatter coefficients due to scattering of molecules and particles in the atmosphere respectively (m^{-1}), α is the volume extinction coefficient (m^{-1}) resulting from absorption and scattering of light by molecules and particles in the atmosphere. The above equation can be grouped in the following form,

$$P(R,\lambda) = KG(R)\beta(R,\lambda)T(R)^2, \qquad \textbf{(1.9)}$$

where, $\beta = \beta_p + \beta_m$ and T= T_p T_m and K is the "system constant" of the instrument; G(R) is the geometry factor with $1/R^2$ dependence; $\beta(R,\lambda)$ is the total backscatter

coefficient of the atmosphere, which is the sum of backscatter coefficient due to particles (β_p) and the backscatter coefficient due to molecules (β_m) present in the atmosphere; T is the atmospheric transmittance, a measure of light lost before it reaches range R, which is the product of transmittance of molecules (T_m) and particles in the atmosphere (T_p). The parameters K and G can be controlled experimentally.

The process of determining the quantitative parameters (such as optical depth) from the raw signal is called "inversion".

1.5 Eye- safe Lidars

The traditional lidars have high pulse energies ranging from 0.1 to 1 J, with low repetition rates varying from 0.1 to 10Hz. The disadvantages of using these lidars include low efficiency, poor reliability, and high operational and development costs, which make them difficult for full-time uninterrupted measurements. Eye-safety is a key requirement for full-time unattended monitoring. Some of the eye-safe lidars are discussed (Spinhirne, 1995) in this section, including micropulse lidar, pseudo modulated continuous wave (CW) lidar, pulsed diode laser lidar and near IR eye-safe lidar.

The principle of pseudo modulated CW lidar involves shooting a high frequency modulated laser beam in the atmosphere. The beam undergoes elastic scattering of molecules and aerosols. A part of this signal hitting the receiver is captured in the histo-programming memory. To obtain the backscattered signal, the transmitted and received signals are cross-correlated at each bin (range). The major disadvantage of this lidar is the daytime background. The effect of daytime background can be reduced by using an improved optical band pass filter and a narrow field of view.

A pulsed diode laser lidar uses a pulsed laser diode as a source and analog avalanche photo diode for detection. The instrument is good at detecting aerosol boundary layers and cloud heights. The major disadvantage of the instrument is the inherent noise due to a weak input signal.

A near IR lidar uses wavelength in the near infra-red range, a frequency at which the sensitivity of human eye is low.

In the next section I discuss the advantages and disadvantages of the micropulse lidar.

Chapter 2 Signal Analysis of MPL at Barrow

The concept of Micropulse Lidar (MPL) was introduced by J .D. Spinhirne in 1992. Unlike traditional lidars, MPL has a higher PRF (on the order of KHz, rather than Hz) and low pulse energy (in the order of μJ, rather than J), which permit eye-safety. The eye-safe, compact cloud and aerosol lidar has a PRF of 2.5 KHz with approximately 20μJ/pulse at the exit of the aperture, and a pulse length less than 10ns. The lidar has a diode-pumped Spectra Physics 7300-L3 Nd:YLF laser and EG&G SPCM-AQ-100 Geiger mode avalanche photodiode (GAPD) photon-counting module as a detector. It has "shared'' MPL optical paths that coincide through a 20-cm aperture, adjustable focal length, Celestron-made Schmidt–Cassegrain telescope. Eye safety is achieved by beam expansion, and a narrow field of view is used to prevent multiple scattering and limit ambient background signal. Due to low pulse energies, pulses have to be averaged over time to achieve a significant signal to noise ratio (SNR).

The MPL at Barrow has been operational since November 2002. The dataset analyzed for this work is through September 2005. The MPL was initially operated with a single channel at 0.523 μm (green) wavelength. A polarization channel was added in December 2003, to facilitate a more quantitative study of clouds and aerosols. A polarizer was introduced in the outgoing laser path, which rotated the plane of polarization of the laser by 180°. A simple flip-flop circuit was used to activate the polarizer at regular intervals, forcing the instrument to shoot parallel and perpendicularly polarized signals alternately. Due to the inclusion of the new channel, data before and after December 2003

are processed in a different manner. The maximum permissible range of the MPL is 60km (period between the pulses*speed of light/2).

2.1 Theory

A beam of light, of any wavelength, undergoes a backscatter by molecules and particles in the atmosphere. A (vertical) profile is a plot of the variation of atmospheric backscatter with height. The theoretical backscatter of molecular atmosphere by 0.523 μm light is shown in Figure 2.1, where the dotted line is for the winter and the solid line for summer. When the atmosphere contains aerosols or hydrometeors, the backscatter would be less than this theoretical backscatter at a given height. The attenuation caused by the aerosol (or cloud) layer, would force the next (upper) layer to backscatter less than the theoretical value for that height, if the layer is free of aerosols or hydrometeors. The distance between the theoretical and the actual backscatter at this molecular layer would correspond to the optical depth of the aerosol (or cloud) layer below it. Hence, by comparing the theoretical profile and the lidar return, many useful radiative quantities of an aerosol or cloud layer can be calculated. In the presence of a second channel the linear depolarization ratio (Equation 1.7) can be calculated, which can aid in distinguishing aerosols and hydrometeors.

A lidar height versus time image is a color-coded time series plot of normalized lidar returns. The lidar image helps to detect aerosol or cloud layers and how they evolve over time. It helps in visualizing various microphysical processes of the atmosphere, viz. virga, formation of a cloud from an aerosol, and time periods of snow or rainfall.

Normally, hydrometeors attenuate and scatter light better than aerosols. Hence, regions of high backscatter would correspond to hydrometeors and regions of low backscatter would correspond to aerosols.

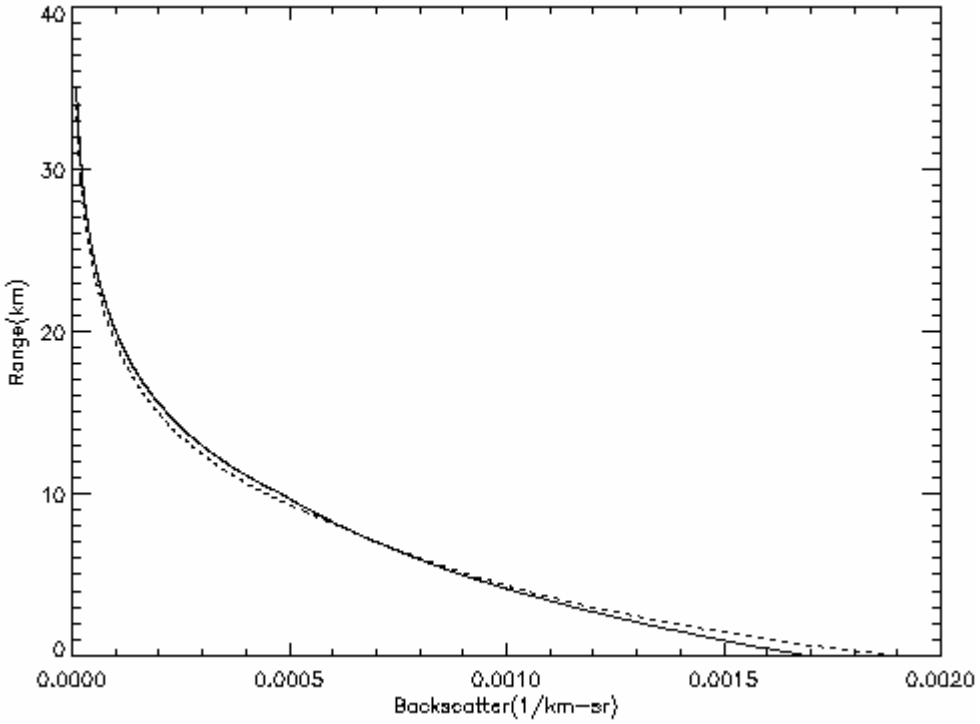

Figure 2.1: Theoretical backscatter of 0.523 µm wavelength light

The prime focus of this study is to detect aerosols and distinguish them from hydrometeors. The presence of any hydrometeor can be confirmed by atmospheric soundings. Atmospheric soundings are altitude measurements of atmospheric variables, such as temperature, pressure and relative humidity.

Analyzing lidar intensity plots in tandem with atmospheric soundings, the regions of strongest intensity on lidar image, and relative humidity (from sounding) greater than

80%, would correspond to hydrometeors. When the temperature at that range is less than zero Celsius, relative humidity with respect to ice is considered, and is calculated by the following equations,

$$\ln(\frac{e_{si}}{e_{s0}}) = 6293(\frac{1}{T_0} - \frac{1}{T}) - 0.555\ln(\frac{T}{T_0}), \qquad \textbf{(2.1)}$$

$$RH_{ice} = \frac{e}{e_{si}}, \qquad \textbf{(2.2)}$$

where, e_{si} is the vapor pressure and saturation vapor pressure with respect to ice at temperature T; e_{s0} is the saturation vapor pressure at reference temperature T_0 (normally 0^0 C, e_{s0}=6.11 mb @ 0^0 C); RH_{ice} is the relative humidity with respect to ice; and e is the vapor pressure at T.

Referring to Figure 2.5, the background color (blue, in this case) corresponds to the scattering by molecules in the atmosphere. The black color (corresponding to zero intensity) represents no available signal. The white color (corresponding to maximum intensity) represents the presence of hydrometeors. Any intermediate color in the color map from the background color to the white would signify the presence of either a hydrometeor or an aerosol.

2.2 MPL Equation and Correction Parameters

The MPL equation is of the form (Campbell et al. 2002),

$$n(R) = \frac{\frac{\left(O(R)CE\beta(R)T(R)^2\right)}{R^2} + n_b + n_{ap}(R)}{D[n(R)]} \qquad \textbf{(2.3)}$$

where, n is the signal measured by detector as a function of range R; C is the calibration / normalization constant; E is the transmitted laser pulse energy (also known as energy monitor); n_b and n_{ap} are the background and after pulse signal corrections respectively; D is the dead time signal correction; and other terms have been defined earlier (Equations 1.8 and 1.9).

As can be seen from this equation, most of the parameters are functions of range. The signal is measured in photon electrons per second and the range in km. The above equation can be rewritten in the following form

$$\beta(R)T(R)^2 = \frac{n(R)D[n(R)] - n_b - n_{ap}(R)}{O(R)CE} * R^2. \qquad \textbf{(2.4)}$$

The above parameter is called the Normalized Relative Backscatter (NRB) signal.

A detailed explanation for these parameters could be found in Campbell et al. (2002); however a brief description is given below.

2.2.1 After Pulse Correction

The outgoing pulse interacts with the reflective surfaces along the optical path and the backward reflections saturate the detector. This unintended signal is called after-pulse, and is a function of range. To estimate the after-pulse, "a beam blocked case" is chosen and the vertical profile is averaged (see "Averaging" section) for 0.05 Julian days. A signal that is blocked by a low-level target (range < 0.5 km) is called a "beam blocked" signal. The averaged profile is then fitted to the following polynomial

$$n_{ap} = a + \frac{b}{R} + cR^2 + \frac{d}{R^3}, \qquad \textbf{(2.5)}$$

where, a, b, c and d are constants; and R is in meters. The after-pulse correction, as a function of range, is shown in Figure 2.2.

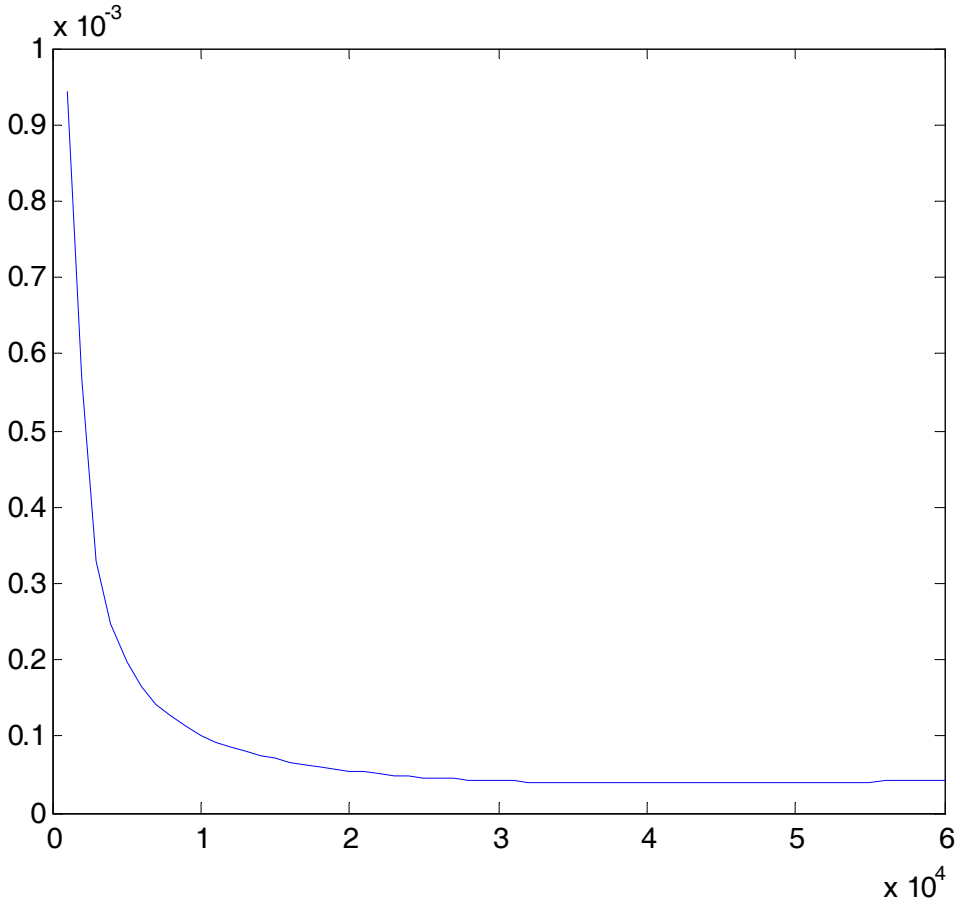

Figure 2.2: The after pulse correction as a function of range

2.2.2 Dead Time Correction

The detector will not be able to count all the photons that are incident on it, especially when the count rates are high. The dead time correction factor is a statistical function that compensates for this saturation effect of the detector. It is a function of the

measured count rate (Fig 2.3(a)) and is supplied by the manufacturer. It is of the following form,

$$D[n(R)] = a_2 + b_2 n(R) + c_2 n(R)^2 + d_2 n(R)^3 + e_2 n(R)^4 + f_2 n(R)^5, \qquad \textbf{(2.6)}$$

where a_2, b_2, c_2, d_2, e_2 and f_2 are constants.

2.2.3 Overlap Correction

Due to the narrow receiver FOV (Figure 1.1) and the expanded beam, the pinhole is not wide enough to accommodate all the incident rays from a near field object. The correction applied to compensate for this "near field signal vignetting" is called overlap correction. The correction is a function of range (Figure 2.3(b)) and approaches unity when the vignetting disappears (at a very distant range). To estimate overlap, an averaged "clear-sky" profile (a day with almost no aerosols) is taken and fitted to the following polynomial,

$$O(r) = a_1 + b_1 R + c_1 R^2 + d_1 R^3, \qquad \textbf{(2.7)}$$

where, a_1, b_1, c_1 and d_1 are constants; r is the range in meters.

2.2.4 Background Correction

The background correction corrects for the ambient light. This correction is calculated by averaging the raw signal from the 45 to 55 km range.

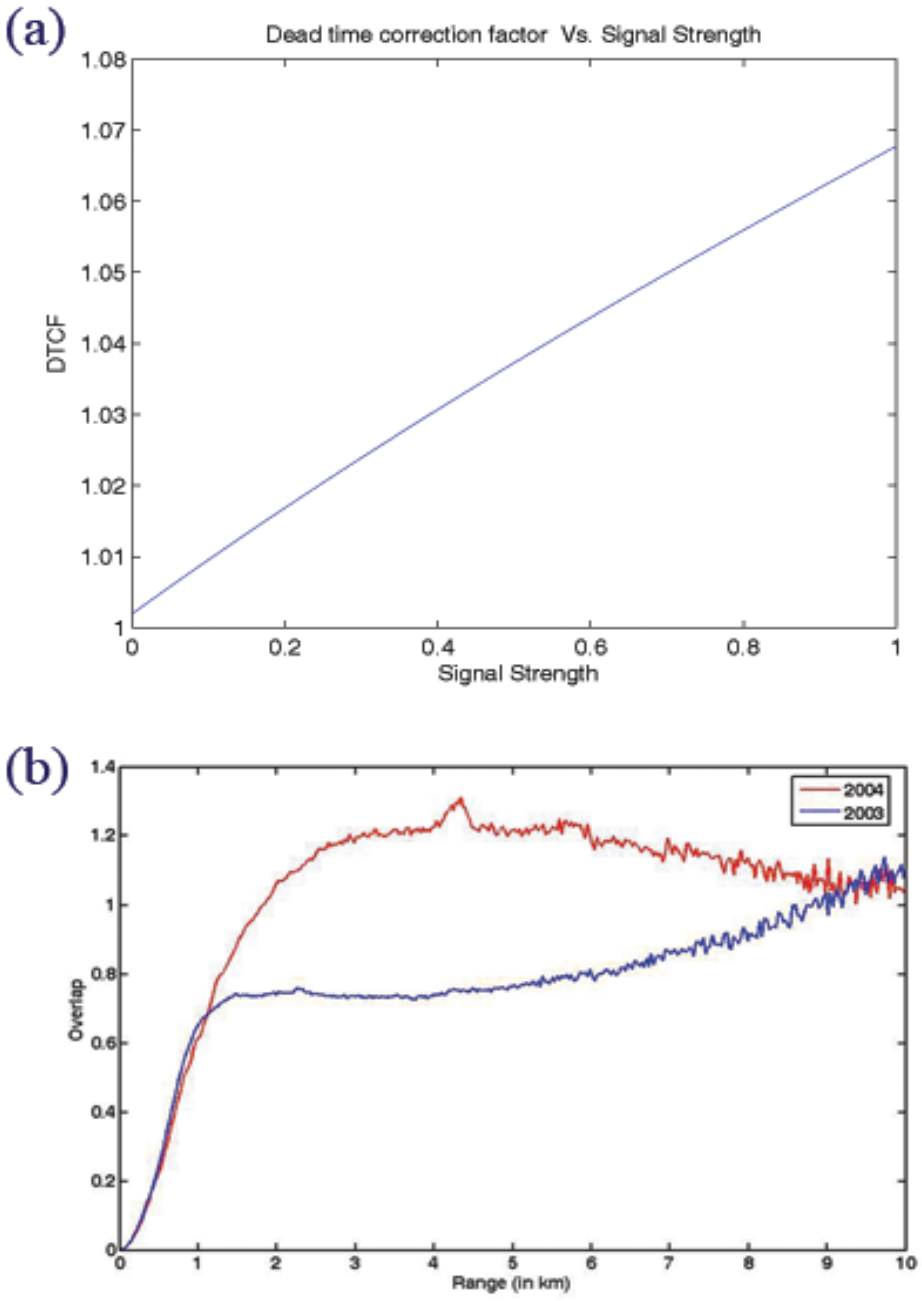

Figure 2.3: (a) The dead time correction factor as a function of signal strength, (b) The variation of overlap function with distance.

2.2.5 Normalization/Calibration Constant

The normalization constant is the ratio of the observed profile to the theoretical profile at a certain altitude. Though normalization is done by averaging the signal over a kilometer in range, normalizing at a single point (altitude) is not uncommon. The former technique, when used, allows the maximum number of points in the profile to coincide with the theoretical curve. Normalization is usually done at an altitude below the first aerosol layer.

The procedure involves determining the optical depth from an independent data source, and substituting it in the MPL equation to determine the calibration constant. AERONET (AEROsol Robotic NETwork) Sunphotometer (operated by Goddard Space Flight Center NASA) data were used to obtain the value of aerosol optical depth. Since the AERONET operates only in summer months, the dataset for the consistency test was restricted to these months. To make calculations easier, only "clear-sky" (no cloud) days were analyzed. Data from June 2004 were used as test data, as they had more clear-sky cases compared to other summer months and the sunphotometer had less interrupted data during this month. The NRB signal from the MPL can be written as

$$\mathrm{NRB_{MPL}} = C(\beta_p + \beta_m)T_p^2 T_m^2, \qquad \textbf{(2.8)}$$

$$\mathrm{NRB_{MPL}} = C\beta_m(1+\frac{\beta_p}{\beta_m})T_p^2 T_m^2. \qquad \textbf{(2.9)}$$

Assuming $\beta_p >> \beta_m$, we get

$$\mathrm{NRB_{MPL}} = C\beta_m T_p^2 T_m^2. \qquad \textbf{(2.10)}$$

From the theoretical profile, we can write the NRB signal as

$$\mathrm{NRB_{THE}} = \beta_m T_m^2 . \qquad \textbf{(2.11)}$$

The transmittance of the atmosphere due to particles can be determined from the optical depth (measured by independently) using the following relation,

$$T_p = \exp(-\tau) . \qquad \textbf{(2.12)}$$

From the above three relations, the calibration constant can be determined. Figure 2.4 shows the variation of optical depth (measured by the sunphotometer) and calibration constant of the instrument in June 2004.

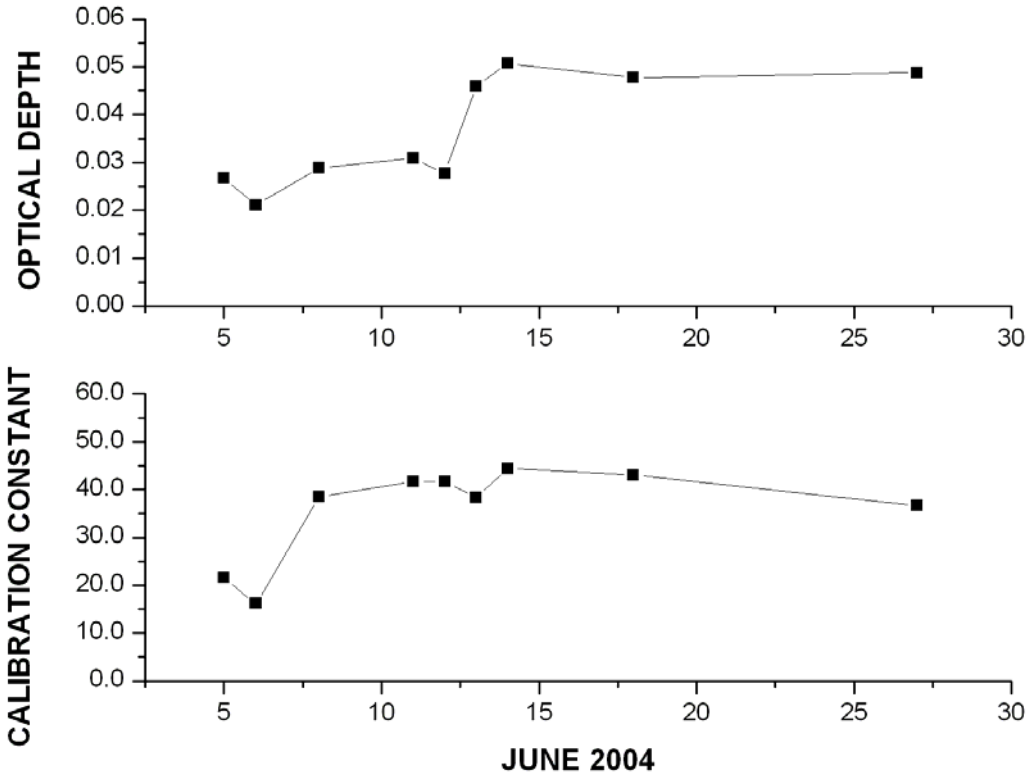

Figure 2.4: The variation of optical depth measured by the sunphotometer (top) and the variation of the calibration constant of the MPL at Barrow (bottom).

2.3 Data Processing

The first step in processing data is the estimation of correction parameters of the MPL equation. Initially, dummy parameters are used in the MPL equation to create lidar images for the entire dataset. Analyzing these lidar images, Julian days for the estimation of correction parameters are chosen. The corrections are then applied to the data, to create a new set of lidar images. The days of aerosol events and the approximate heights of these aerosol layers are determined by visual inspection of the images.

2.4 Algorithm for Image Creation

The MPL data are stored in binary files day wise (Dataset 1 and 2), and each file about 13 MB in size.

The algorithm to process the data is the following:

1. Read files containing the correction parameters.
2. Calculate the length of a (non-averaged) vertical profile (shot).

   L=number of vertical bins x 4 + header length.
3. Read L bytes of data from input (MPL data) file.
4. Get offset time and other parameters from header.
5. Calculate signal intensity at different heights.
6. Calculate Julian day from offset time and input filename.
7. For dataset 2, determination of co-pol or cross-pol is done and both channels are stored in separate arrays.
8. Steps 3 to 7 are repeated till end of file is encountered.

9. The array(s) is (are) then averaged (for one day, in this work). The correction parameters are applied, if necessary.
10. The array(s) is (are) normalized (with maximum value of 0.25) and coded with 256 colors.
11. For dataset 2, depolarization ratio is calculated by taking ratio of co-pol and cross-pol and a similar image is made as in step 9.

The above algorithm can also be used to plot profiles. Steps 1 to 9 are followed and a plot routine is used to plot the arrays column wise as a function of range.

While visual inspection of lidar images can be used to identify an aerosol, lidar profile inversions are necessary to make quantitative measurements. Due to the variation in the calibration constant, inversion of profiles cannot be done reliably. A simpler approach was used to detect aerosol layers and quantify their radiative properties. The lidar profile was normalized at the start of each aerosol layer and a "relative" scattering ratio was defined, as the ratio of the lidar backscatter signal to the theoretical signal at a particular altitude. A mean "relative" scattering ratio could be calculated for each aerosol layer by averaging the "relative" scattering ratios over the layer. The main advantage is that the calculation does not require any knowledge of the amount of signal attenuated below the particular altitude (by a lower level cloud or aerosol layer) and hence eliminates the need for an additional instrument to measure optical depth. However, due to the above mentioned advantage, this measure could not be directly related to the optical thickness or type of aerosol layer. A more detailed discussion is done in Chapter 4.

2.5 Automated Algorithm for Aerosol Detection

The procedure developed to automatically detect aerosols contains the following steps:

1. The profile is averaged (vertically) using a sliding (moving) average procedure.
2. Points of local maxima and minima in the profile are then determined.
3. The profile is normalized at the first minimum point above 1.5 km, and new relative scattering ratios are calculated.
4. Between two successive minimum points, the maximum relative scattering ratio is determined. If the maximum scattering ratio was less than 1.05, the control is transferred to next step, otherwise the point where the relative scattering ratio crosses 1.05 is assumed as the start of an aerosol layer. The top of the aerosol layer is the point where the relative scattering ratio comes back to 1.0.
5. Steps 3 and 4 are repeated for all minima in the profile to detect higher aerosol layers and the normalization is done after each aerosol layer at the next minima point.
6. Layers with higher relative scattering ratios (greater than three) are neglected because experience has shown that these layers contained hydrometeors.

Since the signal is very noisy, a moving average method is used to eliminate the zigzag pattern (noise) in the profile. For a profile (or signal) with N data points, a m-point

moving average can be defined by taking average of m consecutive data points of the profile. Mathematically,

$$S_i = \frac{1}{m} \sum_{j=i}^{j=i+m-1} P_j \qquad \text{i=1,2,….N} \quad , \qquad \textbf{(2.13)}$$

where S represents the averaged profile and P represents the original profile.

A 3 point moving average is used in the algorithm because it yielded good results (see below). The normalization is always done at the minima points to make sure that the new relative scattering ratios calculated are never less than one (which is not allowed theoretically).

To illustrate the above algorithm, a simple case is considered, where there is only one aerosol layer. A backscatter profile starting at 00UTC on February 9, 2004, with 0.05 Julian day averaging, is shown in Fig 2.6a. The dotted line (Fig 2.6a) represents the theoretical backscatter by the molecular atmosphere for 523 nm light. Referring to the lidar image, and soundings (Fig 2.5) and the profile (Fig 2.6a), a relatively strong aerosol layer is present at an altitude just below 4.0 km. Fig 2.6a shows a comparison of the actual profile and the profile after 3 point moving averaging is done (Step 1). The 3-point moving average smoothes the profile, especially at higher altitudes. Figure 2.6b shows the profile after steps 2 and 3 of the algorithm. The minima representing the start of the aerosol layers are captured well by the algorithm. After normalizing at the first minimum, we could see that only the values above the first minimum are multiplied by the difference between the profile and the theoretical backscatter at the first minimum. Figure 2.7a contrasts the actual scattering ratios and the scattering ratios calculated from the

profile after normalization is done. Though there is an inherent digital filter in the algorithm determining local maxima and minima, the moving average procedure is applied to the backscatter profile in order to smooth the scattering ratio plot. The new scattering ratio plot has a relative scattering ratio at the first minimum (range = 2.174 km) equal to unity, as expected after normalization.

The algorithm starts to track the new scattering ratio plot and finds the maximum scattering ratio achieved before reaching the next minimum is 1.02, which is less than the 1.05, the minimum scattering ratio assigned to an aerosol layer. The value 1.05 was chosen after rigorous analysis of the noise in the profiles and effect of number of points to be averaged in the moving average filter (discussed later in the chapter). The algorithm now moves to the next minimum (range= 3.523 km), and normalizes the profile at that point.

The backscatter profile and scattering ratio plots after the normalization at the second minimum is shown in Fig 2.7b. The algorithm starts to track the new profile from the second minimum and finds the maximum scattering ratio to be 1.241 (range=3.793km). So, it considers the second minimum point as the start of an aerosol layer. The profile crosses unity from 1.01 (range = 3.943 km) to 0.9831 (range=3.973 km), and determines 3.973 km as the end of the aerosol layer. Hence it detects the layer from 3.523 km to 3.793 km as an aerosol layer. The algorithm then repeats the same process at all minima, and does not find any other aerosol layer.

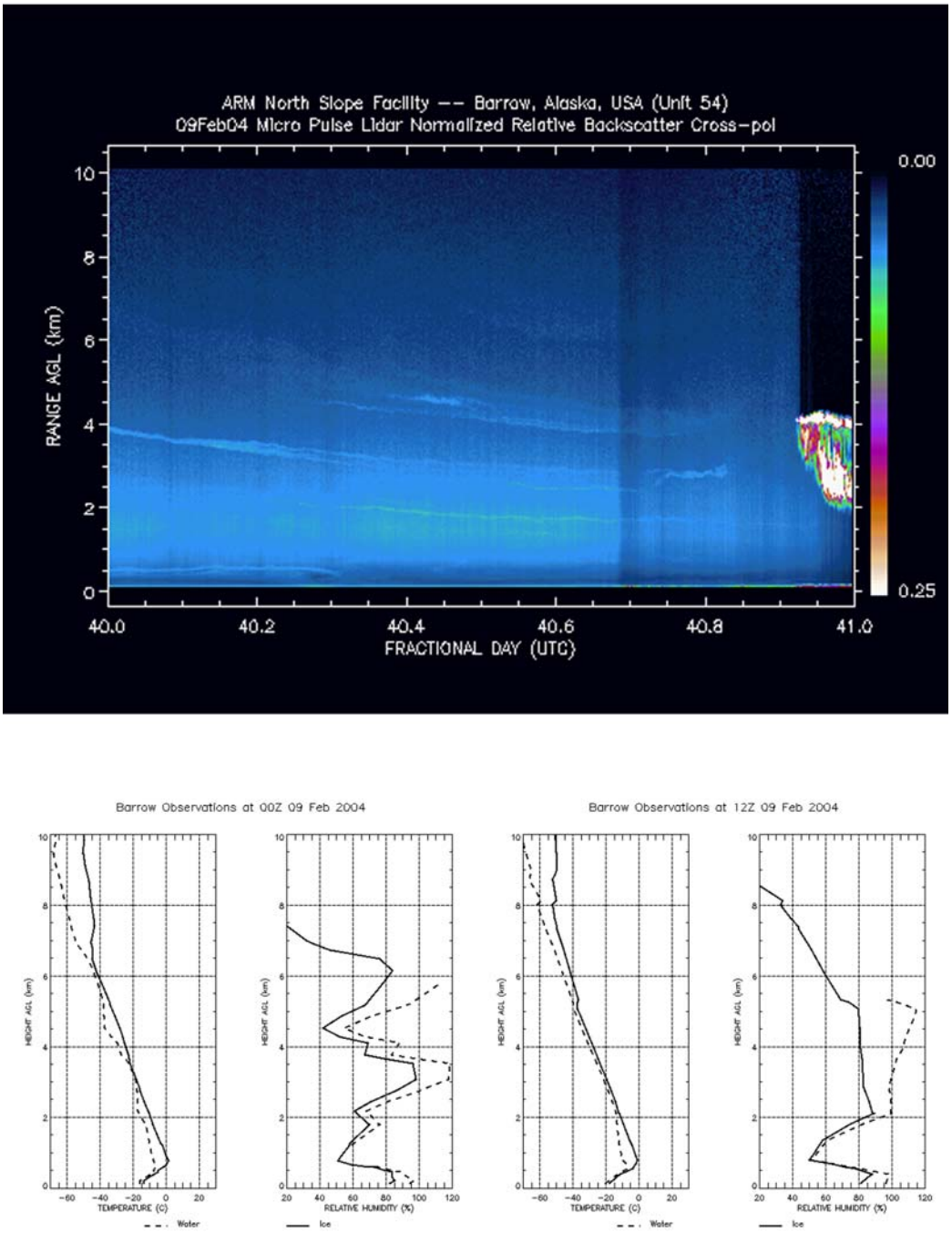

Figure 2.5: Lidar image (top) and the soundings for 00Z (UTC) (bottom left) and 12Z (UTC) (bottom right) for Feb 9, 2004.

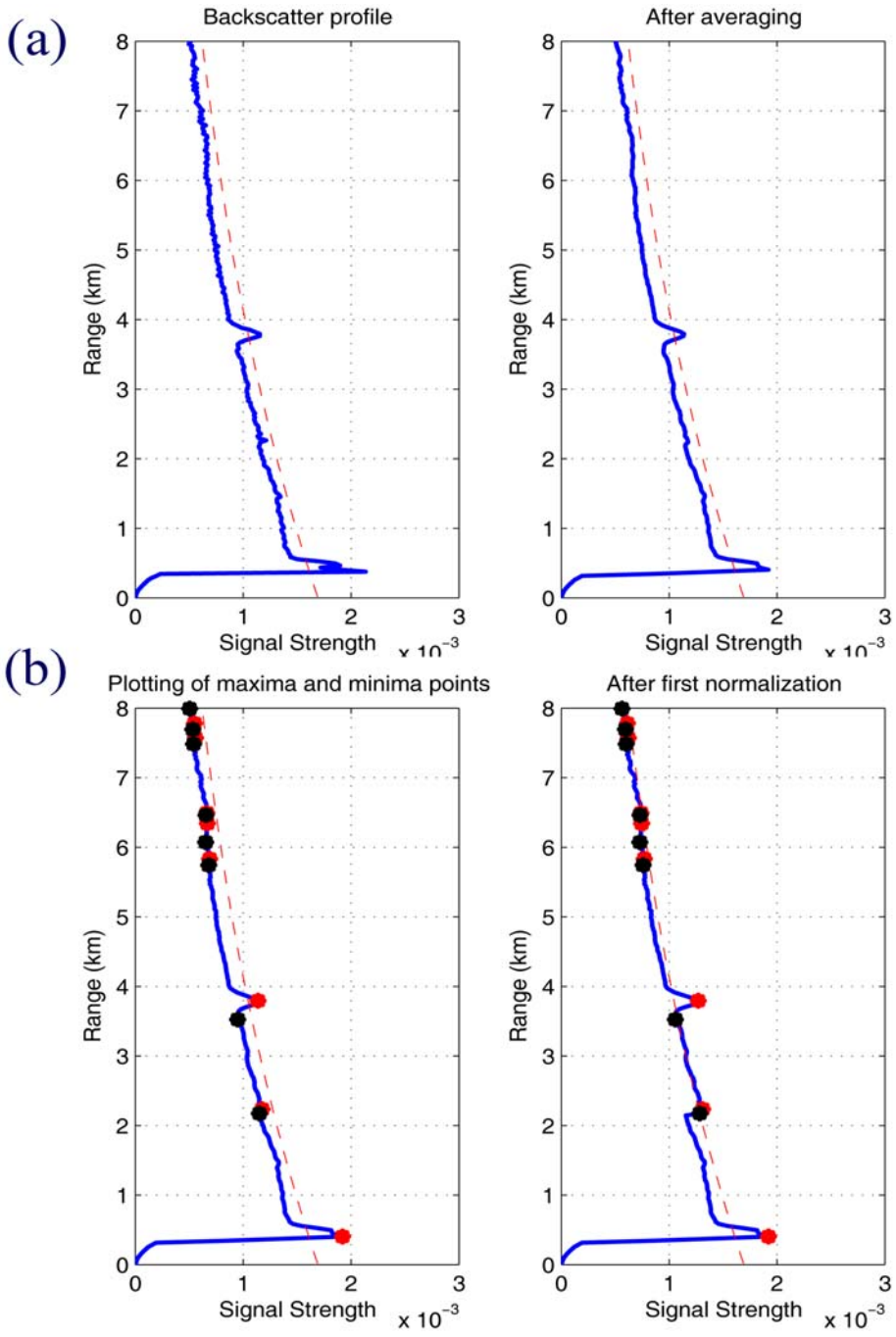

Figure 2.6: (a) A comparison of NRB signal before and after averaging; (b) Plotting of maxima and the signal after first normalization.

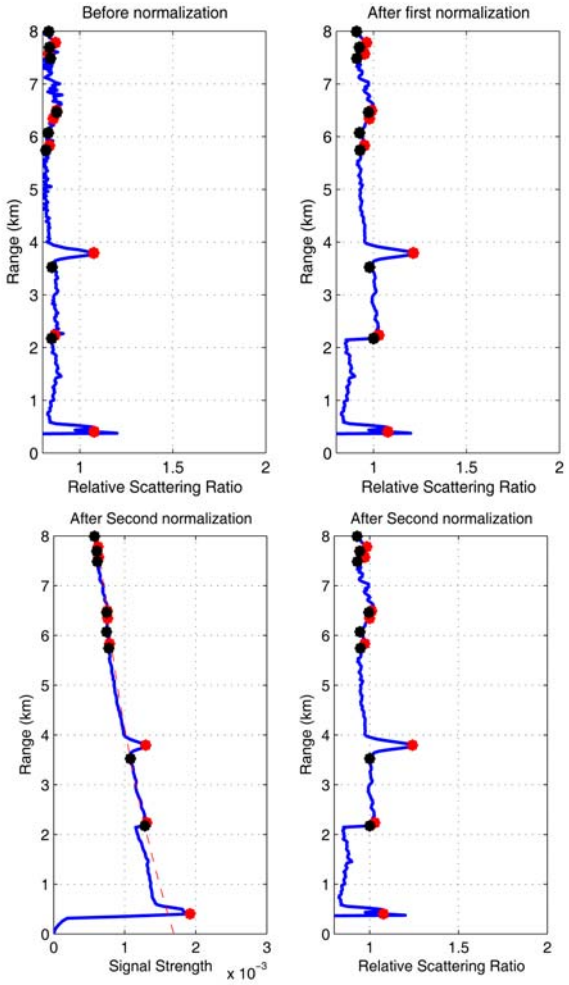

Figure 2.7: (a) The relative scattering ratio plot before and after first normalization, (b) The NRB signal and the relative scattering ratio after second normalization.

2.6 Drawbacks of the Algorithm

The detection of aerosol layers and estimation of their heights depends on the efficiency of detecting the minimum and maximum points, and the number of points used in the moving average procedure. The moving average method has an inherent ability of catching the trend of signal strength at higher altitudes. This could either lead to an

underestimate or an overestimate of the height of aerosol layers, or failure to detect the aerosol layer. Using the previous example, Fig. 2.8 shows a comparison of using 0, 3 and 20 points to average in the moving average filter on scattering ratios. The scattering ratio plot is chosen for the illustration as it has more variability. A 3-point moving average smoothes the profile slightly, with little deviation between the actual and the average values of the profiles. The scattering ratios calculated from these averaged profiles are, however, underestimated or overestimated depending on the values at higher levels. The 20-point average changes the way the plot looks. Though it only shows the trends (aerosol layers), the altitudes of the aerosol layers and the scattering ratios contain large errors. The 20 point average also fails to detect weak aerosol layers. The above arguments also hold good for averaging of backscatter profiles. Another example is when a cloud layer is right on top of the aerosol layer.

The algorithm detects the first aerosol layer (with no cloud below it) with a fair amount of accuracy. The heights calculated by the algorithm for these layers have an error of up to 5 bins (150 m). This can be attributed to the weakening of an aerosol layer or the descending nature of the aerosol layer within a day. The algorithm fails to detect weak aerosol layers (minimum scattering ratio for the aerosol layer is set to 1.05). It also does not do well in estimating higher aerosol layers, especially ones which have cloud layers beneath them.

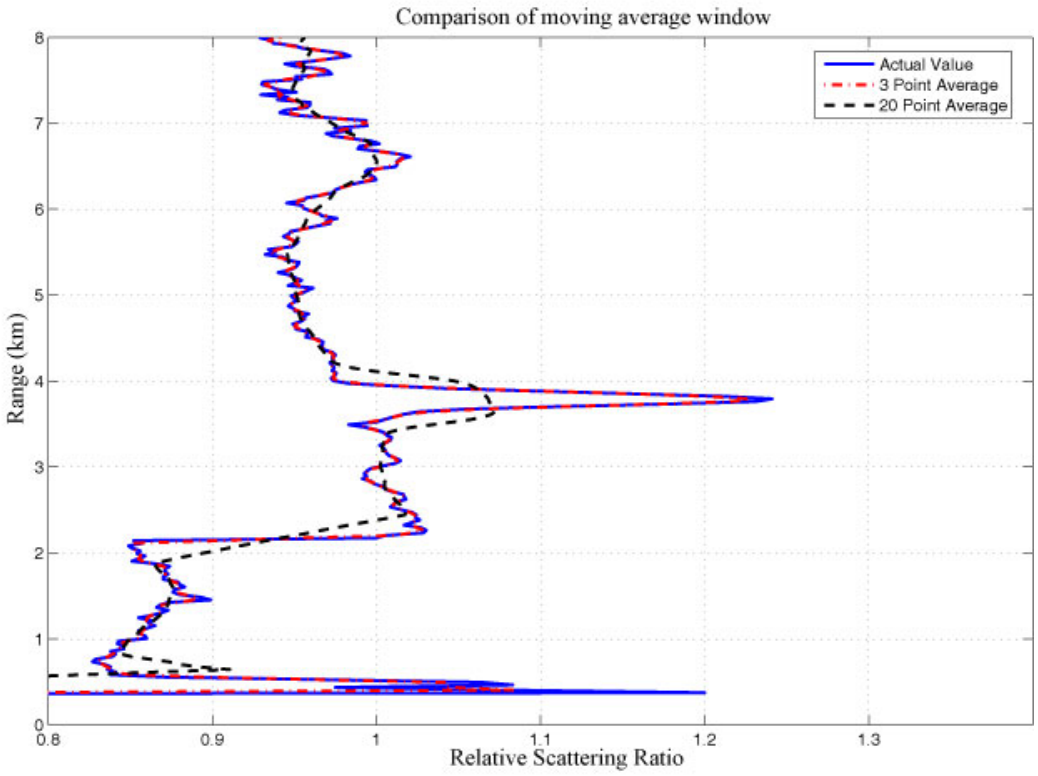

Figure 2.8: Comparison of various moving point averages applied to relative scattering ratios

2.7 Time Averaging

The signal strength of a single vertical profile is shown in Figure 2.9. Due to the low energy of the pulse, averaging of pulses is essential to obtain a significant SNR. The amount of signal averaging applied is a very important factor and varies with the application. An over-averaging could cloud a microphysical process, while under-averaging could result in a noisy incomprehensible signal.

Referring to Figs. 2.9 and 2.10, it can be inferred that even a two hour average has significant noise remaining in the signal. For evaluating correction parameters, a profile

has to be as smooth as possible, as any kinks could lead to an approximation error in the correction equation. Hence, while it is better to average for a long enough period of time, the length of averaging is limited by the rapidly changing conditions in the atmosphere. For example, to evaluate the overlap correction, the longest clear sky profile observed was approximately 2 hours (0.1 Julian day). Since all the time calculations are based on Julian day (for convenience), the averaging of signals is also in terms of Julian day.

For calculating scattering ratios, the profile has to be averaged to define a clear aerosol boundary with a significant SNR. Unlike the averaging done in estimating correction parameters, the smallest amount of averaging that yields a significant SNR should be used to register all the microphysical phenomena that occur in the atmosphere. For calculating heights and scattering ratios of aerosol layers, a 0.05 Julian day average was used.

To create the lidar image, the data are averaged to get 1008 shots per image. This number is good up to imaging for a seven-day period of data. When a week's data is used, each shot displayed represents 15 minutes (1008/(24x7)=4 shots/hour) of averaged data. On the other hand, when images are created daily, each shot represents 85 seconds of averaged data, which is long enough to record change in microphysical processes.

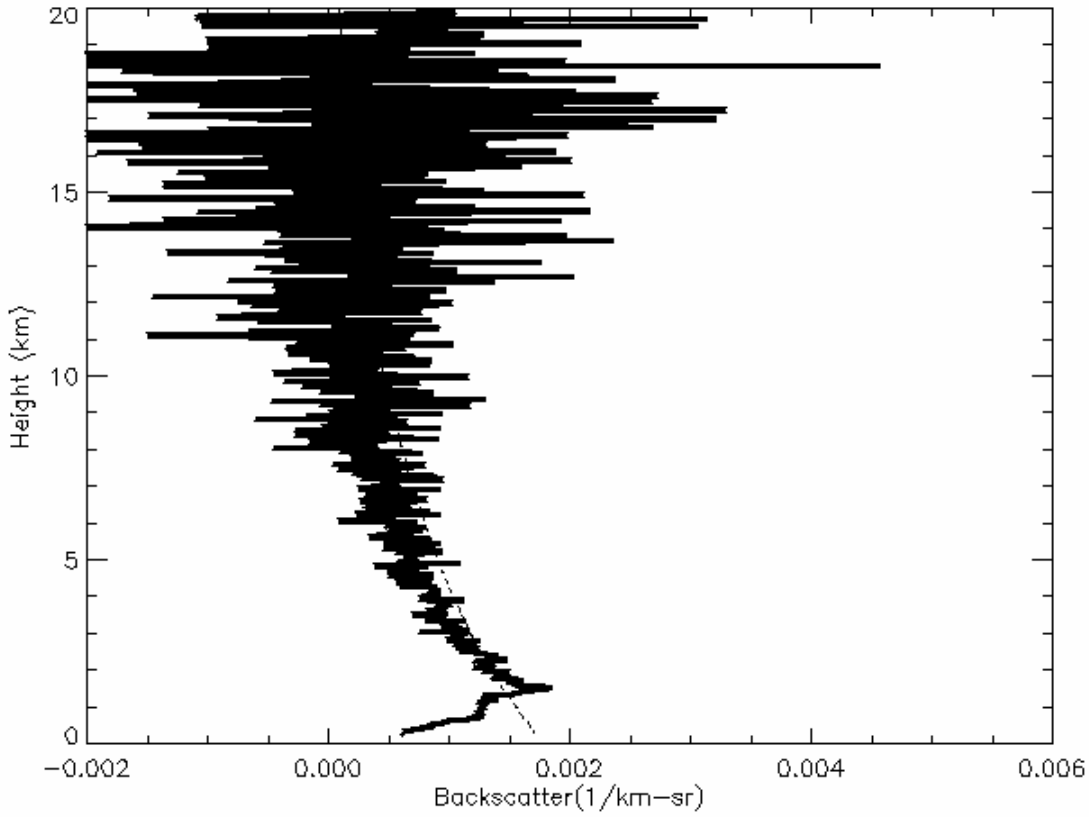

Figure 2.9: The backscattered signal resulting from a single laser pulse.

(a)

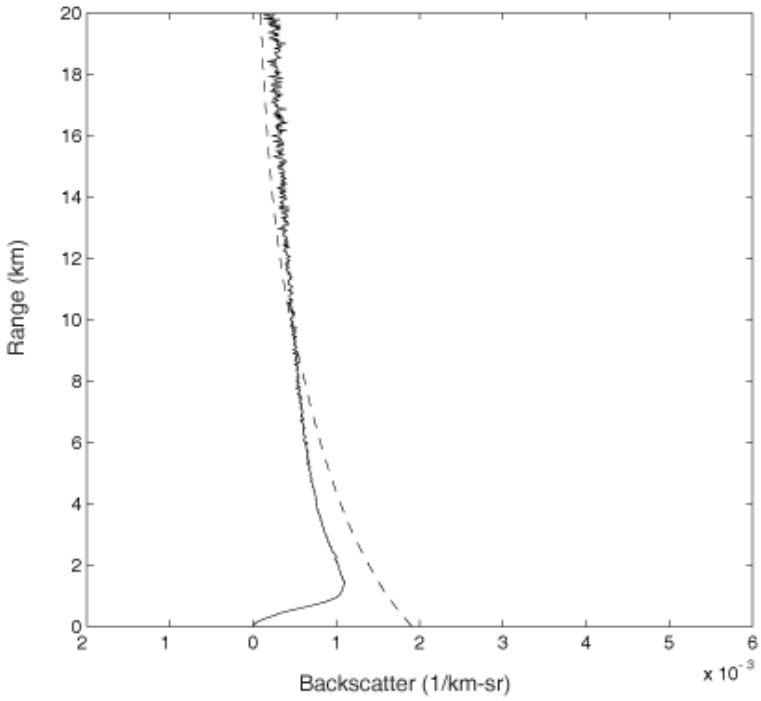

(b)

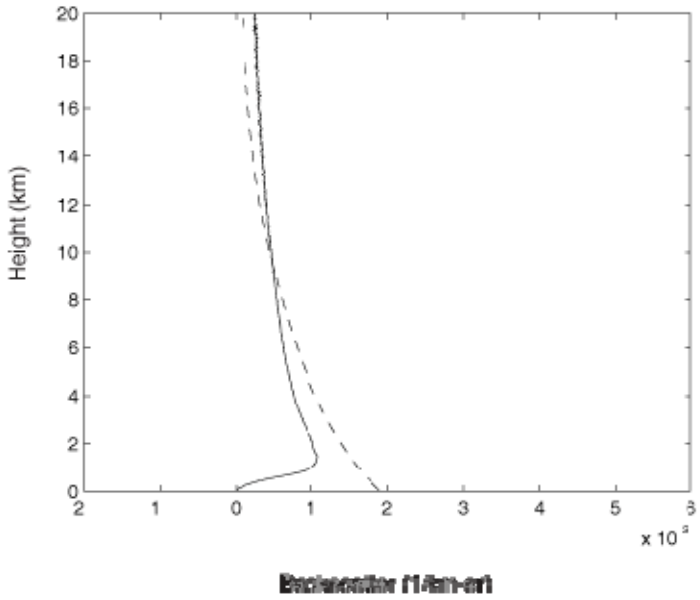

Figure 2.10: A NRB signal (with no overlap correction) with (a) 0.01 Julian day averaging and (b) 0.1 Julian day averaging.

Chapter 3 Backtrajectories and Climatologies

Aerosols can be transported over long ranges, depending on their size and the existing synoptic conditions. The knowledge of the sources of these aerosols helps us to determine the duration of transport and the transport path. The simplest and the easiest way to determine the transport path is to use a back trajectory model. The path taken by an air parcel over a period of time is called its "trajectory" and the models that describe them are called trajectory models. Trajectory models are used to investigate air mass flow in general, and find extensive use in investigating and tracking air pollution. They can be used to estimate the aerosol transport path and to develop source-receptor relationships of air pollutants, and climatology, with very little computation time (about 2-3 min).

3.1 Trajectories and HYSPLIT

The trajectory of a small air parcel can be described using the following equation (Stohl, 1998):

$$\frac{dX}{dt} = \dot{X}[X(t)], \qquad \textbf{(3.1)}$$

where X=position and t=time.

Evaluating the Taylor series expansion of X (t) at $t_1=t_0+\Delta t$ about $t = t_0$, we get

$$X(t_1) = X(t_0) + (\Delta t)\frac{dX}{dt}|_{t_0} + \frac{1}{2}(\Delta t)^2 \frac{d^2X}{dt^2} + ... \qquad \textbf{(3.2)}$$

Neglecting higher order terms,

$$X(t_1) \approx X(t_0) + (\Delta t)\dot{X}(t_0). \qquad \textbf{(3.3)}$$

Using the above equations, trajectories can be calculated either forward in time (forward trajectory) or backwards in time (back trajectory).

Trajectories can be calculated by interpolating the wind observations (from radiosonde measurements) at different locations. In addition, some simple trajectory models also adjust the observations to fulfill mass consistency. More sophisticated models are used by Numerical Weather Prediction centers to do accurate analysis on a synoptic scale. Several models are available to calculate back trajectories. In this study, HYSPLIT model was used to calculate the backtrajectories.

HYSPLIT, an acronym for Hybrid Single-Particle Lagrangian Integrated Trajectory, is a model developed by NOAA (National Oceanic and Atmospheric Administration) to calculate forward trajectories and backtrajectories. The model uses a Lagrangian approach to calculate advection and diffusion, and an Eulerian approach to calculate concentrations. While the initial version used just radiosonde data as inputs, the current version (Version 4) takes inputs from gridded meteorological data (obtained either from models or short forecasts). The model can be run interactively using the READY interface and can calculate trajectories from multiple heights within a layer. A detailed description of the model can be found in Draxler and Hass (1998).

Although back trajectories are computed using sophisticated methods and initializing from advanced models, their results are uncertain. Some sources of errors in computation of trajectories include: (a) truncation errors (errors due to approximation of the Taylor series expansion), (b) Interpolation errors (errors arising from the interpolation of wind data), (c) other errors such as errors relating to assumptions in estimating the

vertical wind fields. A detailed analysis of the accuracy of trajectory analysis can be found in Stohl (1998). The other drawback of a back trajectory is that it assumes that an aerosol layer has originated from a single aerosol event. Also, it is difficult to guess where the aerosol has originated from in the absence of a record from satellites (in case of strong aerosol events such as forest fires) or chemical fingerprinting.

However, with the knowledge of back trajectories and synoptic charts it is possible to determine the "pathways" that an aerosol takes to reach to Barrow, Alaska. This is accomplished by analyzing the air flow patterns to Barrow at standard pressure levels, and comparing the synoptic features with the back trajectories, obtained by inputting the aerosol layer heights, from the MPL, into the HYSPLIT model.

3.2 Synoptic Charts and Reanalysis

To study general air flow patterns at standard pressure level surfaces, and determine the important synoptic features, reanalysis models from NCEP/NCAR were used. A "reanalysis" is done offline with a meteorological field that does not change over the period of time the analysis is made. Also, it is homogenous temporally. The NCEP/NCAR reanalysis provides long term means (climatologies) that can be used to more easily understand the important synoptic features, apart from the intermittent features that occur in the daily charts. A geostrophic flow is assumed in the analysis, where the pressure gradient force is balanced by the Coriolis force. This assumption is justified as the study relates to long term transports to Barrow, where the Coriolis force is not weaker and the temporal scale is large. In the northern hemisphere, the air circulations are counterclockwise and parallel to the isopleths of a low pressure system,

and clockwise and parallel to the isopleths along a high pressure system. Normally, a mean high pressure represents a quasi-static system (low daily variation), whereas a mean high pressure system represents a dynamic system with a high possibility of deep cyclone movement (Petterssen, 1950).The pressure surfaces considered are 850mb, 700mb and 500mb. The 850mb is selected as the lowest level (to surface) as it simplifies the analysis by taking out geographical considerations such as mountains and low-level plains.

3.3 Important Synoptic Features Affecting Barrow, Alaska

In this section a review of the important synoptic features from the literature (Barry and Carleton 2001) is presented.

3.3.1 Siberian High

The Siberian high is a strong semi-permanent synoptic feature centered about 45°N-50°N, 90°E-110°E. It plays an important role in the winter climate of East Asia, and is responsible for the lowest temperature and highest pressure recorded in the Northern Hemisphere. This cold high-pressure feature is apparent in the mean surface chart, but is poorly represented in the higher level charts. The cold highs move eastward from southern Europe to Central Asia and southeastward into the Pacific Ocean (from 30°N-50°N). In summer, a low-pressure system replaces the Siberian High pressure feature. The intensity of the Siberian high has decreased since 1980, in accordance with the global trend.

3.3.2 Icelandic Low

The Icelandic low is a sub-polar low pressure feature located near Iceland. It is centered between 55°N-70°N, 10°E-60°W, and varies daily in its position and intensity. This feature weakens (and sometimes, splits) in the summer. It also has a seasonal east-west movement from 30°W (February-April) to 70°W (July-August). It is responsible for the cyclones over the east of Greenland.

3.3.3 Arctic High

Helmholtz argued the presence of a high pressure (at the surface), below the cold tropospheric polar vortex, citing dynamical reasons. This was extended by Hobbs, who developed the "glacial anticyclone" theory. However, modern theory backed with observations has diminished the importance of the "glacial anticyclone" theory. The Arctic high is a weak high pressure feature over the Arctic basin. This feature can be seen in the surface charts in early autumn, summer and late spring. According to Barry and Carleton (2001), "During winter there is usually a ridge of high pressure over Beaufort-Chuchki-East Siberian seas linking centers over Siberia and the Mackenzie-Yukon, with a trough over the Barents Sea."

3.3.4 Aleutian Low

The Aleutian low is a very strong low pressure feature over the Aleutian Islands (Alaska). The intensity of the low pressure is maximal in winter and it is one of the main centers of action as the cyclones in the sub-polar latitudes reach a maximum at the Aleutian low. Though statistical in nature, it can be used in synoptic typing of various flow patterns.

3.4 850 mb Analysis

A comparison of the climatology of 850mb and 1000mb is first made to show that the patterns are different. The plots representing climatologies and the three year composite mean of NCEP/NCAR reanalysis are presented in Appendices A and B, respectively. The climatology of surface charts indicates the presence of the aforementioned synoptic features. The Siberian high is present most of the time in winter, and is replaced by a low in summer.

The prominent features of the climatology at the surface level include: (1) a high over Greenland during most parts of the year, replaced by the one of the Icelandic lows; (2) presence of Icelandic low over the entire year with low intensities and splitting during summer; (3) absence of the Aleutian low in the summer months, and elongation during winter months.

While some features at the surface level are reflected in the 850mb level, the plot looks completely different with the visibility of the polar vortex at the 850mb level. The polar vortex is a persistent low pressure feature that can be seen in the middle and upper tropospheric charts. Also, a few features are under-represented at that level. For example, the high feature north of eastern Alaska and western Russia is not seen in the summer.

The three-year composite mean plots show little structural variation with the cilmatologies, indicating that only small structural anomalies are present.

In the late summer (Fig 3.2) at the 850mb level, the high pressure system over northwestern Alaska and northeastern Russia is absent and a single strong low pressure system with elongated troughs centers around the pole. One of the elongated troughs

(over the Chukchi and Bering Sea, hereafter referred as the mid-Pacific trough) strengthens to form a low pressure feature, which moves southward to form the Aleutian low feature. The two low pressure features (one at the pole and the Aleutian low) are separated by a high pressure feature, which peaks in February.

Hence the synoptic features that are of interest for aerosol transport to Barrow are: (a) the mid Pacific trough created by the elongation of the low over the pole, (2) the Aleutian Low and (3) west Canadian ridge. Both the position and alignment of these synoptic features are important in determining the possibility of aerosol transport to Barrow.

3.5 700mb Analysis

The climatology and the three year composite mean at this level reveal the intensification and elongation of the west Canadian ridge over the northeast resulting in a the poor representation of the north Alaskan high, absence of the mid-Pacific trough (except for August), and a only a brief presence of the low over the Aleutian islands.

This lends to the conclusion that a zonal flow to Barrow is only possible during the summer, and a strong meridional flow from the south exists for most parts of the year.

3.6 500mb Analysis

At this level, only wave patterns are visible, with the West Canadian Ridge as a prominent synoptic feature. The flow to Barrow is zonal in summer, meridional in winter, and has both components during autumn and spring.

3.7 Synoptic Types

From the analysis of the climatology and the three-year composite mean re-analysis charts, it can be concluded that the synoptic features that could influence aerosol transport are: (1) the West Canadian Ridge, (2) the mid-Pacific trough, (3) the Aleutian Low, (3) the Siberian High, (4) the high over the north of Alaska.

The comparison of the back trajectories and the re-analysis charts yields the following four commonly seen flow types:

(i) Synoptic type a – Flow from the south

The flow with a positive (from the south) meridional nature, is characteristic of an upper-level flow (500mb and above). In the upper levels, the flow happens due to the intensification of the mid-Pacific trough and/ or intensification of the West Canadian Ridge and is found during most of the year. The flow can also be seen at lower levels, mostly during summer. At lower levels, the flow is caused by the deepening of the mid-Pacific trough, and sometimes is also coupled with the presence/intensification of the Aleutian low. It is important to note that the high over north of Alaska is not present when such a flow occurs. Though the flow is one of the mechanisms for Asian dust transport to Barrow, we seldom see a transport occurring from the south. At lower levels, the same flow pattern is responsible for the transport of Alaskan forest fire smoke to Barrow.

(ii) Synoptic type b – Flow from the west

The flow from the west is a typical summer pattern easily recognizable from the 500 mb charts. The strong zonal flow to Barrow is normally characterized by the

weakening or absence of the mid-Pacific trough and the high over the north of Alaska. The flow is responsible for the transport of Siberian smoke to Barrow during summer.

(iii) Synoptic type c – Flow from the southwest

The mid-Pacific trough is responsible for the southwest flow to Barrow. The presence/intensification of the Aluetian low can intensify the flow. It is an alternate pathway for the aerosols that originate or come from the direction of Russia.

(iv) Synoptic type d – Flow from the north

The high over the north of Alaska, which forces the winds to flow in the clockwise direction around it, is primarily responsible for the flow from north.

(v) Synoptic type e

The combination of two or more of the above mentioned flow patterns and any patterns that are not described above are categorized into this type.

Chapter 4 Results

The main focus of this research is to identify the days with aerosol layers detected with the MPL data and to find the flow patterns associated with their transport to Barrow. A few case studies are presented below to support the results.

4.1 Case Studies

In this section, documented events of aerosol transport from the NASA visible Earth satellite gallery (http://visibleearth.nasa.gov/) are analyzed. The aerosol heights are determined from the lidar image by using the "detection algorithm" (described in the previous chapter) and confirming them through visual inspection. A backtrajectory plot for the aerosol height is obtained from the HYSPLIT web READY interface, and the synoptic factors responsible for the transport are studied using the NCEP/NCAR re-analysis charts. The description of the aerosol events (with their satellite images) from the Moderate Resolution Imaging Spectroradiometer (MODIS) webpage is included in the CD-ROM.

4.1.1 Siberian Fires

Forest fires are one of the important aerosol sources during summer in the Northern Hemisphere. During the 2003 fire season, wildfires spread across Siberia, East Russia, north-east China and northeast Mongolia. According to the Global Fire Monitoring Network, around 55 million acres were annihilated in the Russian Federation alone, setting a fire record for the year. A satellite image of the fires in Siberia, taken by MODIS sensor aboard Terra satellite on July 18, is shown in Fig 4.1. The smoke layer is

visible on the lidar images from July19-21. Figure 4.2 shows the lidar image for 20 July 2003.

The synoptic charts (Figures 4.3 – 4.6) at both the 700mb and 850mb levels indicate a zonal flow from the west, backed by the trajectory analysis (Figure 4.7).

4.1.2 Alaskan Smoke

The smoke season in Alaska starts in mid-April when the ice melts, and can last until late August. In the summer of 2004, Alaska witnessed one of the worst wildfire seasons in history. The smoke spread all across North America, even entering the Atlantic, registering one of the highest values of EPA's Air Quality Index (measured over Fairbanks) registered in the United States. Fig 4.8 shows the MODIS satellite image of Alaska on 21 August 2004, with red dots representing the wildfire "hot" spots. Fig 4.9 shows the lidar image at Barrow on 24 August 2004, with aerosol layers from 4.0 to 6.0 km.

The synoptic charts (Figures 4.10 and 4.11) representing the composite mean for the period of the aerosol transport (August 22-24, 2004), shows a high pressure system near Barrow. It indicates a clockwise direction of air flow from the Bering Strait to Barrow. Also, the daily composite mean charts indicate an intensification of the West Canadian ridge into a high pressure system, suggestive of the trajectory (Fig 4.12) indicated by the HYSPLIT backtrajectory model.

4.1.3 Asian Dust

In the springtime, intense windstorms occur in southeastern Asia, which pass through the Gobi and Taklamakan deserts and carry suspended particles of dust. The dust

storms are so intense that winds can carry dust from these storms to Hawaii, Barrow (Alaska) and the East Coast of the United Sates, depending on the synoptic situation in the region. According to Raatz and Shaw (1984) and Rahn (1981a, 1981b, 1985), the Asian dust reaches Barrow almost every spring. Mostly, dust events loose their intensity before reaching Alaska, and hence are not seen in satellites.

Figure 4.13 shows a lidar image of an aerosol layer, from approximately 4.0 to 6.0 km, on 15 April 2004. The back trajectory analysis (Figure 4.14) leads one to believe that the aerosol is likely Asian dust. The reanalysis (Figures 4.15 – 4.19) also shows the intensification of the West Canadian ridge and the presence of a high over Alaska (accounting for a northward arrival of aerosol to Barrow), confirming the presence of favorable synoptic conditions to drive the Asian dust to Barrow. However, no direct satellite images were available to confirm the aerosol was Asian dust.

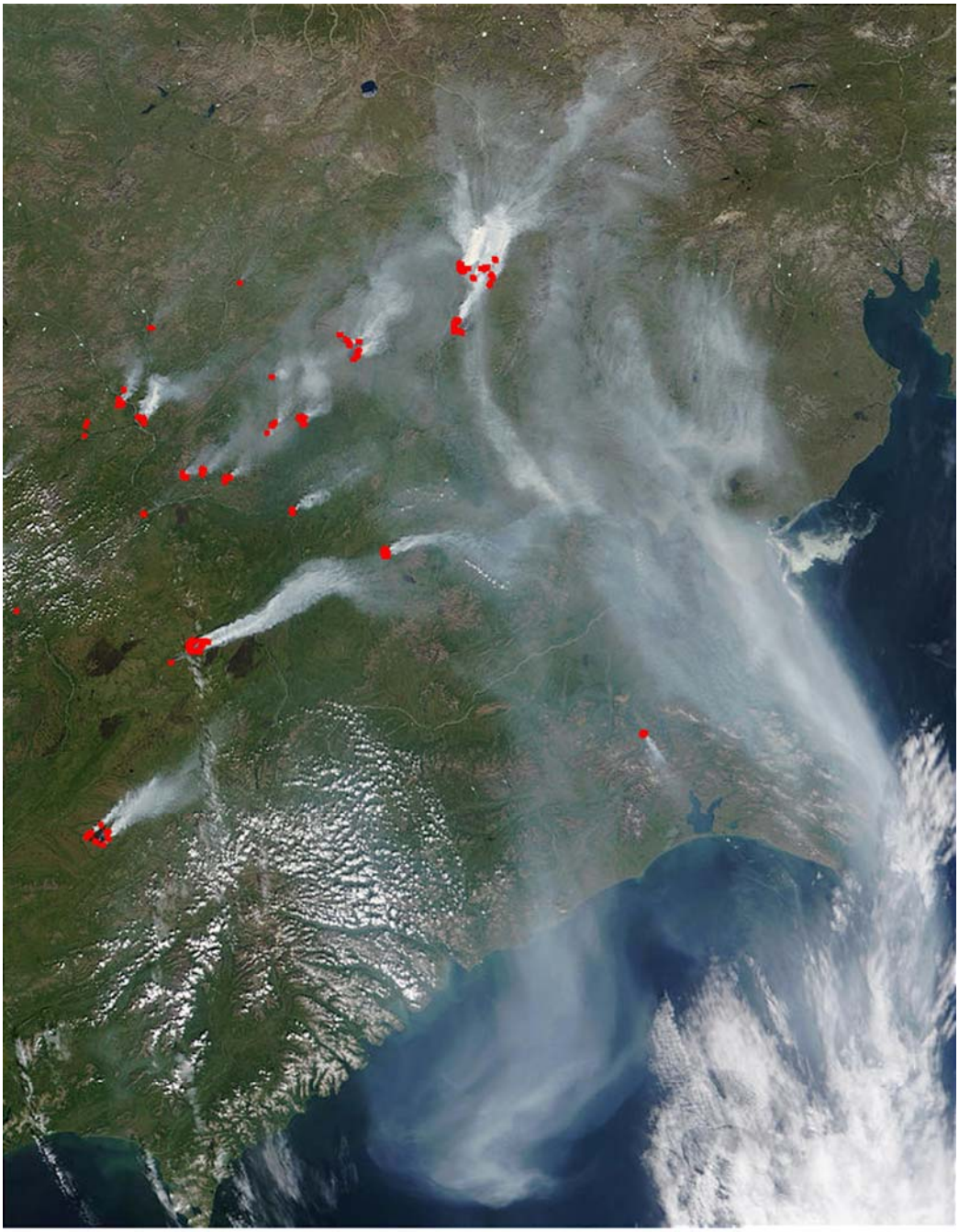

Figure 4.1: A MODIS image taken on July 18, 2003, showing fires (marked in red) in eastern Siberia.

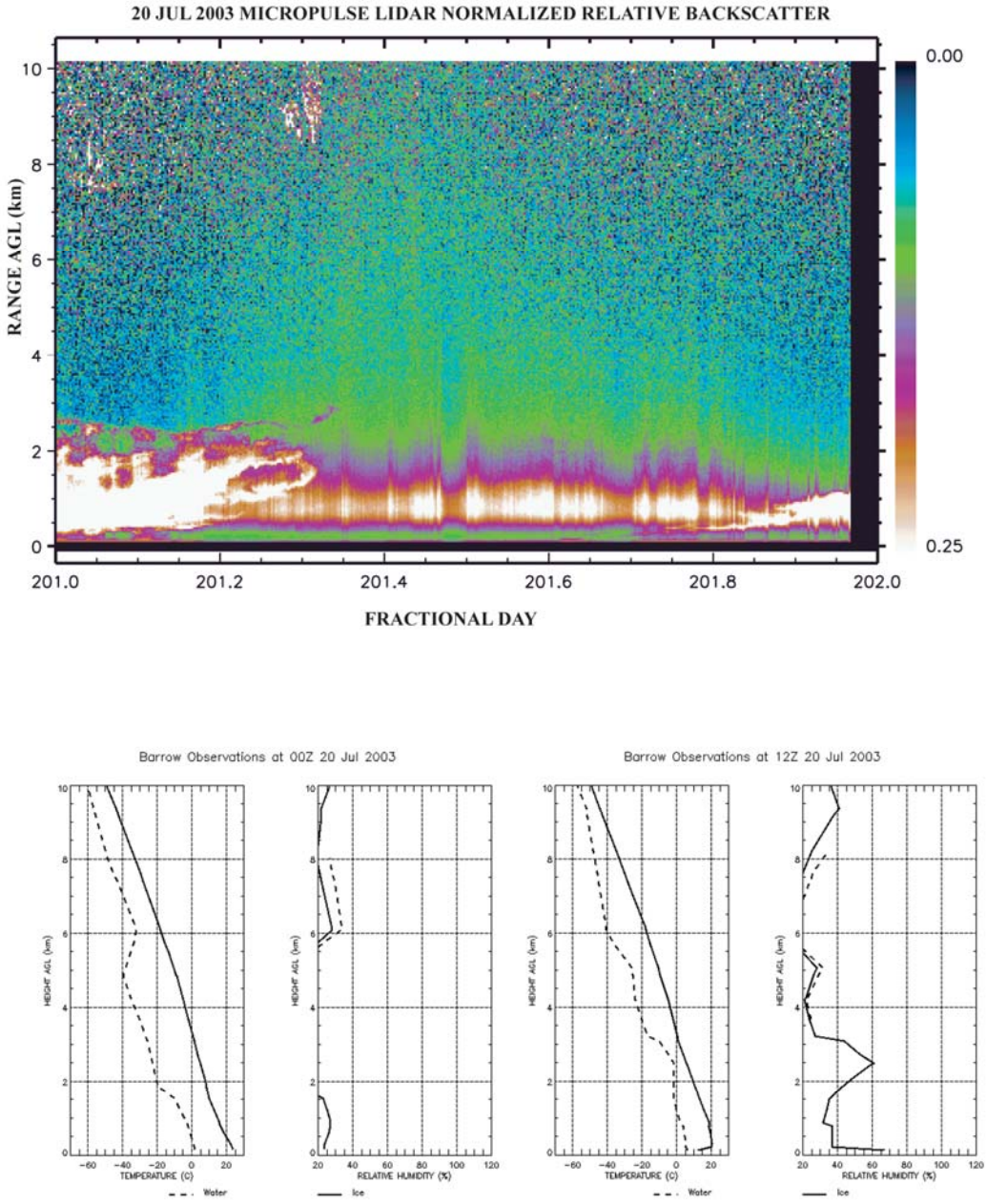

Figure 4.2: The lidar image (top) and the 00Z (bottom left) and 12Z (bottom right) soundings for 20 July 2003.

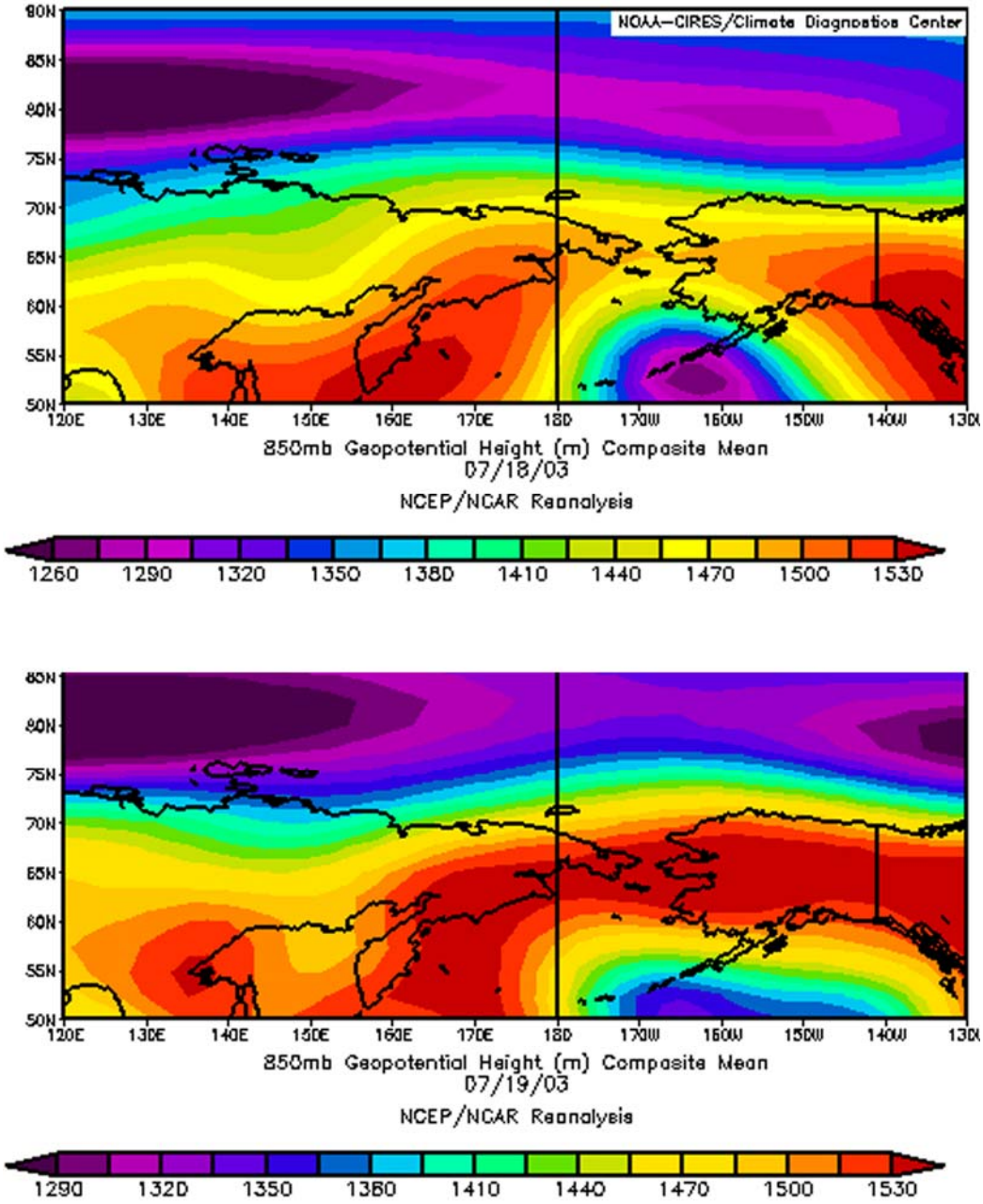

Figure 4.3: NCEP/NCAR reanalysis of the daily composite mean of the 850mb geopotential height surface for 18th and 19th July 2003.

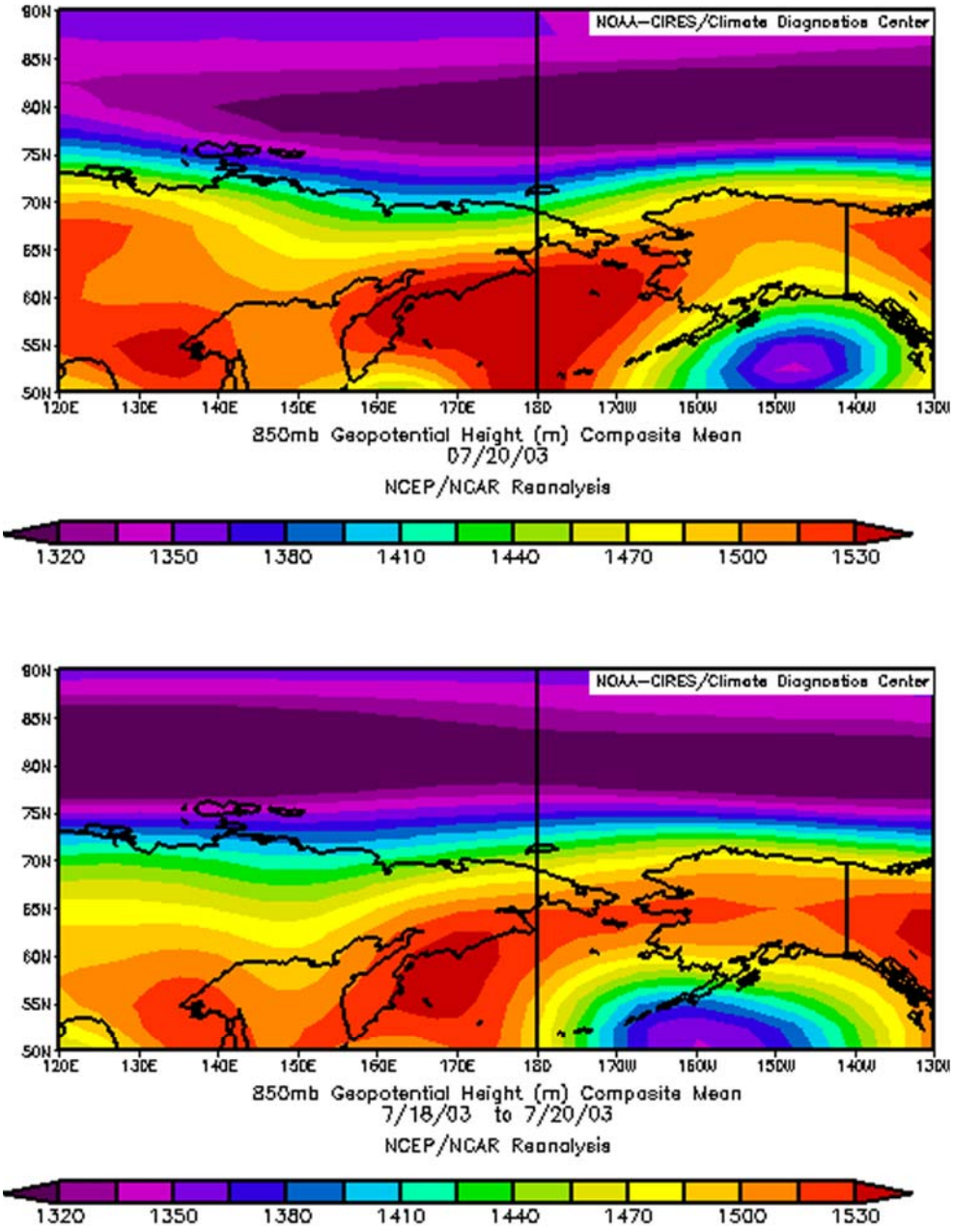

Figure 4.4: NCEP/NCAR reanalysis of the daily composite mean of the 850mb geopotential height surface for 20th July 2003 (top) and 3-day composite mean (bottom).

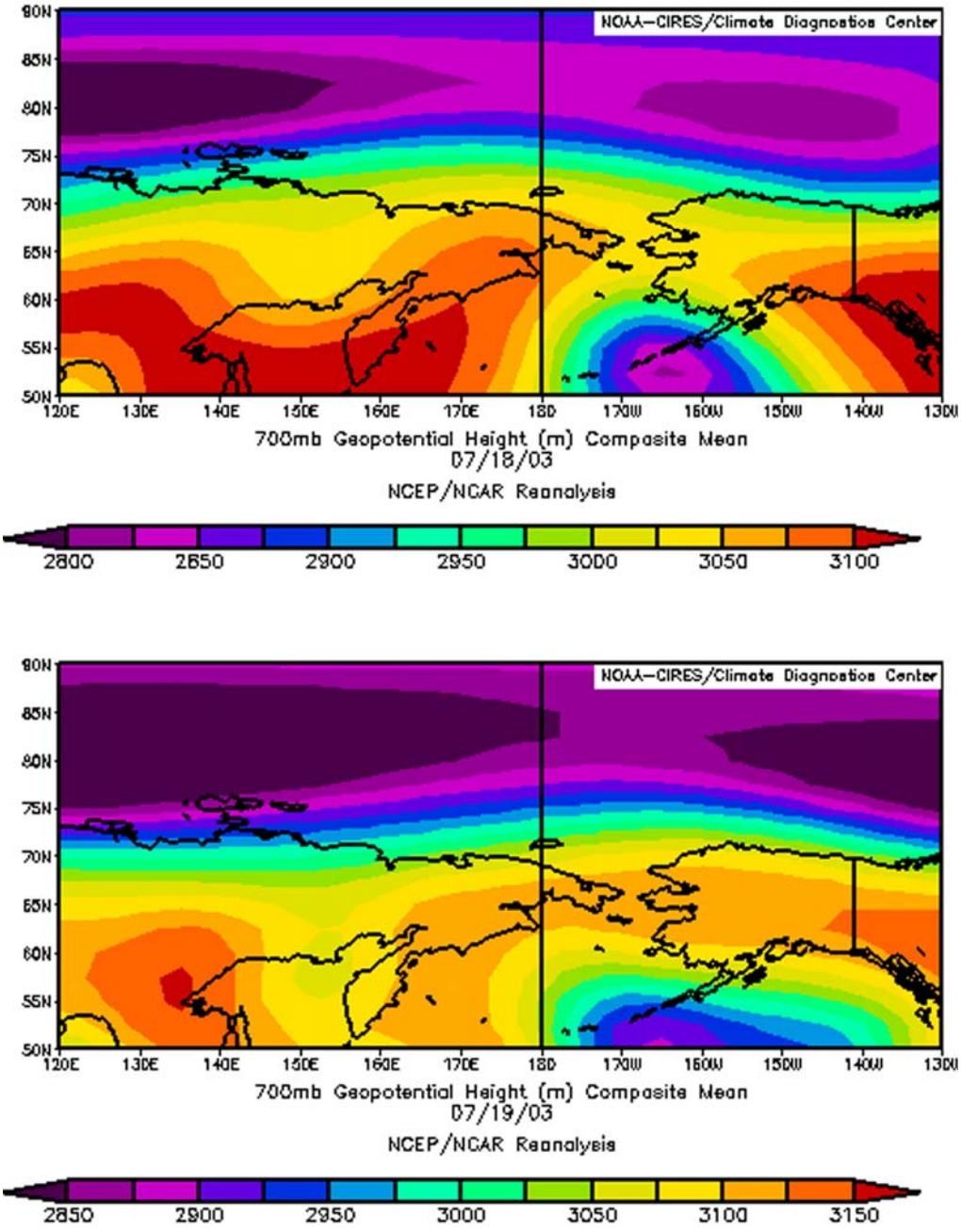

Figure 4.5: NCEP/NCAR reanalysis of the daily composite mean of the 850mb geopotential height surface for 20th July 2003 (top) and 3-day composite mean (bottom)

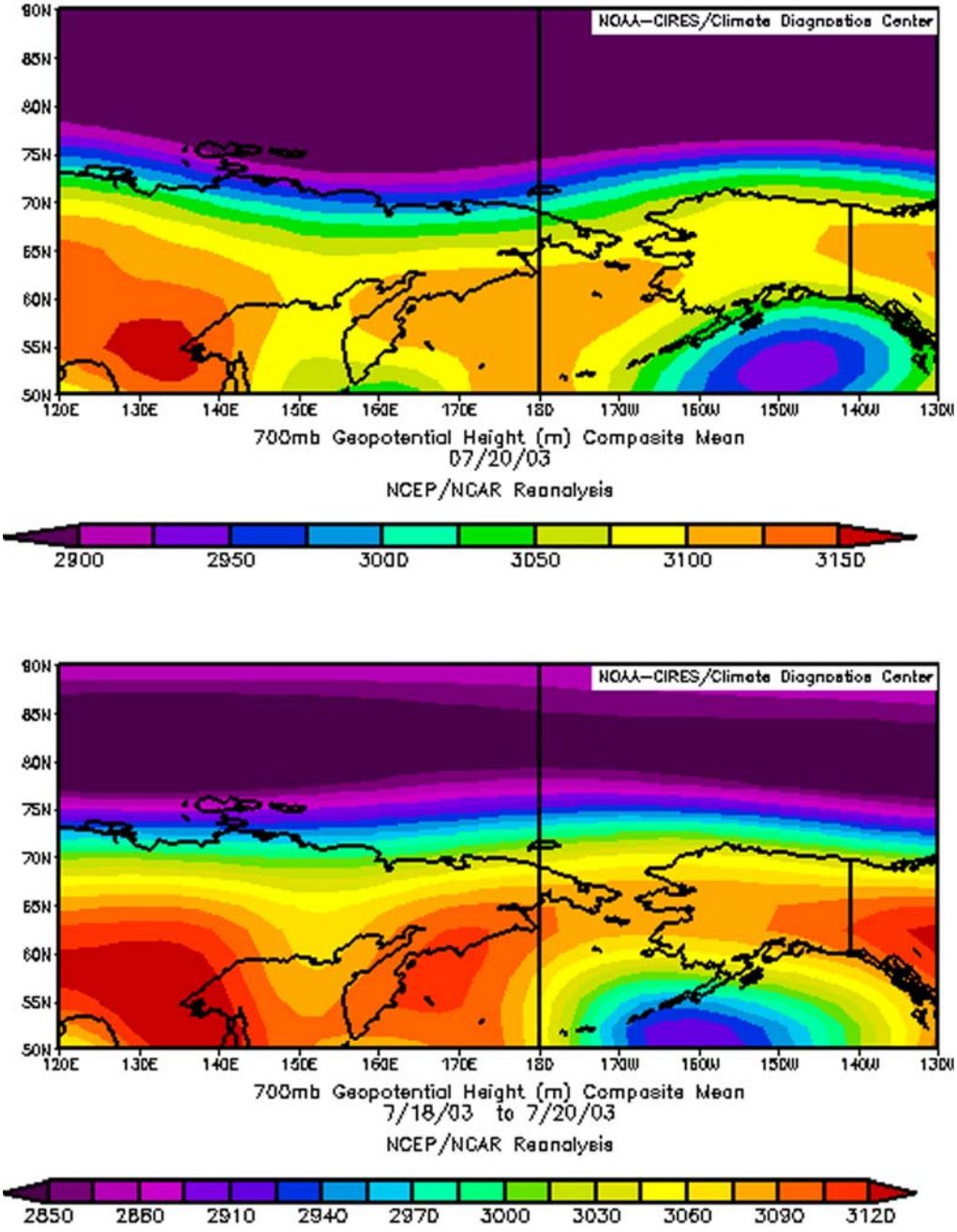

Figure 4.6: NCEP/NCAR reanalysis of the daily composite mean of the 850mb geopotential height surface for 18th and 19th July 2003.

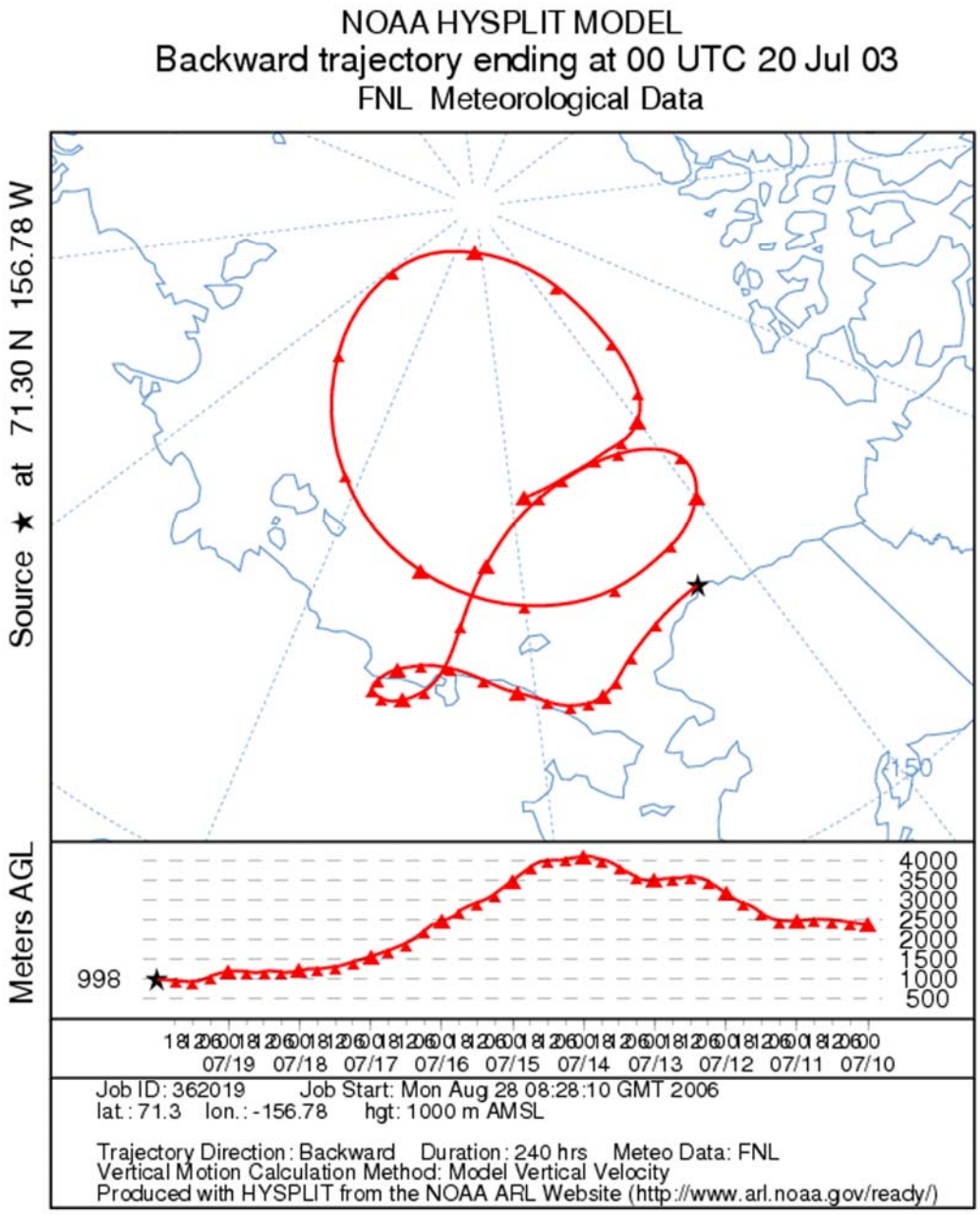

Figure 4.7: A 10 day backtrajectory analysis showing the transport path of the aerosol at 1000m (above mean sea level) ending 20th Jul 2003 at Barrow.

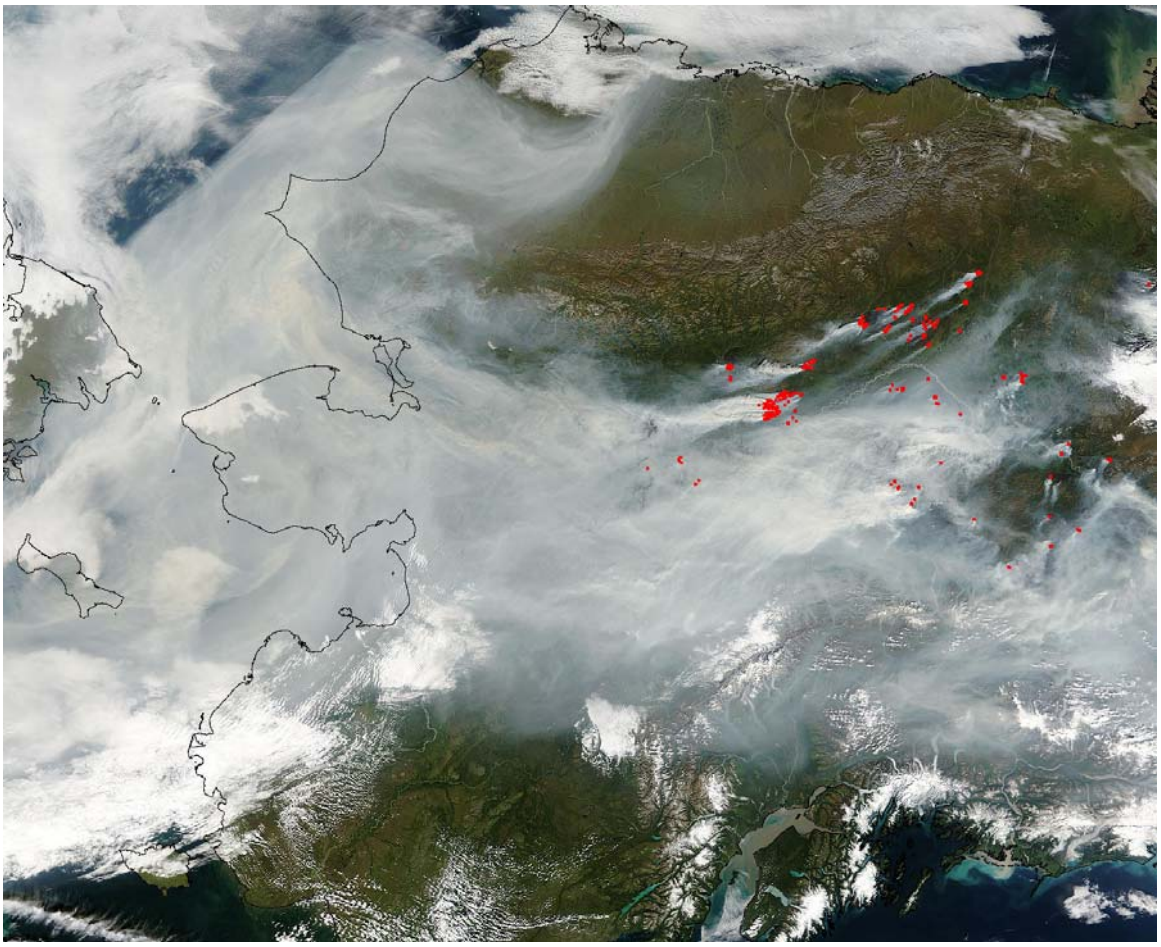

Figure 4.8: A MODIS image showing dense gray smoke in Alaska and Bering Strait on 21 August 2004.

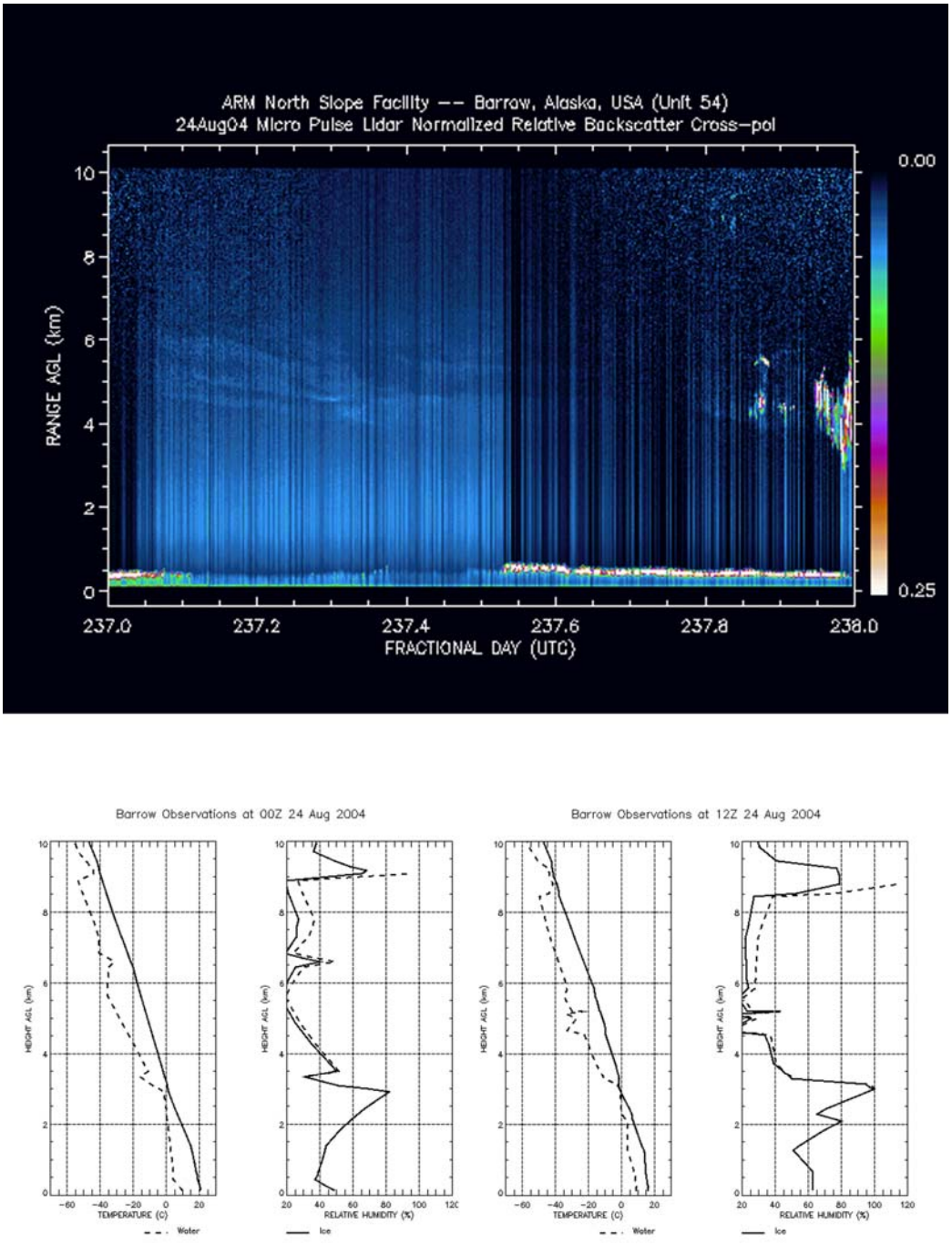

Figure 4.9: The lidar image (top) and 00Z (bottom left) and 12Z (bottom right) soundings for 24 August 2004.

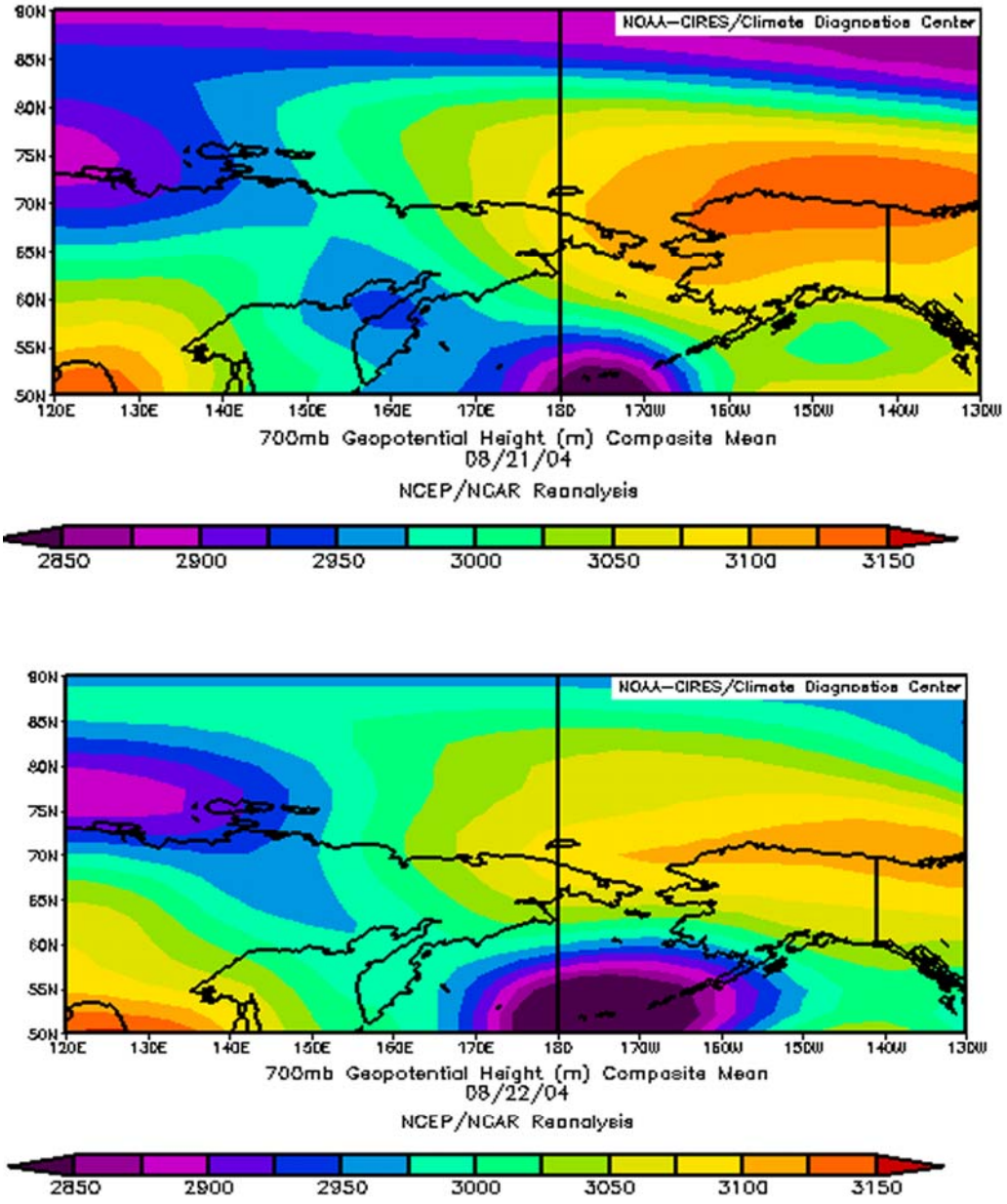

Figure 4.10: NCEP/NCAR reanalysis of the daily composite mean of the 700mb geopotential height surface for 21st and 22nd August 2004.

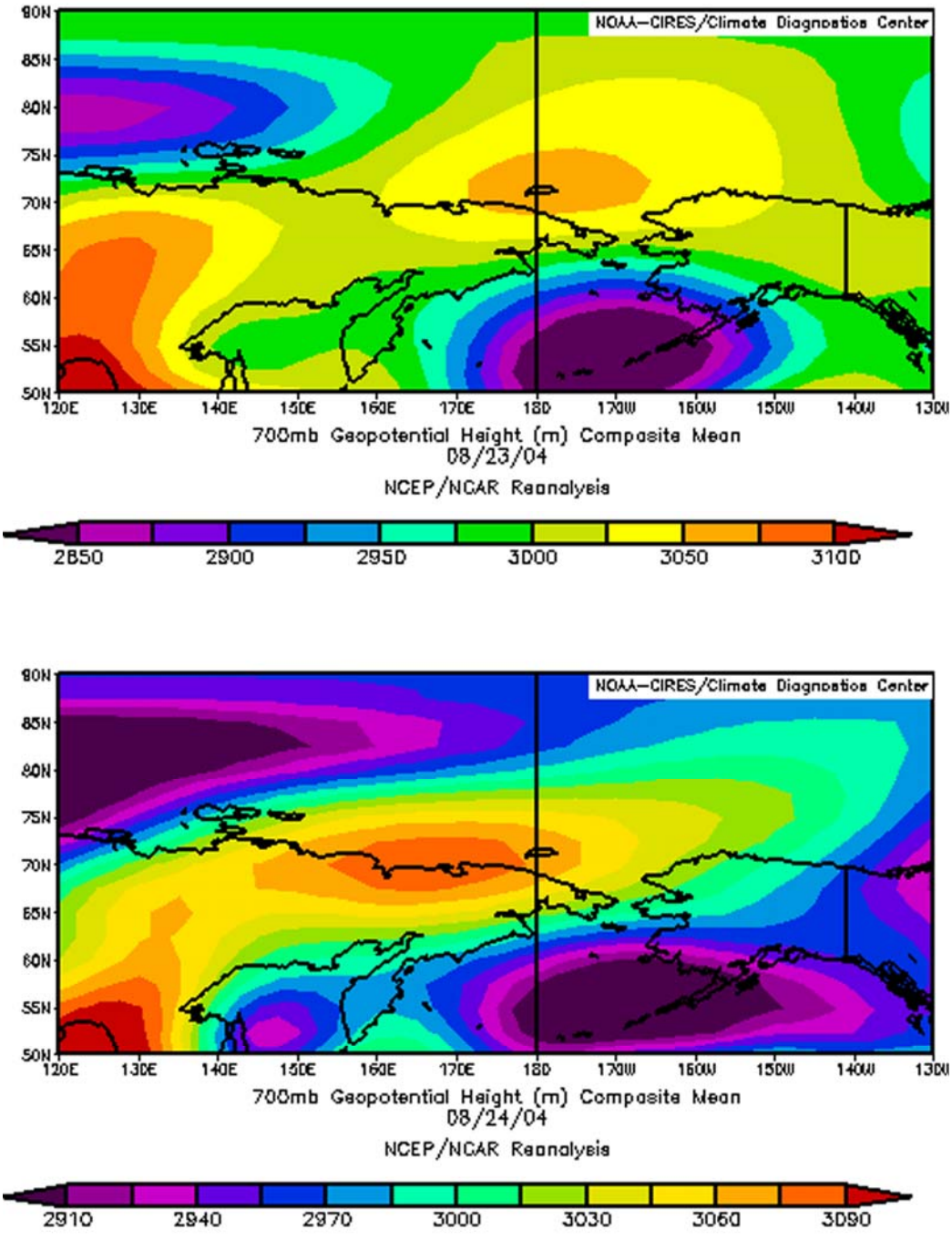

Figure 4.11: NCEP/NCAR reanalysis of the daily composite mean of the 700mb geopotential height surface for 23rd and 24th August 2004.

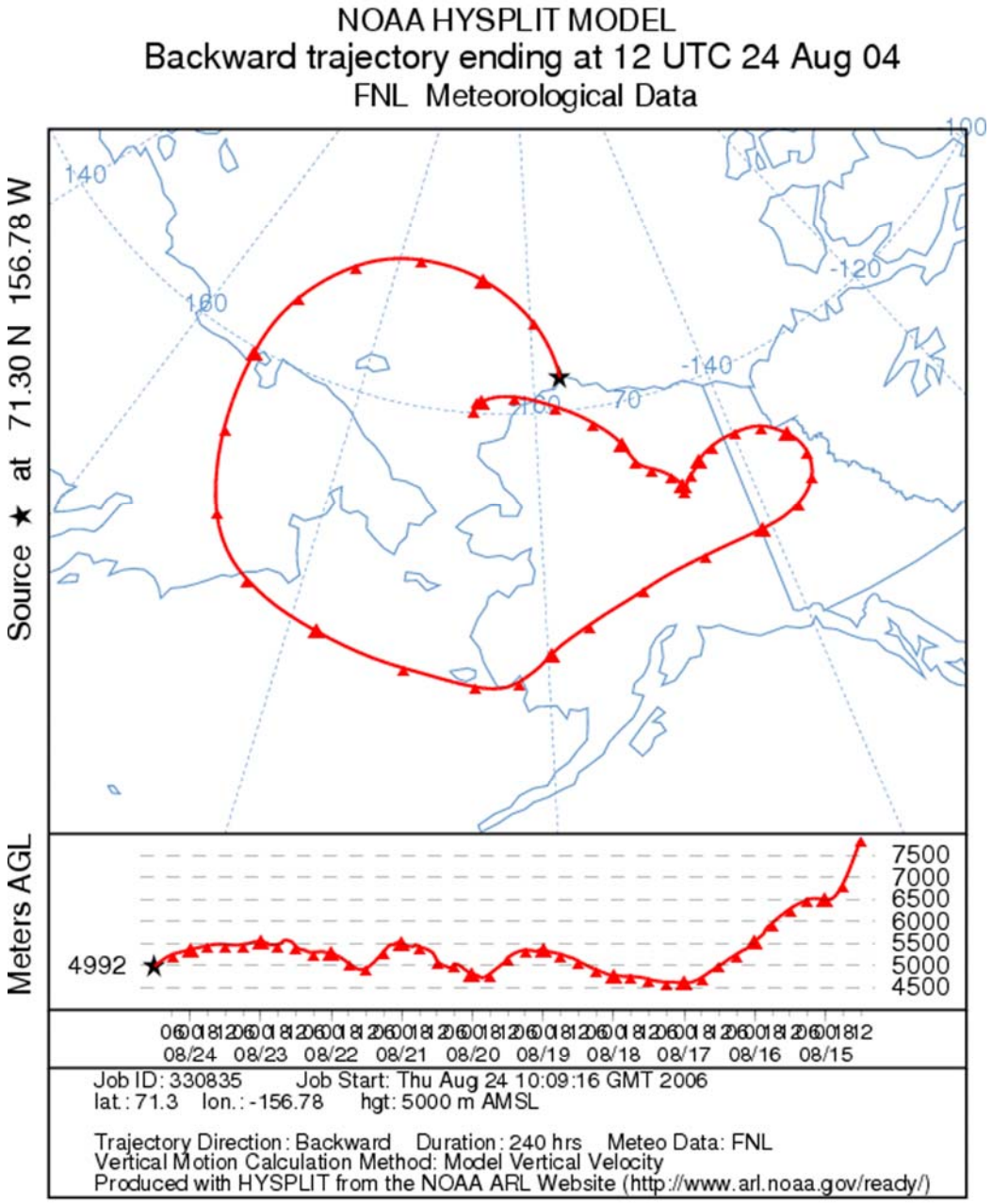

Figure 4.12: A 10 day backtrajectory analysis showing the transport path of the aerosol at 5000m (above mean sea level) ending 24th Aug 2004 at Barrow.

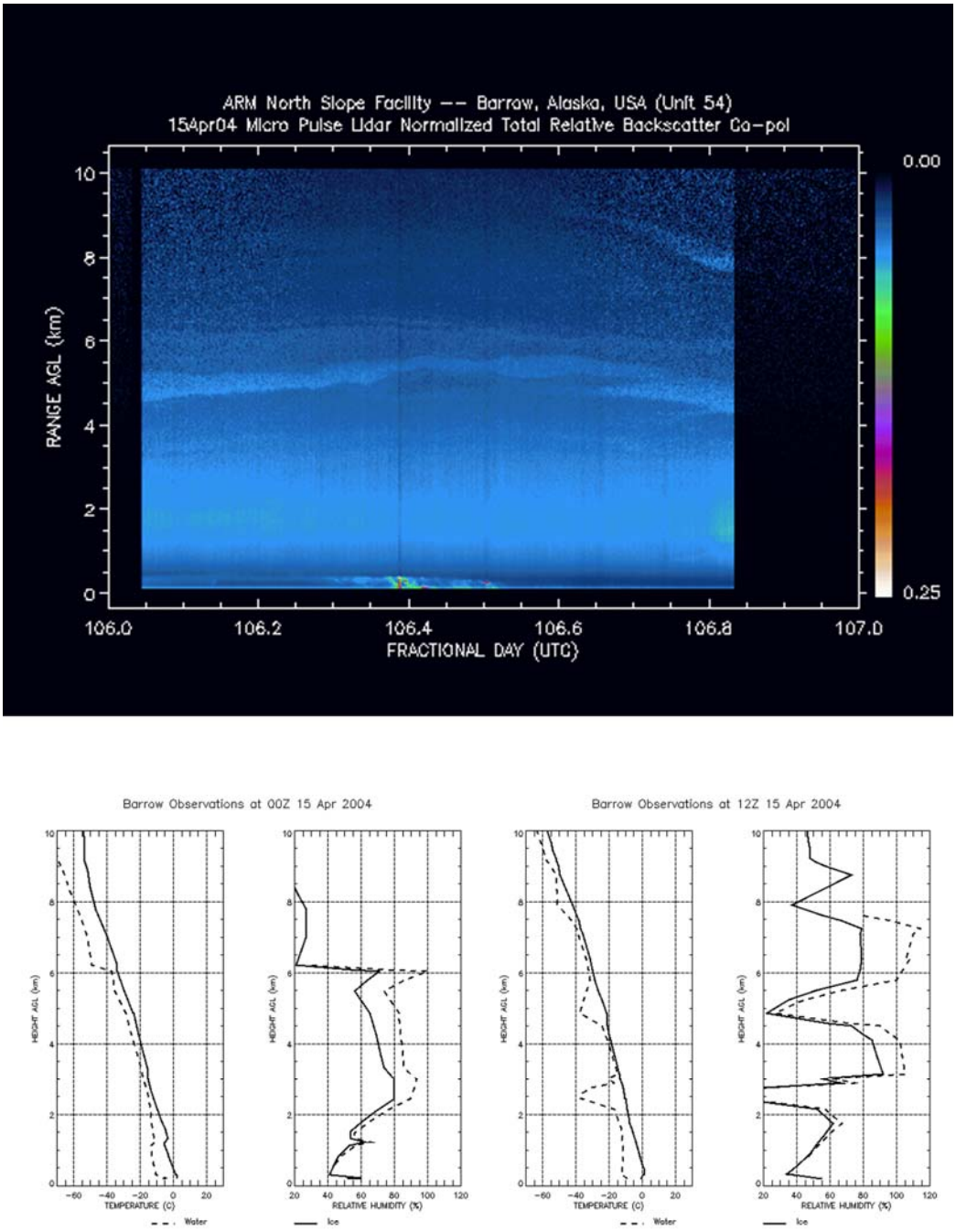

Figure 4.13: The lidar image (top) and 00Z (bottom left) and 12Z (bottom right) soundings for 15th April 2004.

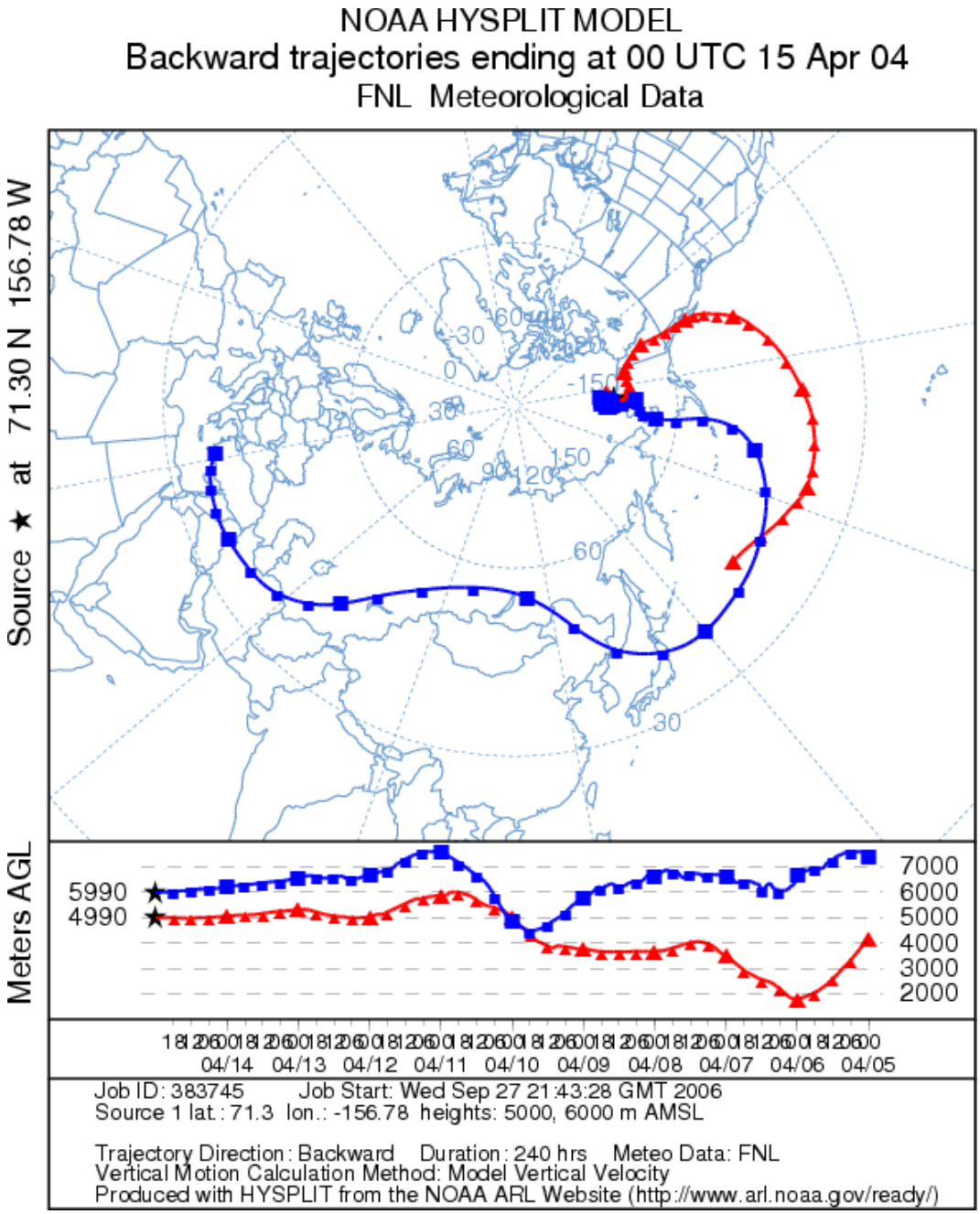

Figure 4.14: A 10 day backtrajectory analysis showing the transport path of the aerosol at 5000m and 6000m (above mean sea level) ending 15th April 2004 at Barrow.

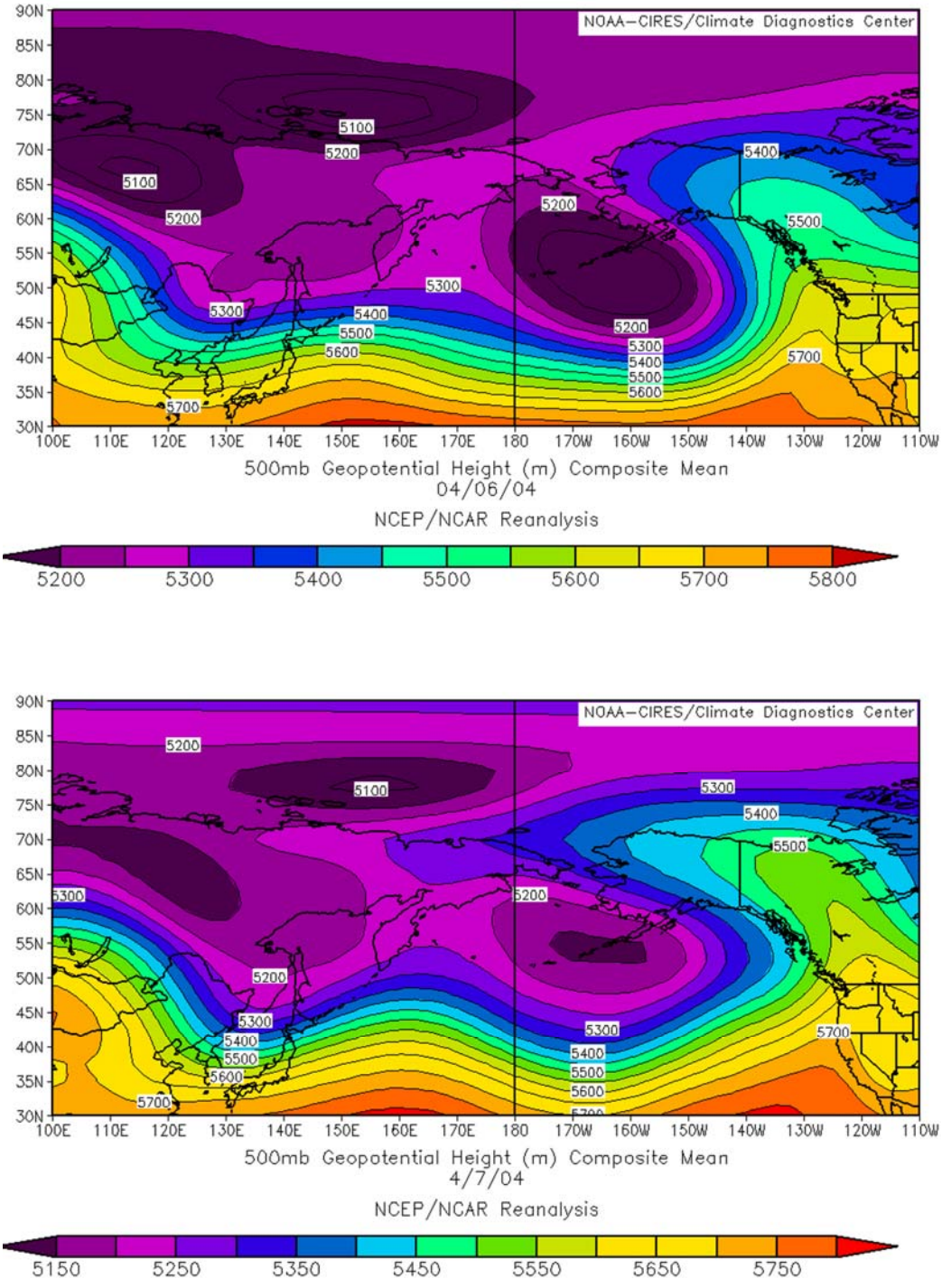

Figure 4.15: NCEP/NCAR reanalysis of the daily composite mean of the 500mb geopotential height surface for 6 April 2004 and 7 April 2004.

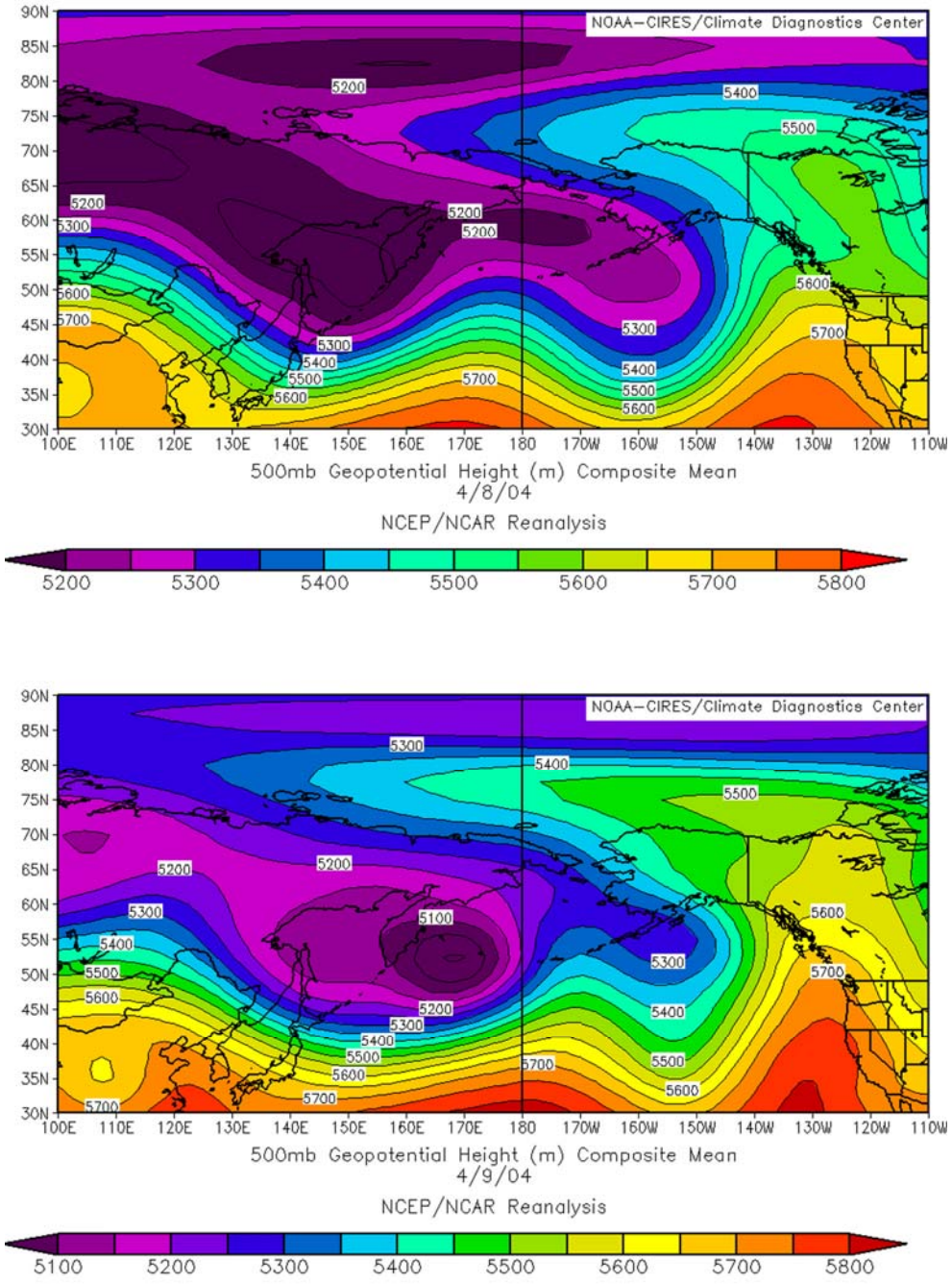

Figure 4.16: NCEP/NCAR reanalysis of daily composite mean of the 500mb geopotential height surface for 8 April 2004 and 9 April 2004.

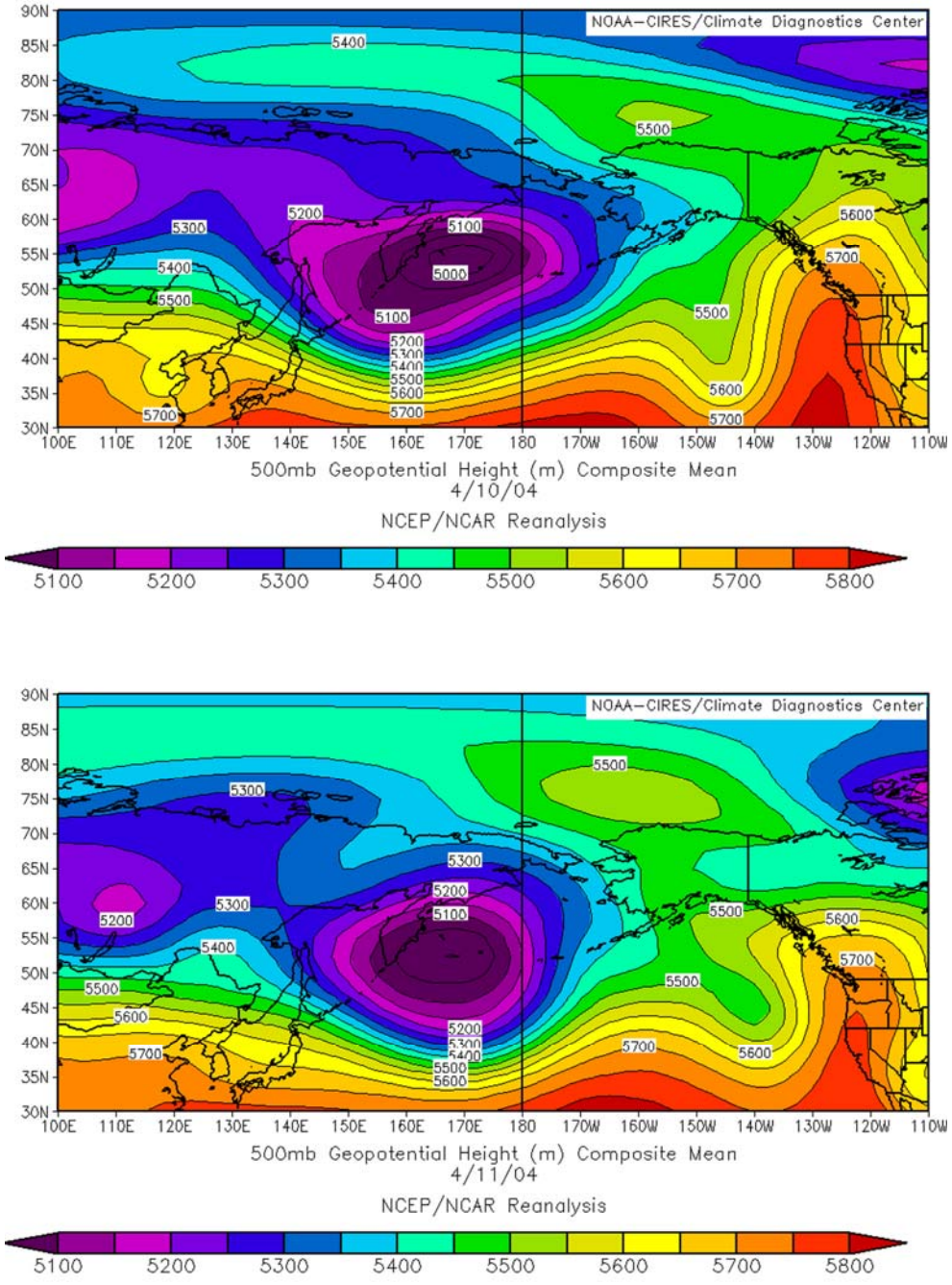

Figure 4.17: NCEP/NCAR reanalysis of daily composite mean of the 500mb geopotential height surface for 10 April 2004 and 11 April 2004.

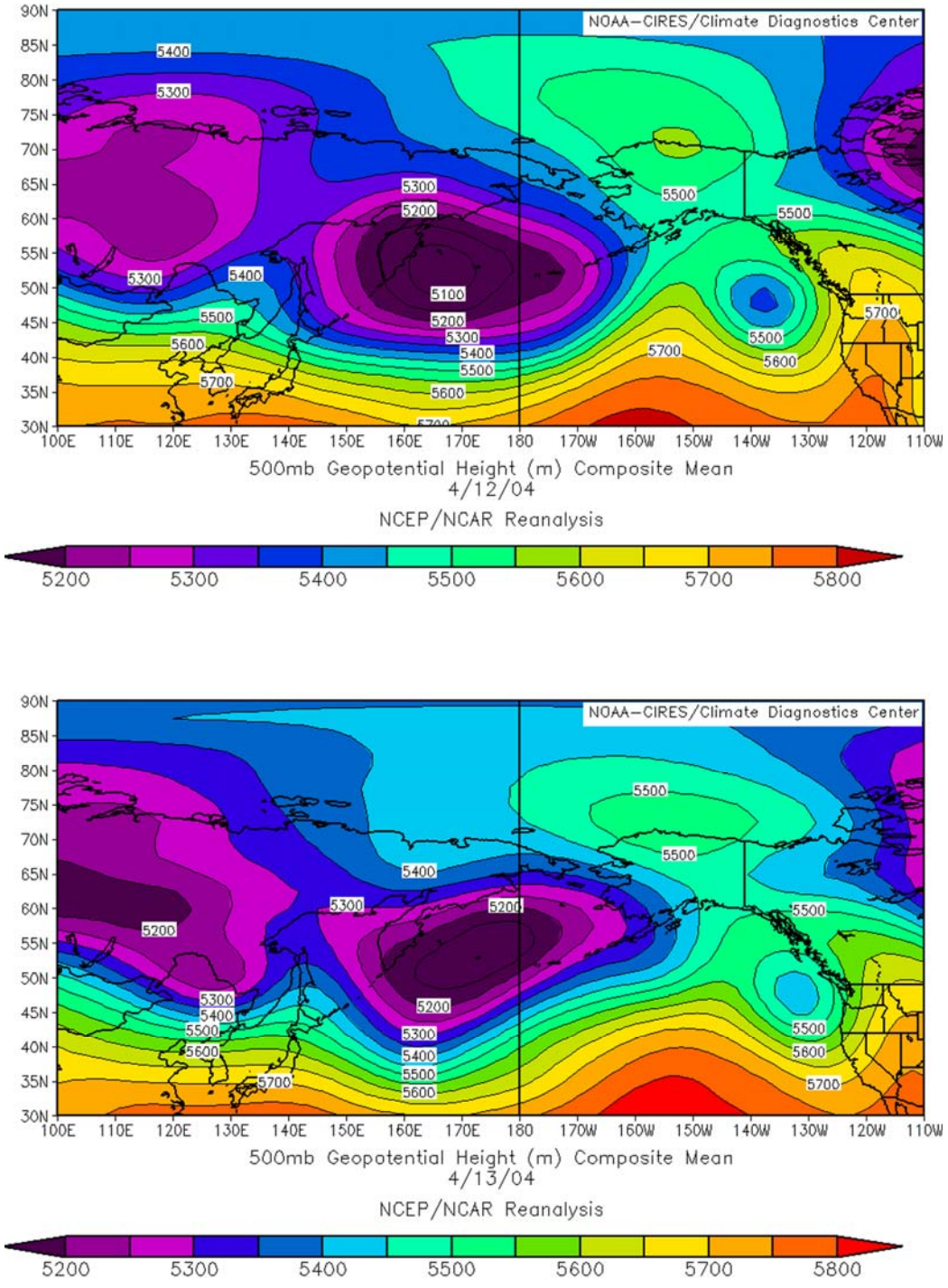

Figure 4.18: NCEP/NCAR reanalysis of daily composite mean of the 500mb geopotential height surface for 12 April 2004 and 13 April 2004.

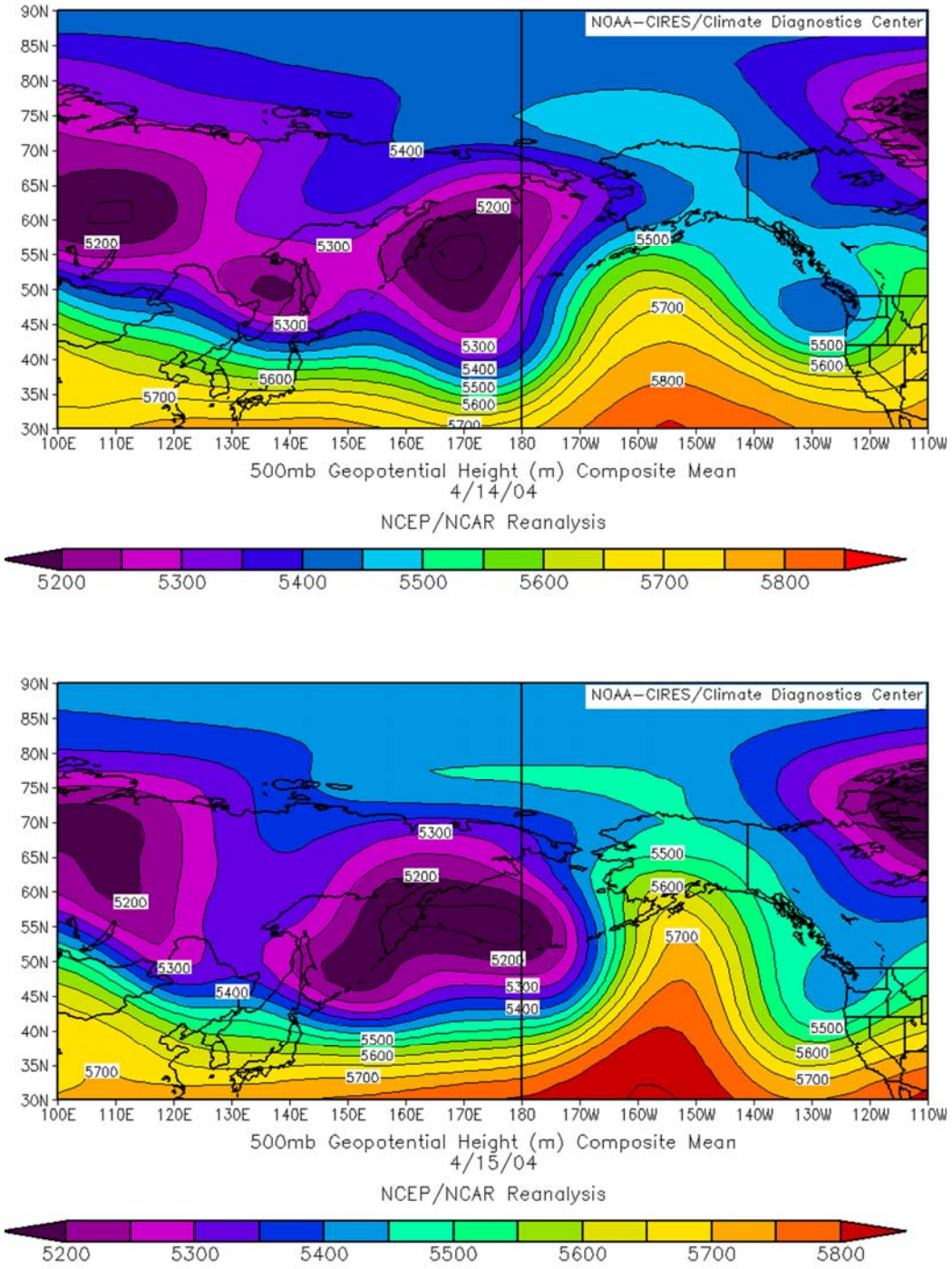

Figure 4.19: NCEP/NCAR reanalysis of daily composite mean of the 500mb geopotential height surface for 14 April 2004 and 15 April 2004.

4.2 Aerosol Picture at Barrow

To develop the aerosol picture of Barrow, the lidar data were first inspected visually, with the help of sounding plots, to identify the aerosol days from the dataset. Lidar profiles (with 0.05 Julian day averaging) were plotted for this filtered dataset. The automated aerosol detection algorithm was applied to the lidar profiles to determine the aerosol layers and their relative scattering ratios. Due to the inherent disadvantages in the algorithm stemming from the MPL performance, the profiles were visually inspected to discard thin cloud layers, and to determine the accurate aerosol layers and their "peak" relative scattering ratios. The scattering ratios calculated are relative to the Rayleigh backscatter of the molecular atmosphere at 0.532 μm and do not take into account the amount of attenuation undergone by the signal. To compare the "average scattering ratios" with the scattering intensity of the aerosol layer, the thickness of the aerosol layer also has to be taken into account. Hence, it would be best to match the average relative scattering ratio with the intensity of the aerosol layer with the "peak" relative scattering ratio to the intensity of the aerosol layer.

Figure 4.21, Figure 4.22 and Figure 4.23 show the days of aerosol events, the height of the aerosol layers (above mean sea level), their variability during the day, and the "peak" relative scattering ratios of the aerosol layers, in the three year dataset.

Before any inferences could be made from the figure, it is necessary to analyze the assumptions made, and the drawbacks of the techniques and the instrument. The plot shows only the aerosol layers visible to the lidar. Lidars normally cannot penetrate layers of optical thickness greater than 3.0. Hence, dense clouds in the bottom few kilometers

could impair the visibility of the lidar. For example, Fig 4.20 shows the number of days in a year the instrument cannot see above 2.0 km. It also includes days of bad/no data. Only in 63% of the cases does the laser reach higher than 2.0 km, which is a very low percentage. The reduced number of aerosol days while using the algorithm can be attributed to the following reasons:

1. Inability to resolve cloud layers from the aerosol layers during averaging
2. Inability of the lidar (MPL at Barrow) to see the bottom half-kilometer range
3. The threshold scattering ratio value (1.05) to identify an aerosol layer prevents detection of thin aerosol layers.

The peak relative scattering ratio calculated does not translate to any absolute optical property (such as optical depth) of the layer. Hence, the property can only be used for a case by case analysis of aerosol layers rather than the study of radiative properties of an aerosol layer over Barrow.

Figure 4.22 shows the aerosol picture of Barrow during years 2003, 2004 and 2005. It can be seen that the springtime is the peak aerosol period in all the years. Also, the higher layers of the aerosol are seen during February, March and April. During summer and early Fall, the layers are situated close to the ground. Among the three years, the (partial) year 2005 has the most aerosols (Figure 4.23).

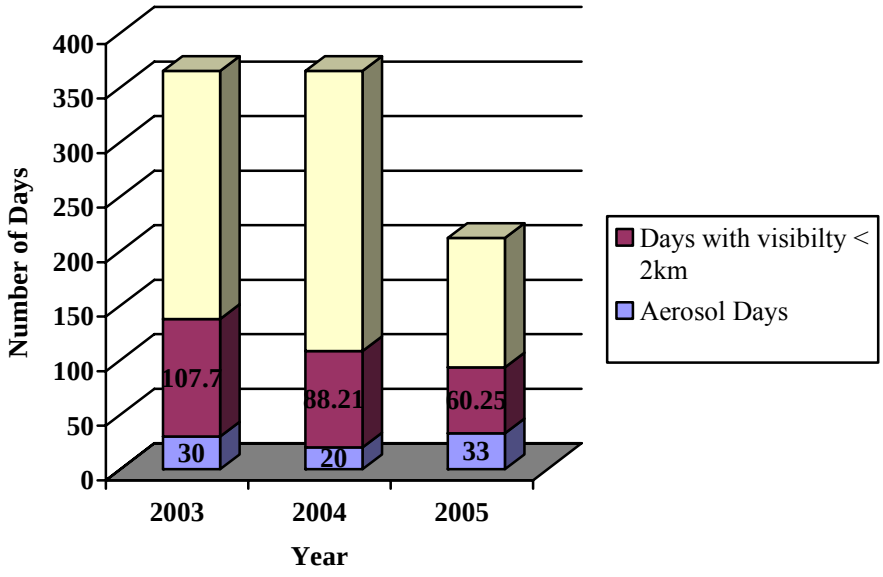

Figure 4.20: A year-wise comparison of the number of aerosol days and the visibility of the MPL (less than 2 km).

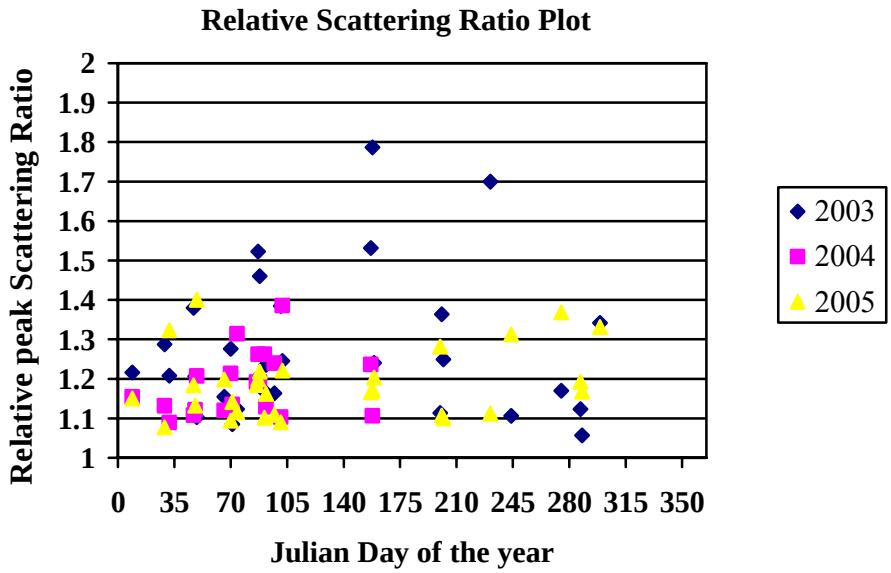

Figure 4.21: The relative peak scattering ratios for the aerosol events during 2003, 2004 and 2005.

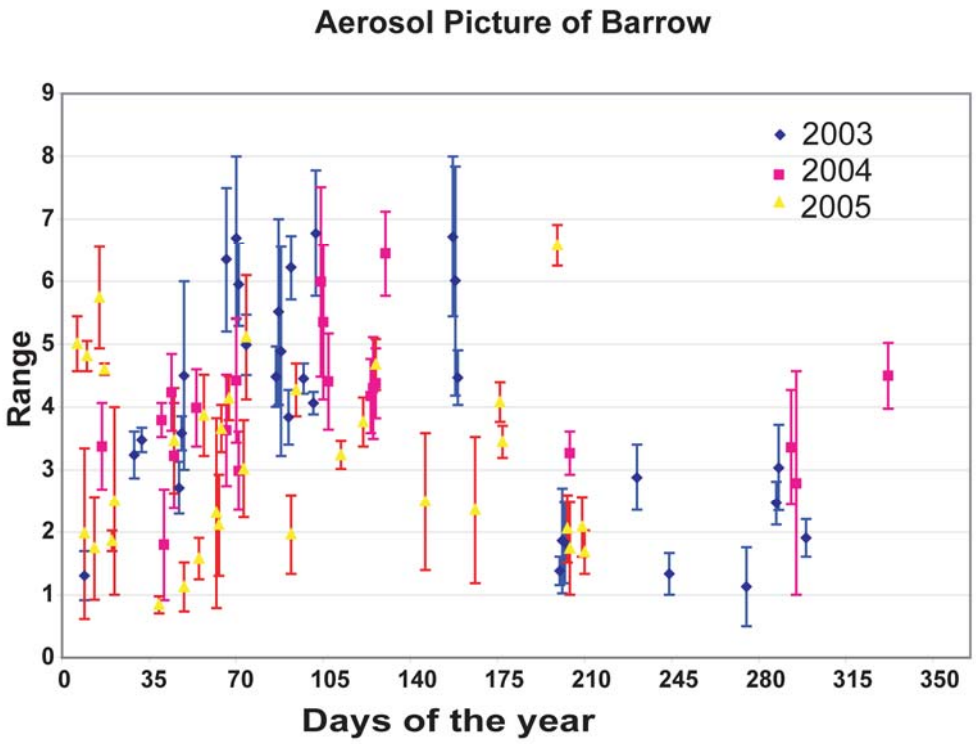

Figure 4.22: Aerosol picture of Barrow - The aerosol heights and the Julian day of the aerosol events that occurred during 2003, 2004 and 2005.

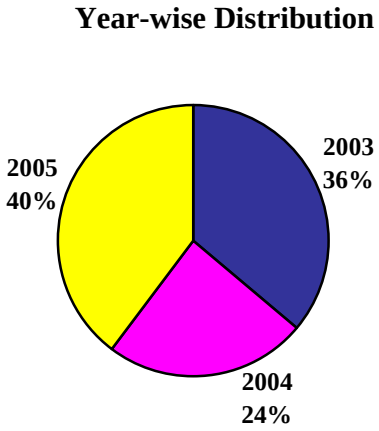

Figure 4.23: Year-wise distribution of the aerosol events

4.3 Aerosol "Pathways"

The synoptic charts at 500mb, 700mb and 850mb pressure levels for both times 00Z and 12Z were analyzed for the all the aerosol days and were categorized into the five types (as discussed in previous chapter). The backtrajectories for all the aerosol layers/ days can be found in the compact disc attached with the document.

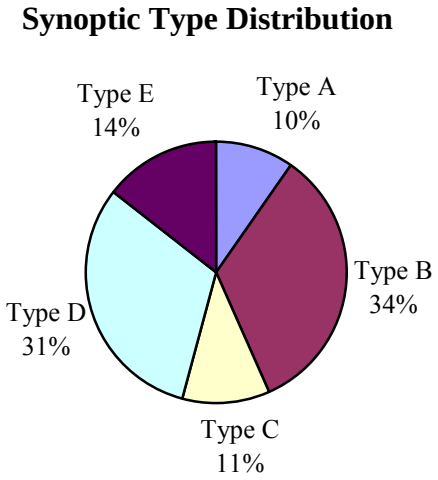

Figure 4.24: A pie-chart depicting the synoptic distribution of aerosol events

The flows from the west and north are the most important flows responsible for aerosol transport to Barrow. The flows from the south and southwest contribute less to aerosol transport.

Chapter 5 Conclusions and Future Work

According to the literature (Stonehouse 1986; Raatz and Shaw 1984; Shaw 1980; Shaw and Stamnes 1980), the main sources of aerosols that could possibly reach Barrow are (a) Asian Dust (from Gobi and Taklamakan deserts), (b) industrial pollutants from north and Eastern Russia, and (c) forest fires from Alaska and Siberian region. The other minor sources could be the strong volcanic eruptions from the Aleutian arc or the north and eastern parts of Russia.

Comparing the synoptic types with the back trajectories, the aerosol sources, and the MPL-detected elevated aerosol layers, it can be concluded that the Asian Dust events in early spring and the wildfires in Alaska and Eastern Russia in mid summer are the most important aerosol events found at Barrow. During spring, the dust storm events in Asia drive the dust aerosol into the Pacific and the strong West Canadian ridge facilitates the transport of Dust aerosol to Barrow. At lower levels (850mb and 700mb), strong zonal flow from Russia can also favor aerosol transport from Russia. During summer, a strong meridional component of flow exists; and with the occurrence of the Alaskan and the Siberian smoke events, the summer can be one of the major aerosol seasons in Barrow. During the 2004 fire season in Alaska, there were only a few detected cases. However, there were only a few cases of aerosol events reported in the late autumn. Mostly, the aerosols in this season are attributable to Arctic haze.

The drawbacks encountered were (i) the reduced tropospheric visibility and operational uncertainties of the MPL, (ii) “fuzziness” involved with the detection and quantification of aerosol layers; (iii) unavailability of other (i.e., airborne) data that could

help in chemical fingerprinting. The inability of the laser to penetrate any cloud greater than 3.0 in optical thickness is a setback in the analysis of higher layers of aerosols. Also, due to its low power and high susceptibility to noise, the MPL requires averaging for longer time periods to get a signal with an acceptable SNR. Due to the drawbacks in calculating the calibration constant of the instrument, accurate scattering ratios for the layers could not be calculated. The depolarization ratios for most of the aerosol layers were not reliable. Hence, these calculations were not used in the analysis. However, the depolarization ratio for ice clouds was around 0.4. These data were used to distinguish aerosol layers from thin ice clouds. The relative humidity data were not good in some cases (mostly when temperatures were below -35°C). During summer, there were at least a couple of events when the soundings reported less than 75% relative humidity for clouds (asserted by a strong backscatter signal from the lidar).

With some improvements in the second MPL channel, more accurate depolarization ratios could be calculated, and can be correlated to some of the aerosol sources. Also, with the presence of other instruments to calibrate (such as a more powerful traditional lidar), the MPL can be calibrated more regularly, and inversion of profiles can be done to determine some direct radiative parameters such as the optical depth. The depolarization ratios and the inversion profiles, along with chemical fingerprinting and synoptic analyses, can give a more complete aerosol picture of Barrow with their sources and pathways. Furthermore, the contributions of these aerosols to cloud cover, and hence the indirect forcing on climate, can begin to be estimated.

APPENDIX A: Climatologies

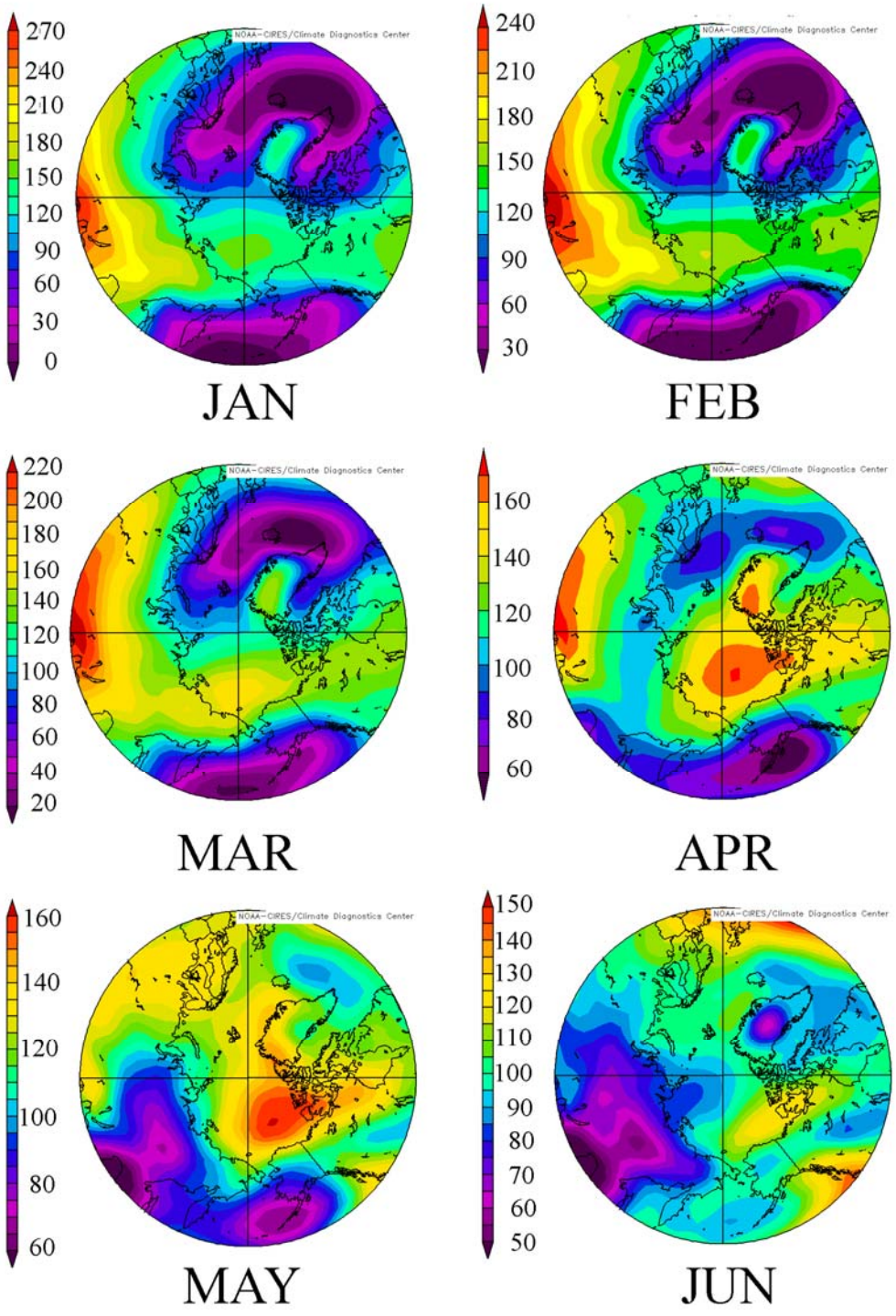

Figure A.1: NCEP/NCAR reanalysis of the 1000mb geopotential height climatology (1968-1996) from January - June.

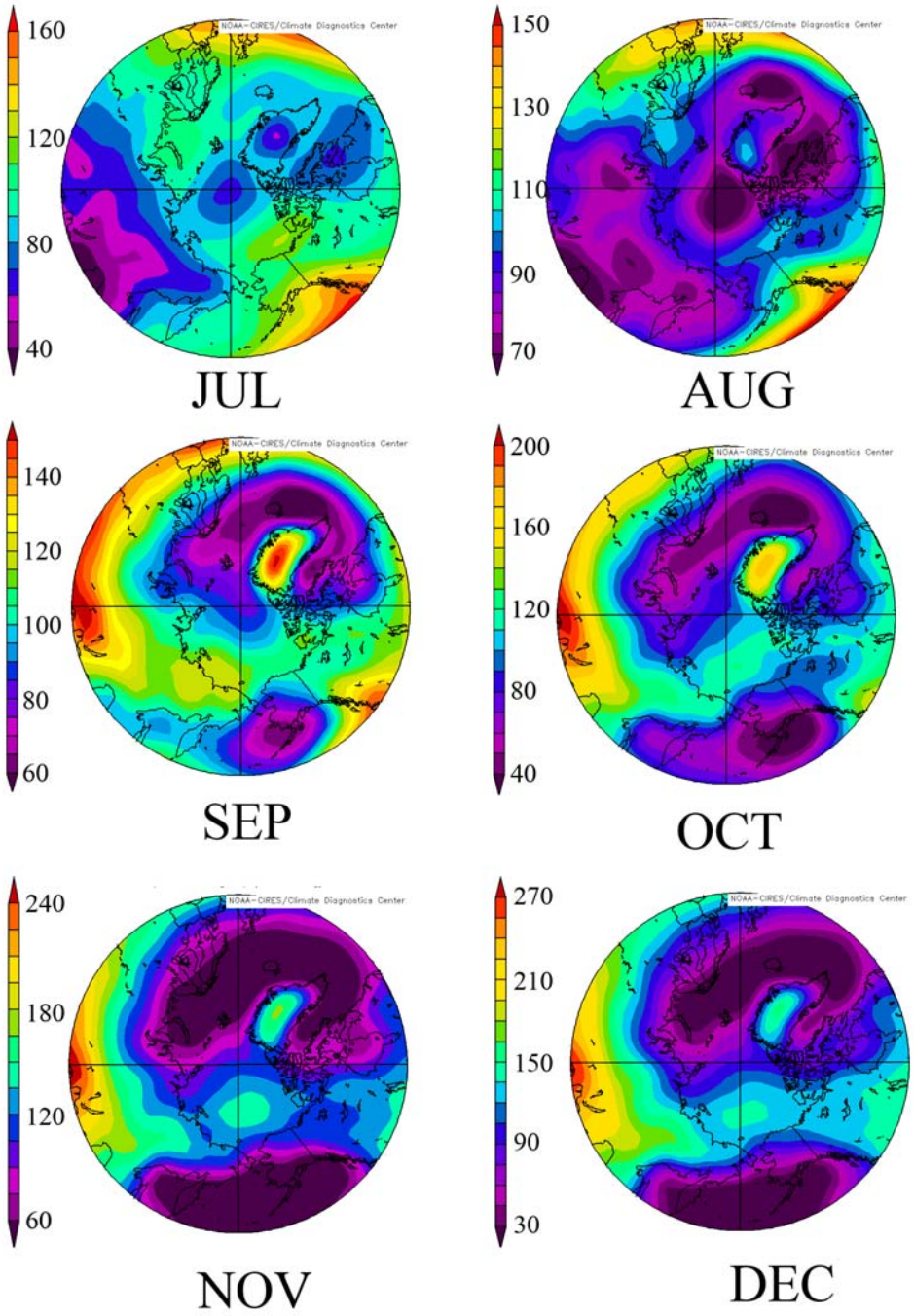

Figure A.2: NCEP/NCAR reanalysis of the 1000mb geopotential height climatology (1968-1996) from July - December.

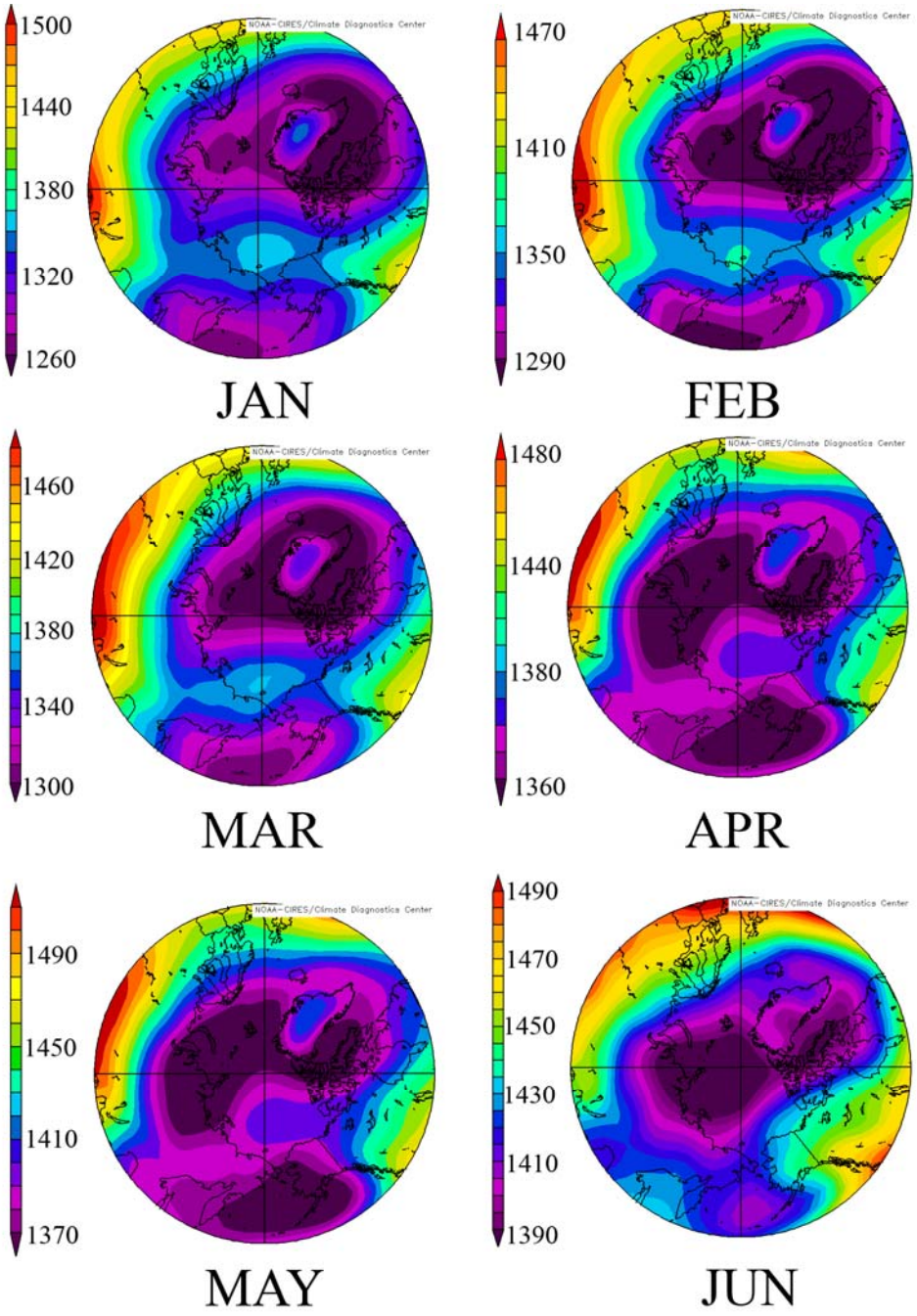

Figure A.3: NCEP/NCAR reanalysis of the 850 mb geopotential height climatology (1968-1996) from January - June.

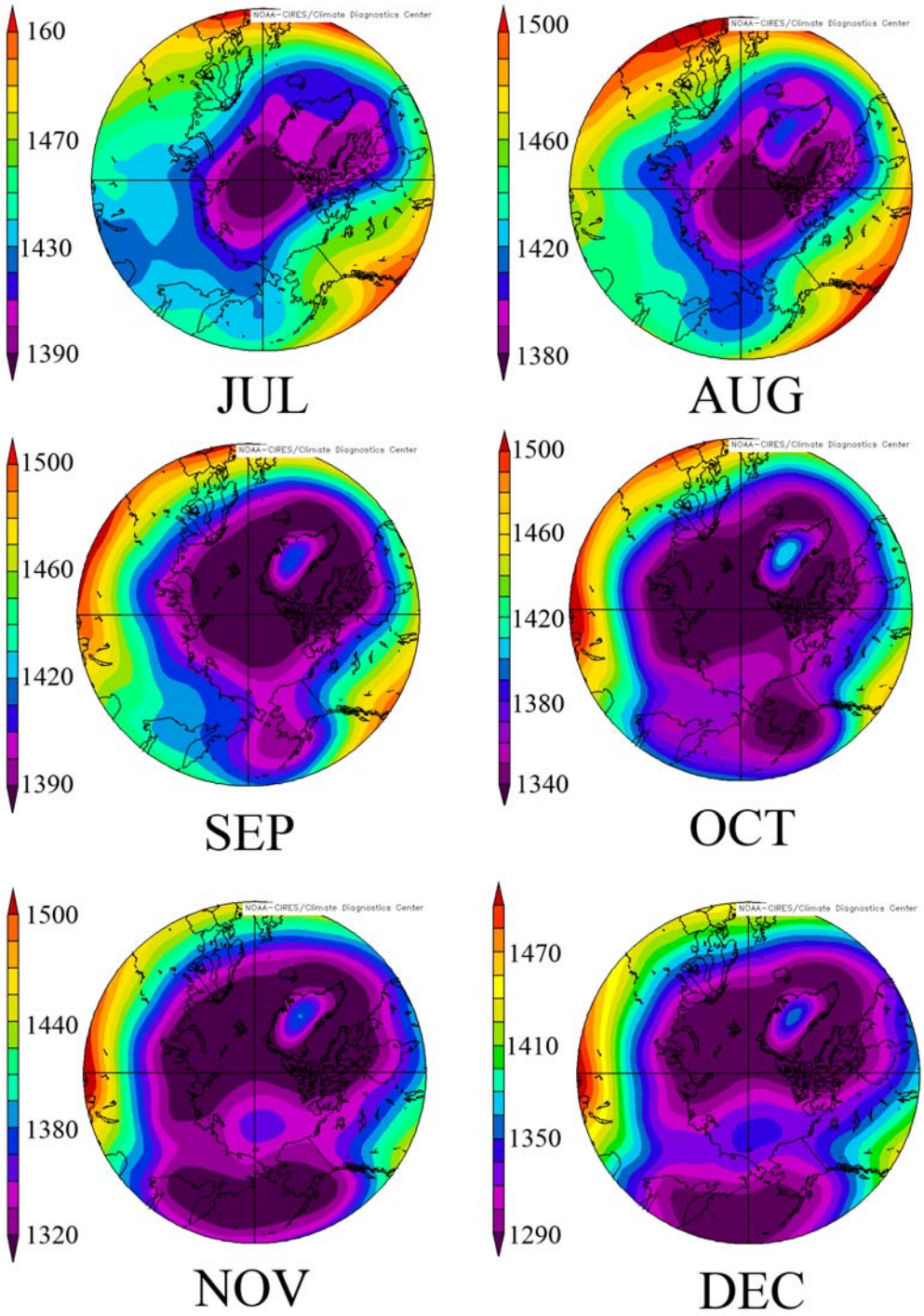

Figure A.4: NCEP/NCAR reanalysis of 850 mb geopotential height climatology (1968-1996) from July - December

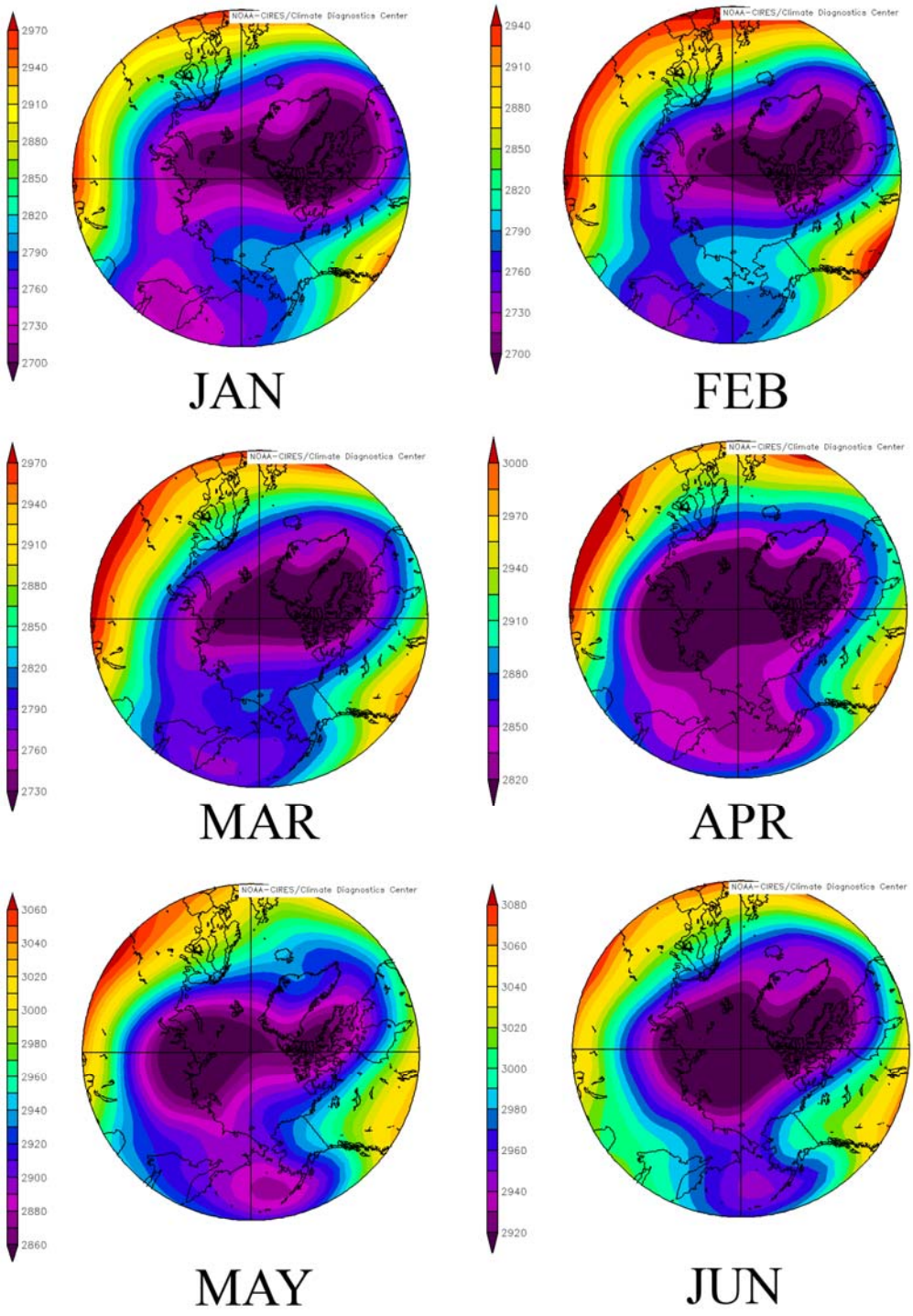

Figure A.5: NCEP/NCAR reanalysis of the 700mb geopotential height climatology (1968-1996) from January – June.

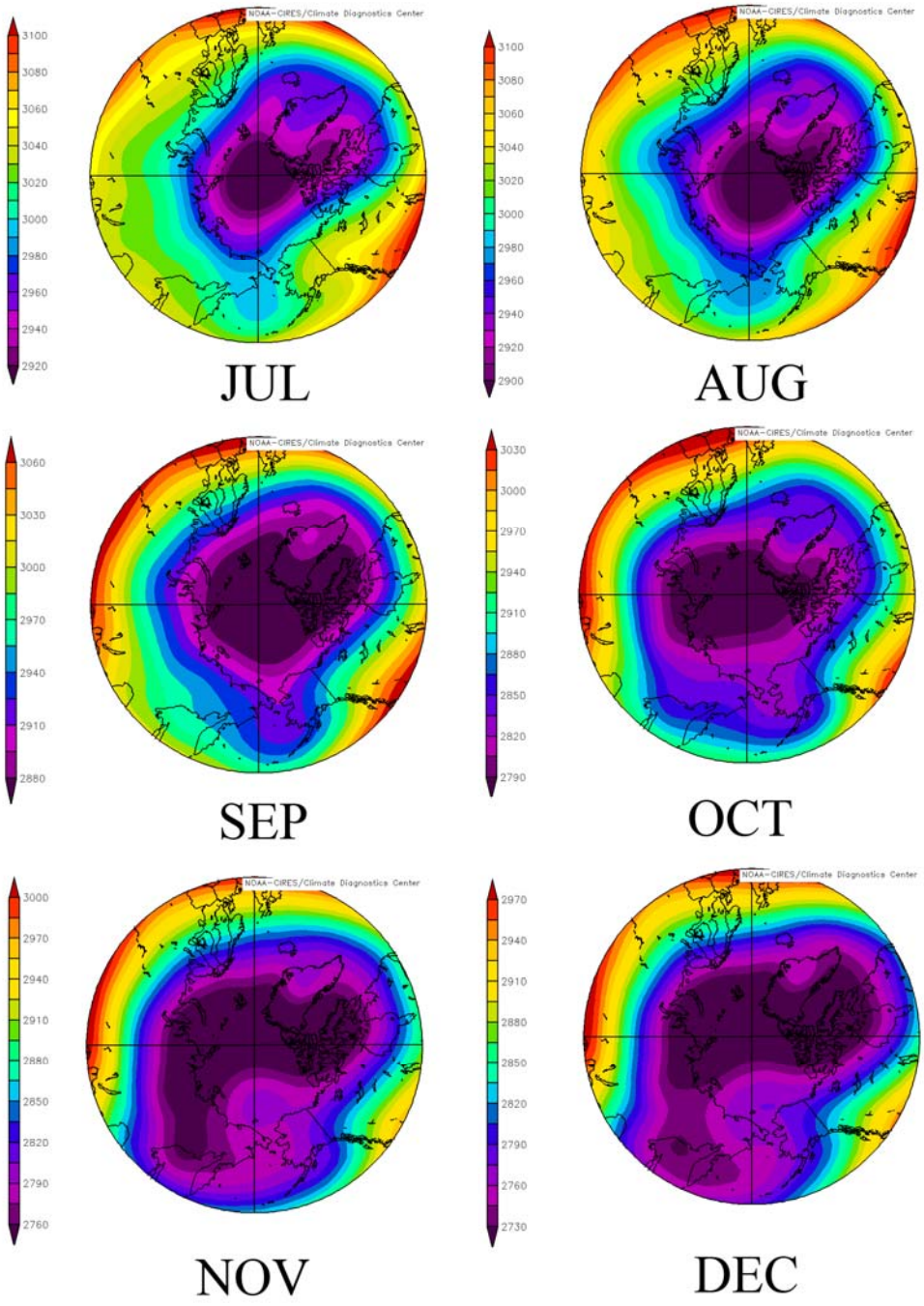

Figure A.6: NCEP/NCAR reanalysis of the 700mb geopotential height climatology (1968-1996) from July – December.

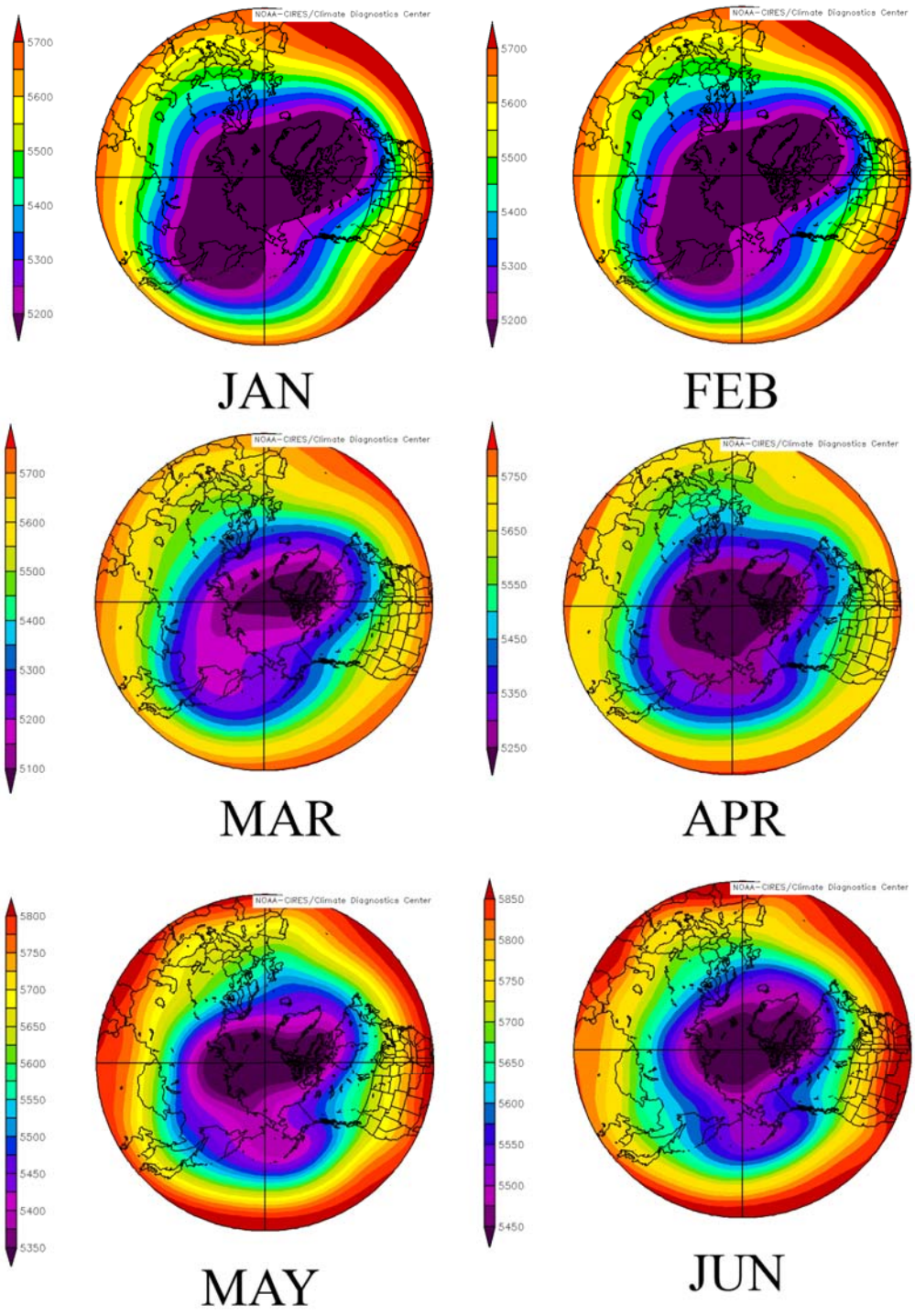

Figure A.7: NCEP/NCAR reanalysis of the 500mb geopotential height climatology (1968-1996) from January - June.

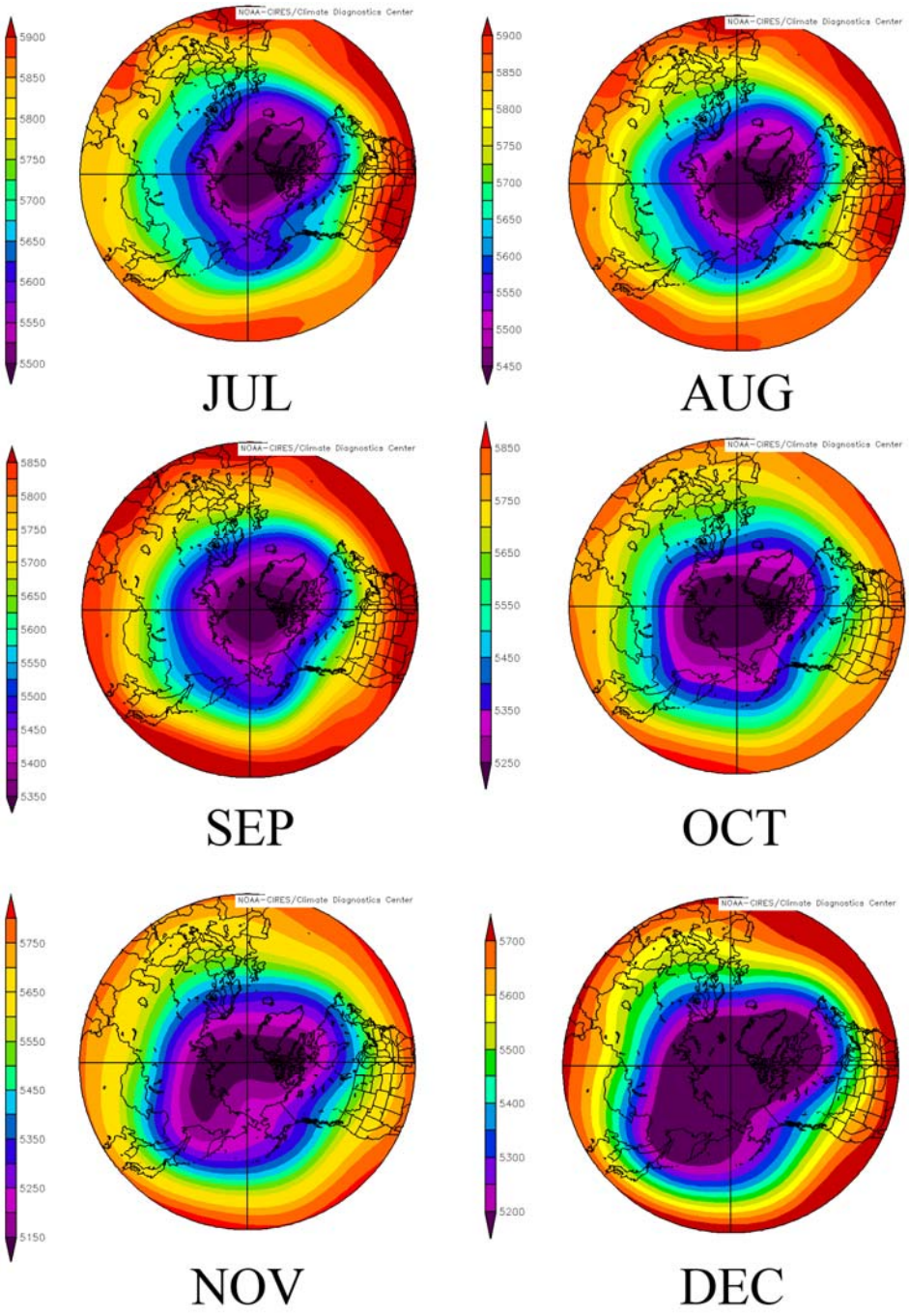

Figure A.7: NCEP/NCAR reanalysis of the 500mb geopotential height climatology (1968-1996) from July - December.

APPENDIX B: Three Year Mean NCEP/ NCAR Reanalysis Plots

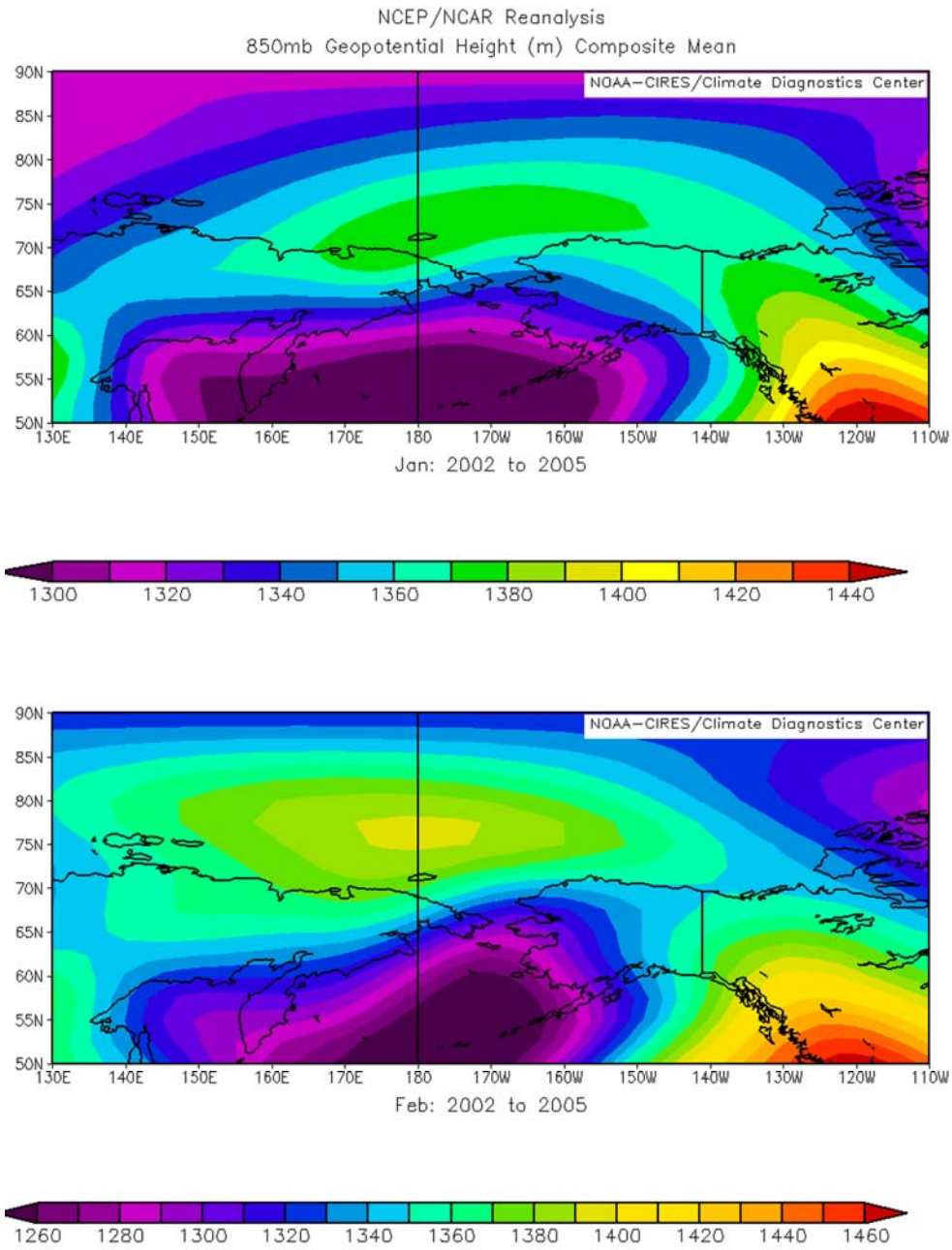

Figure B.1: NCEP/NCAR reanalysis of the three year (2002-2005) composite mean of the 850mb geopotential height for January and February.

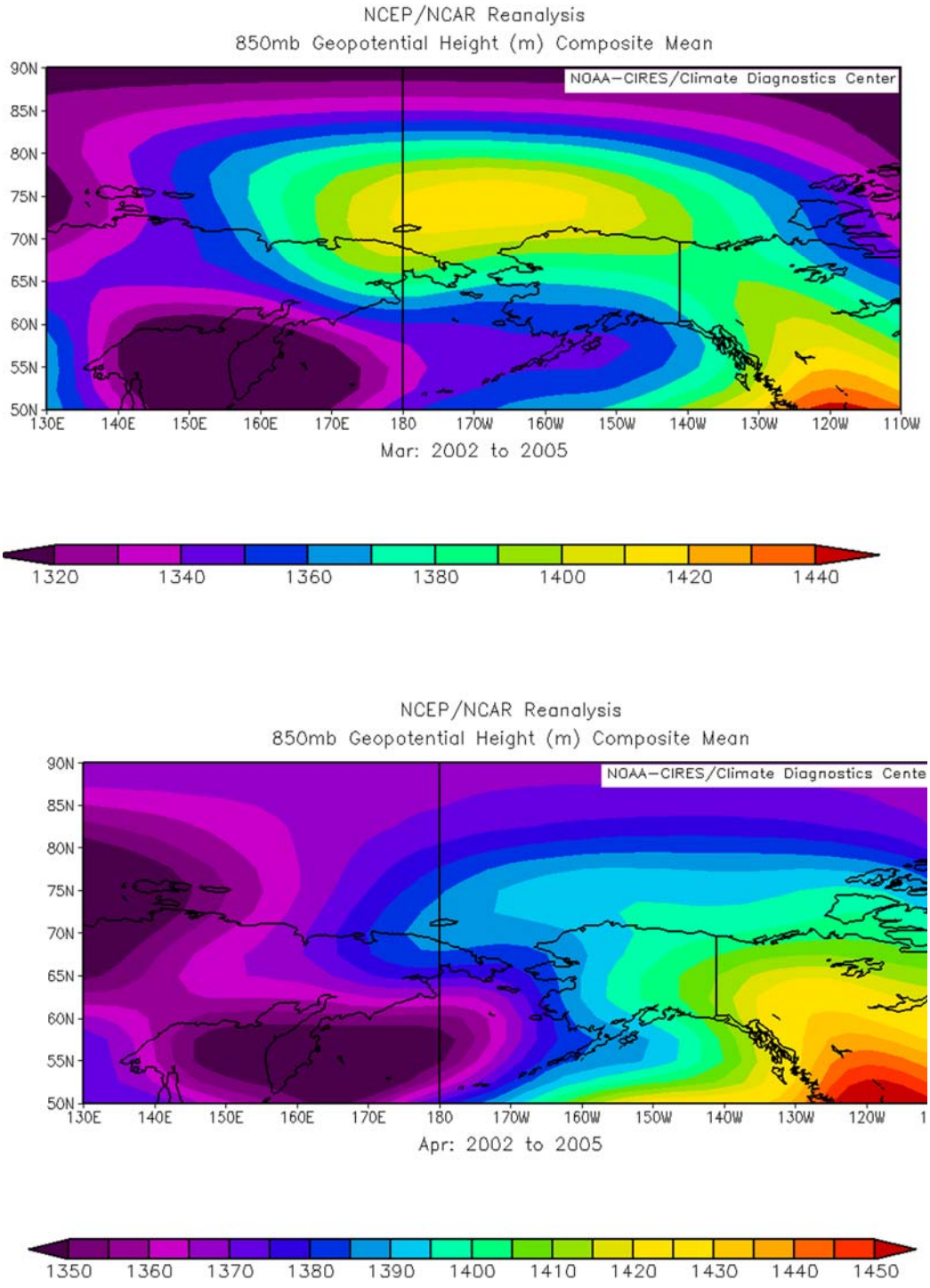

Figure B.2: NCEP/NCAR reanalysis of the three year (2002-2005) composite mean of the 850mb geopotential height for March and April.

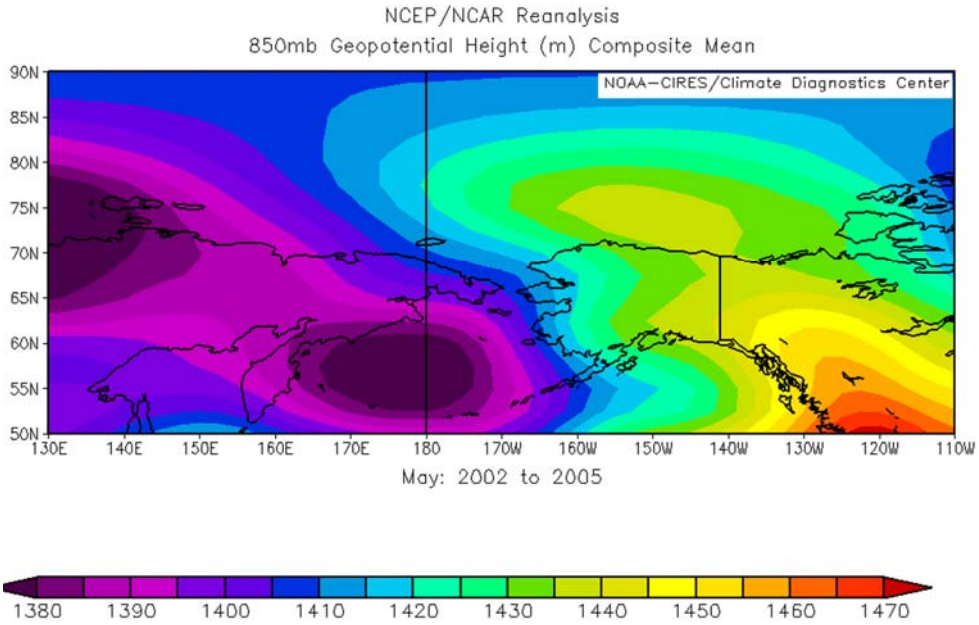

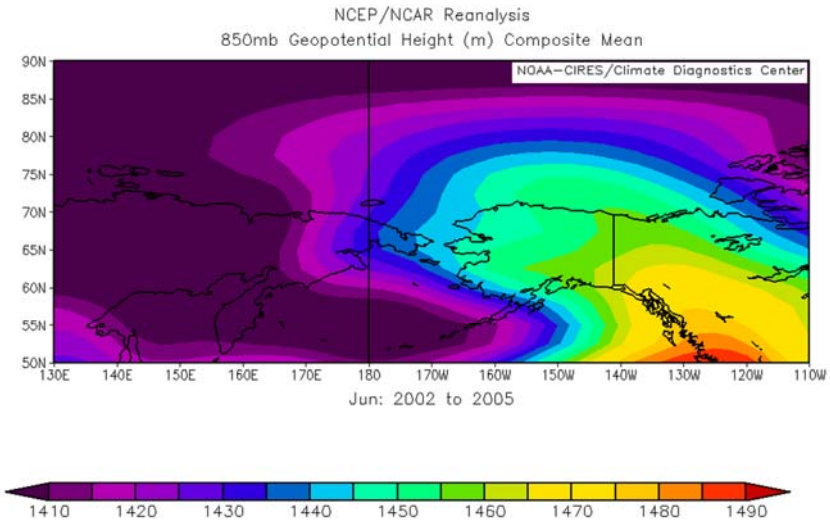

Fig B.3: NCEP/NCAR reanalysis of the three year (2002-2005) composite mean of the 850mb geopotential height for May and June.

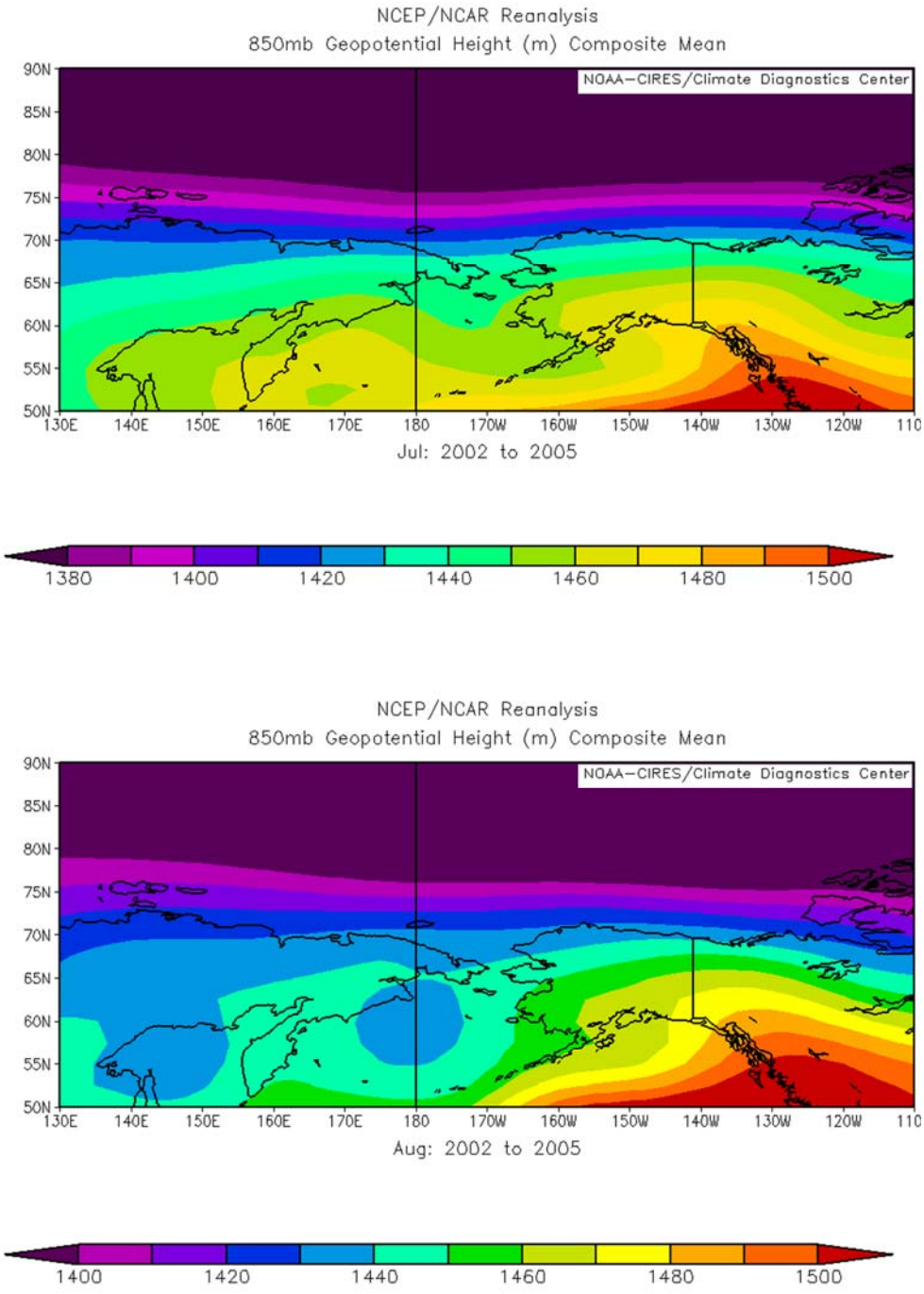

Figure B.4: NCEP/NCAR reanalysis of the three year (2002-2005) composite mean of the 850mb geopotential height for July and August.

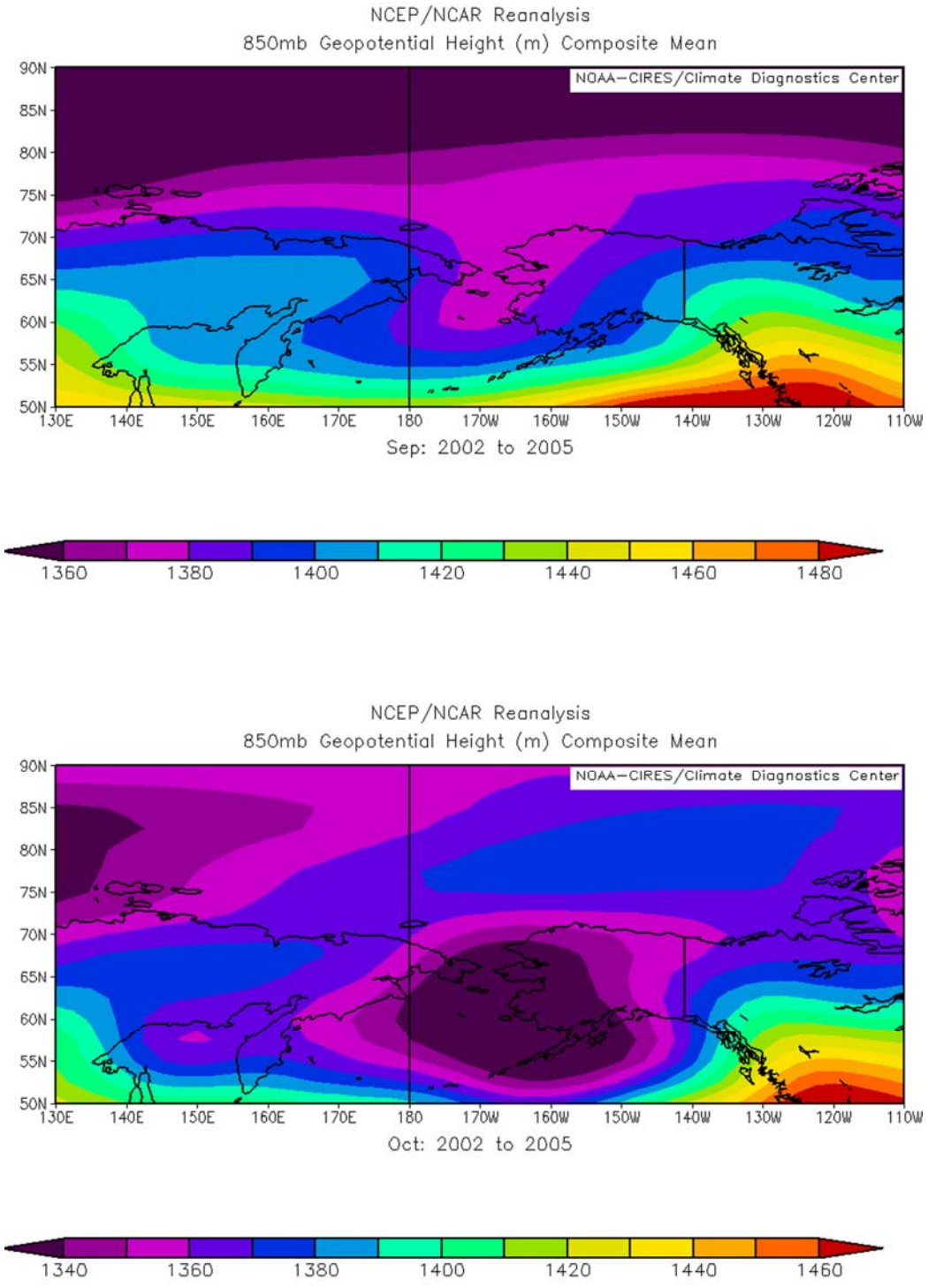

Figure B.5: NCEP/NCAR reanalysis of the three year (2002-2005) composite mean of the 850mb geopotential height for September and October.

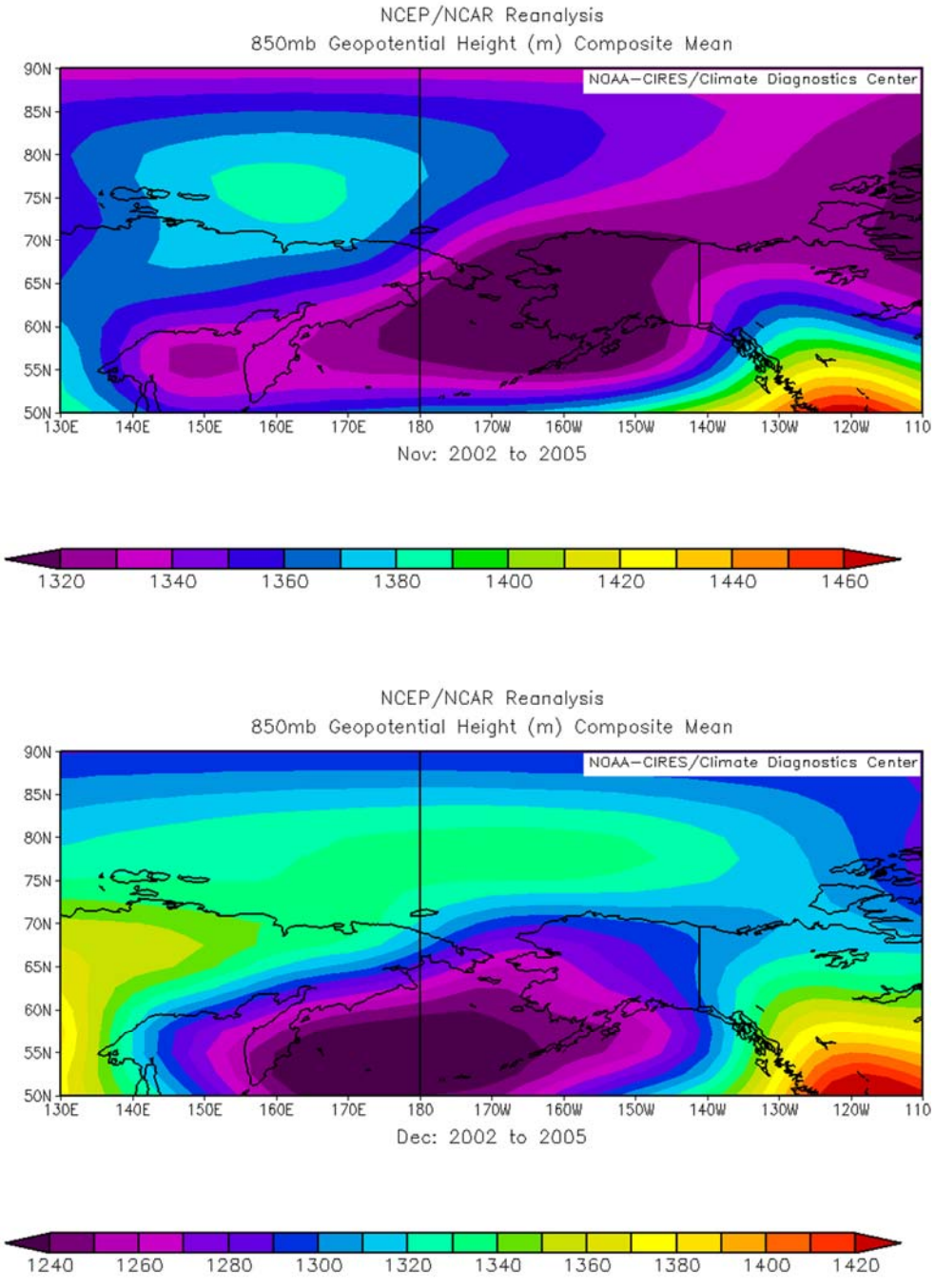

Figure B.6: NCEP/NCAR reanalysis of the three year (2002-2005) composite mean of the 850mb geopotential height for November and December.

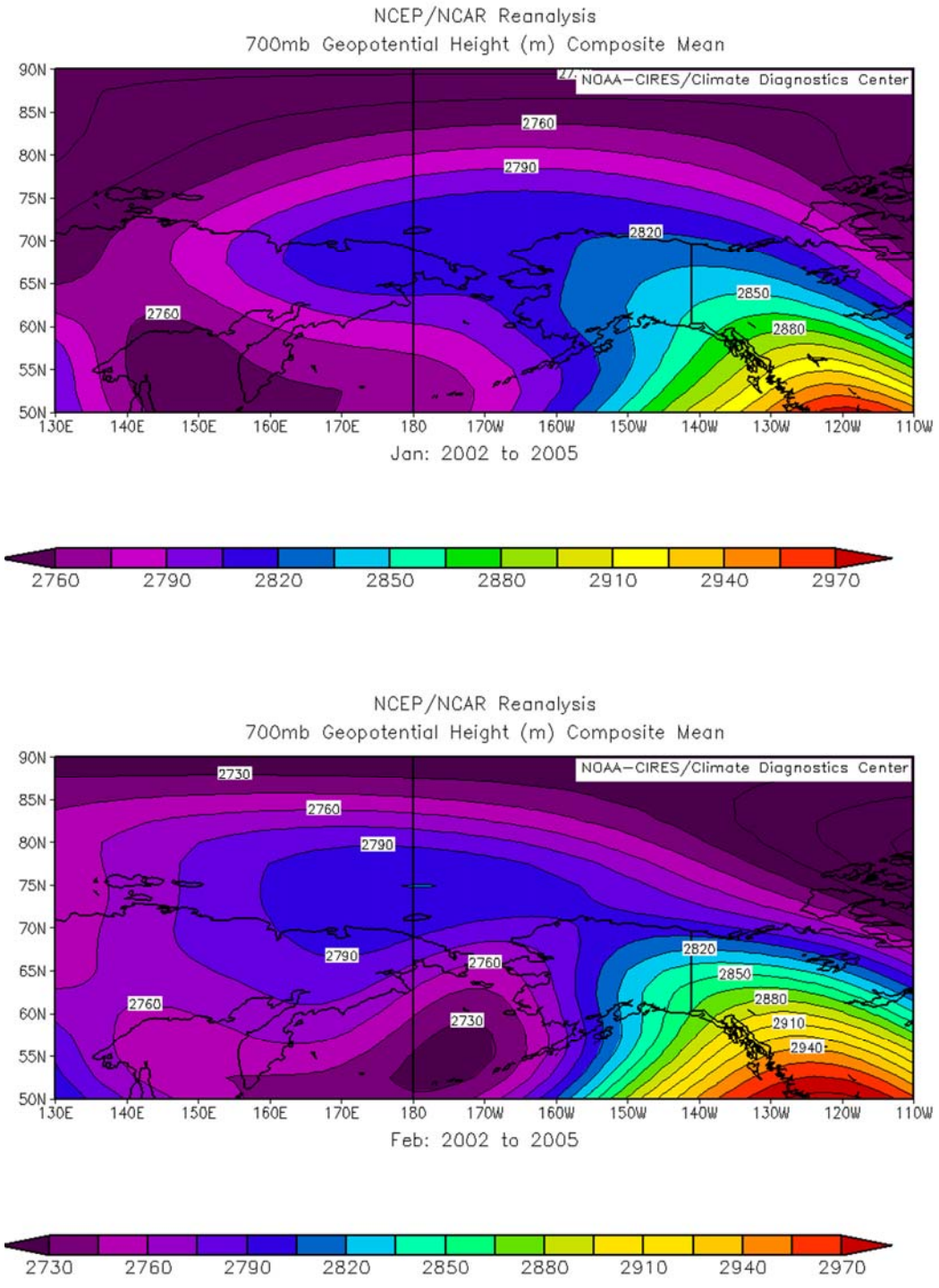

Figure B.7: NCEP/NCAR reanalysis of the three year (2002-2005) composite mean of the 700mb geopotential height from January and February.

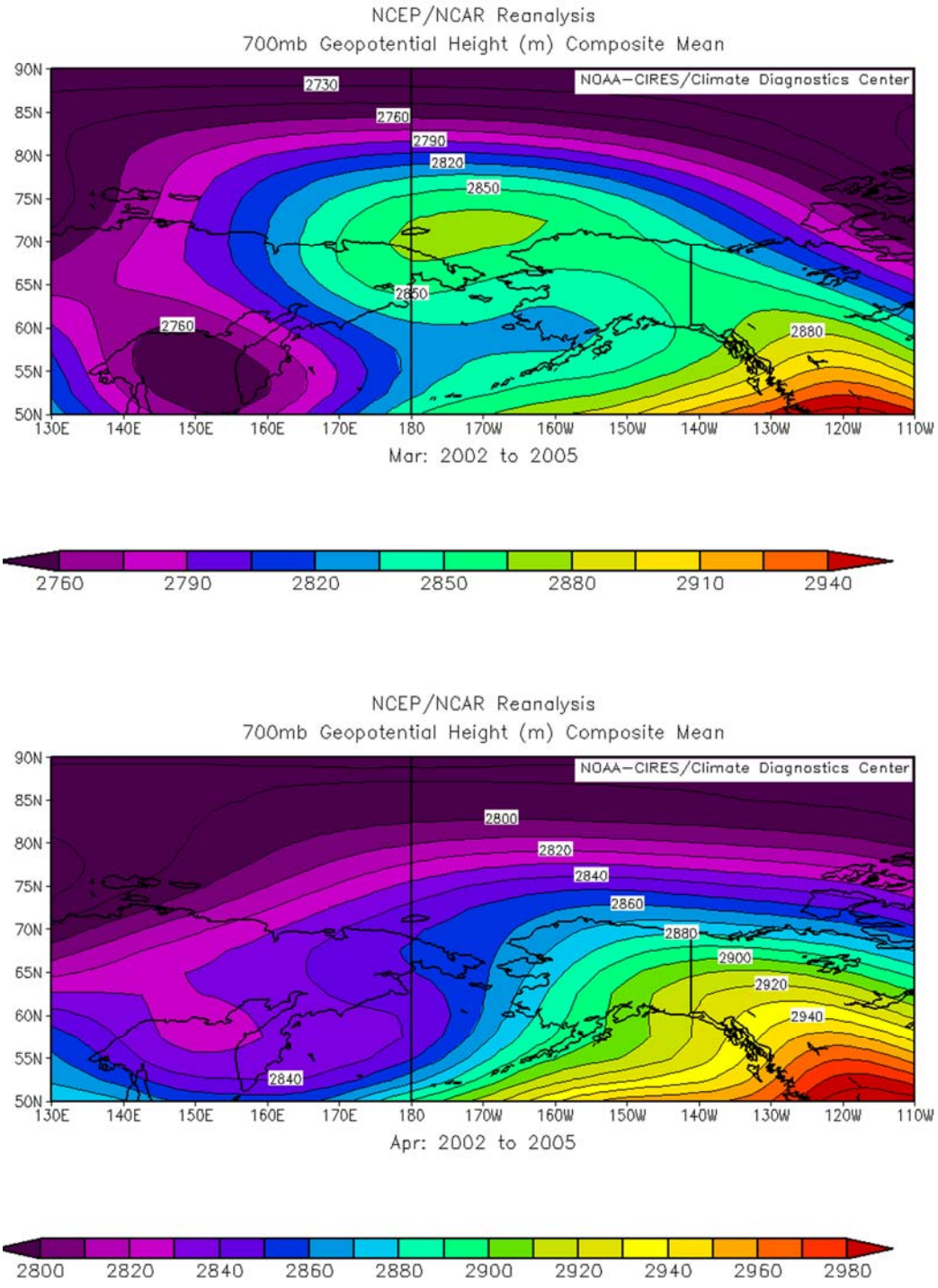

Figure B.8: NCEP/NCAR reanalysis of the three year (2002-2005) composite mean of the 700mb geopotential height from March and April.

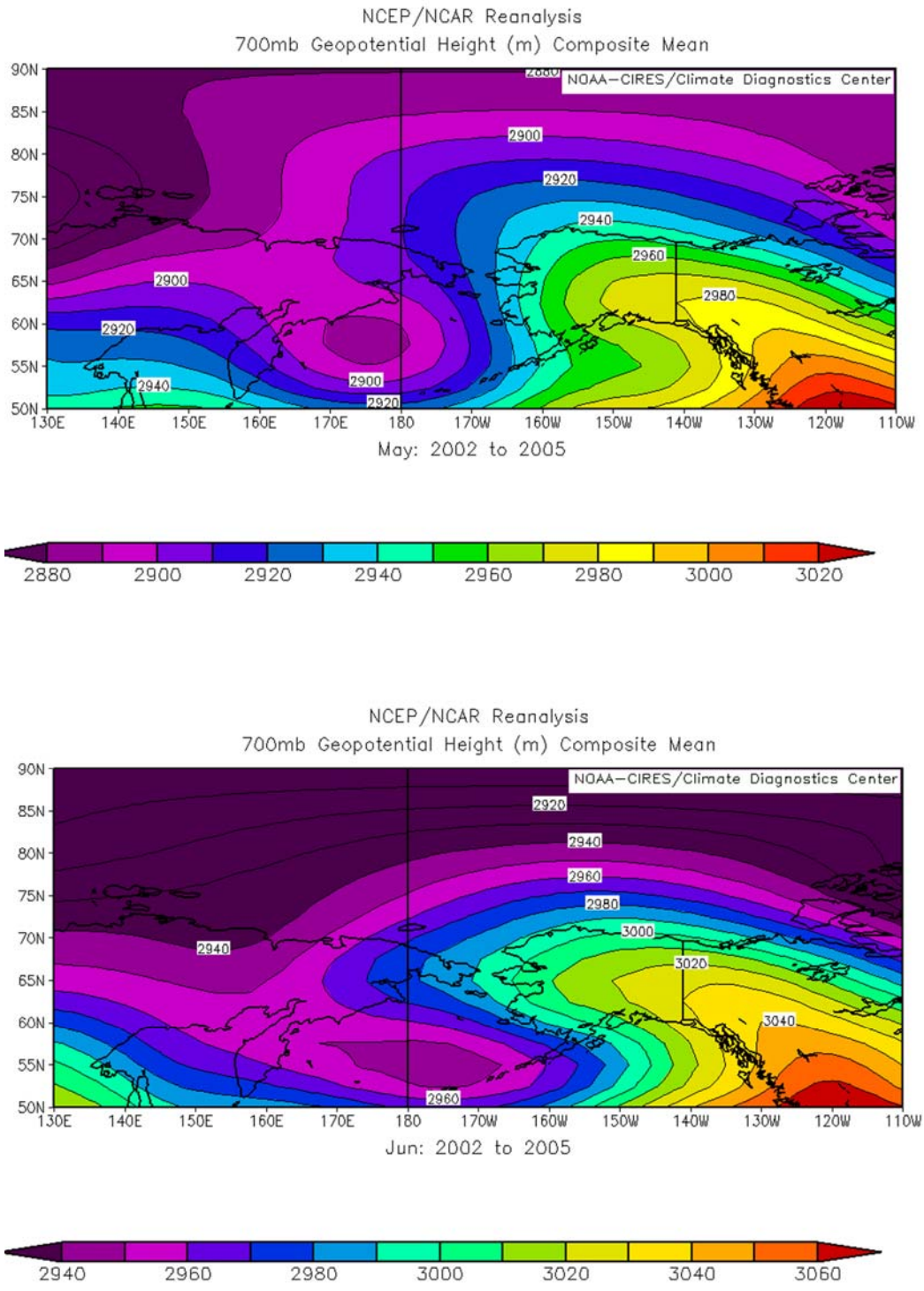

Figure B.9: NCEP/NCAR reanalysis of the three year (2002-2005) composite mean of the 700mb geopotential height from May and June.

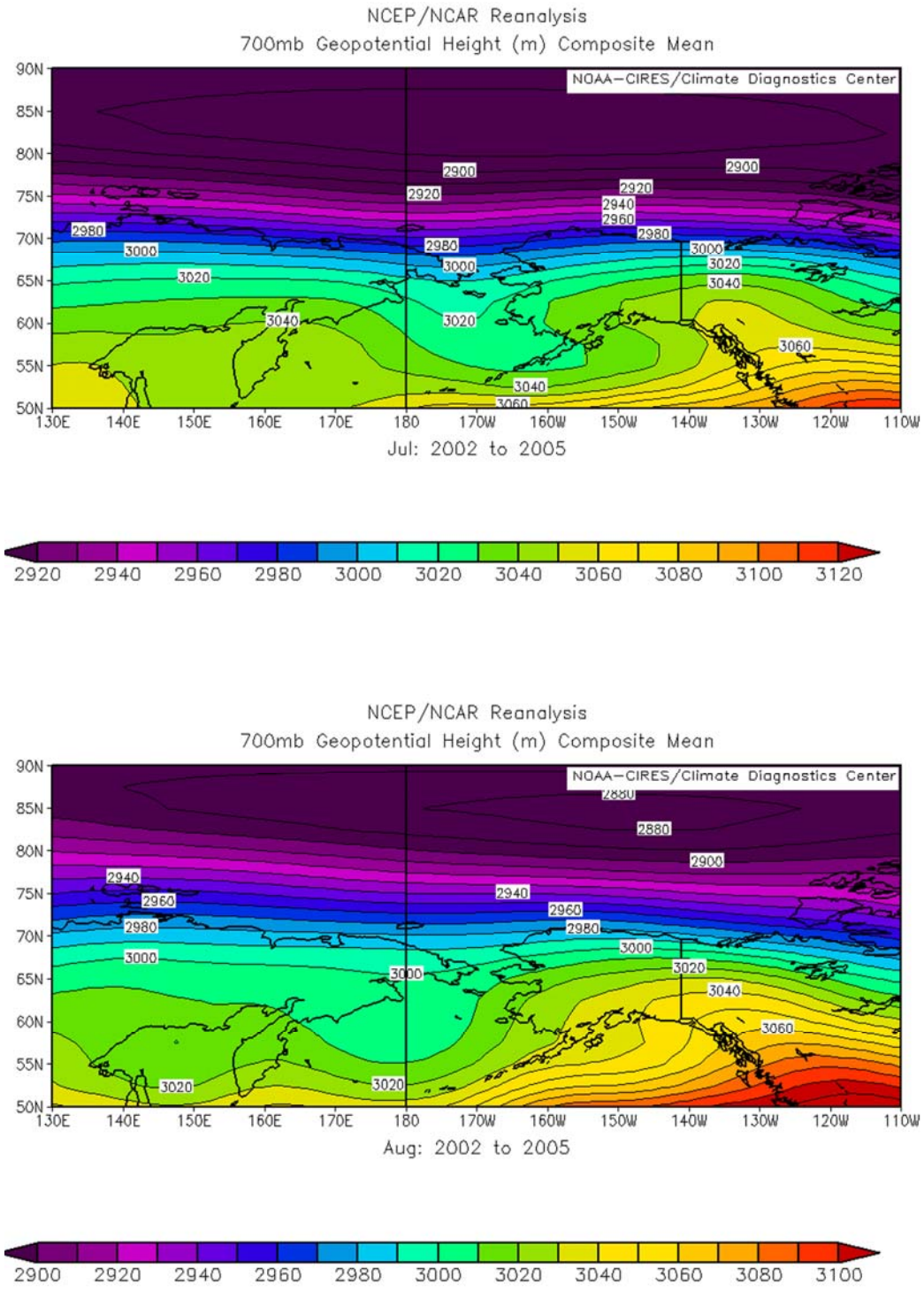

Figure B.10: NCEP/NCAR reanalysis of the three year (2002-2005) composite mean of the 700mb geopotential height from July and August.

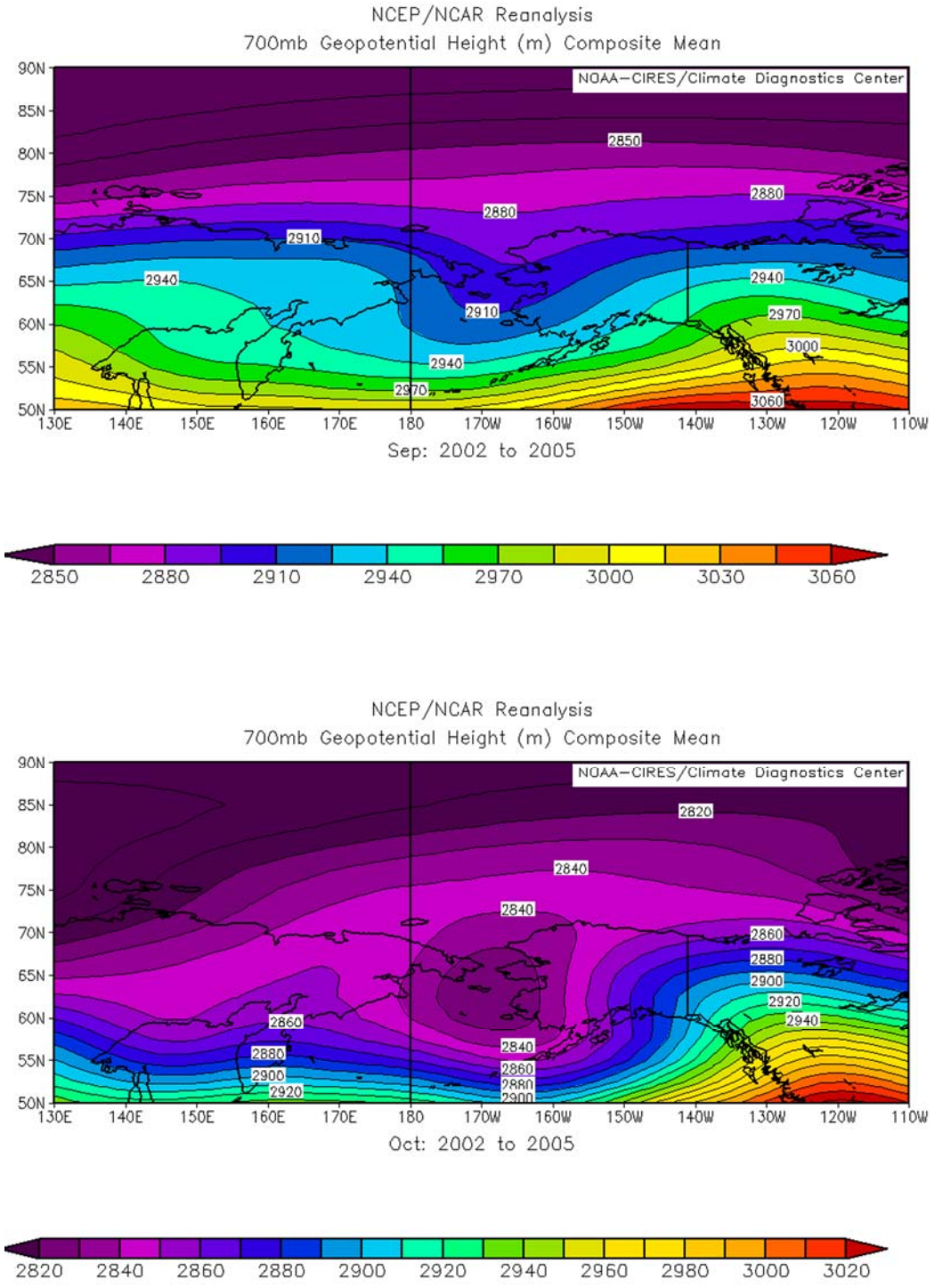

Figure B.11: NCEP/NCAR reanalysis of the three year (2002-2005) composite mean of the 700mb geopotential height from September and October.

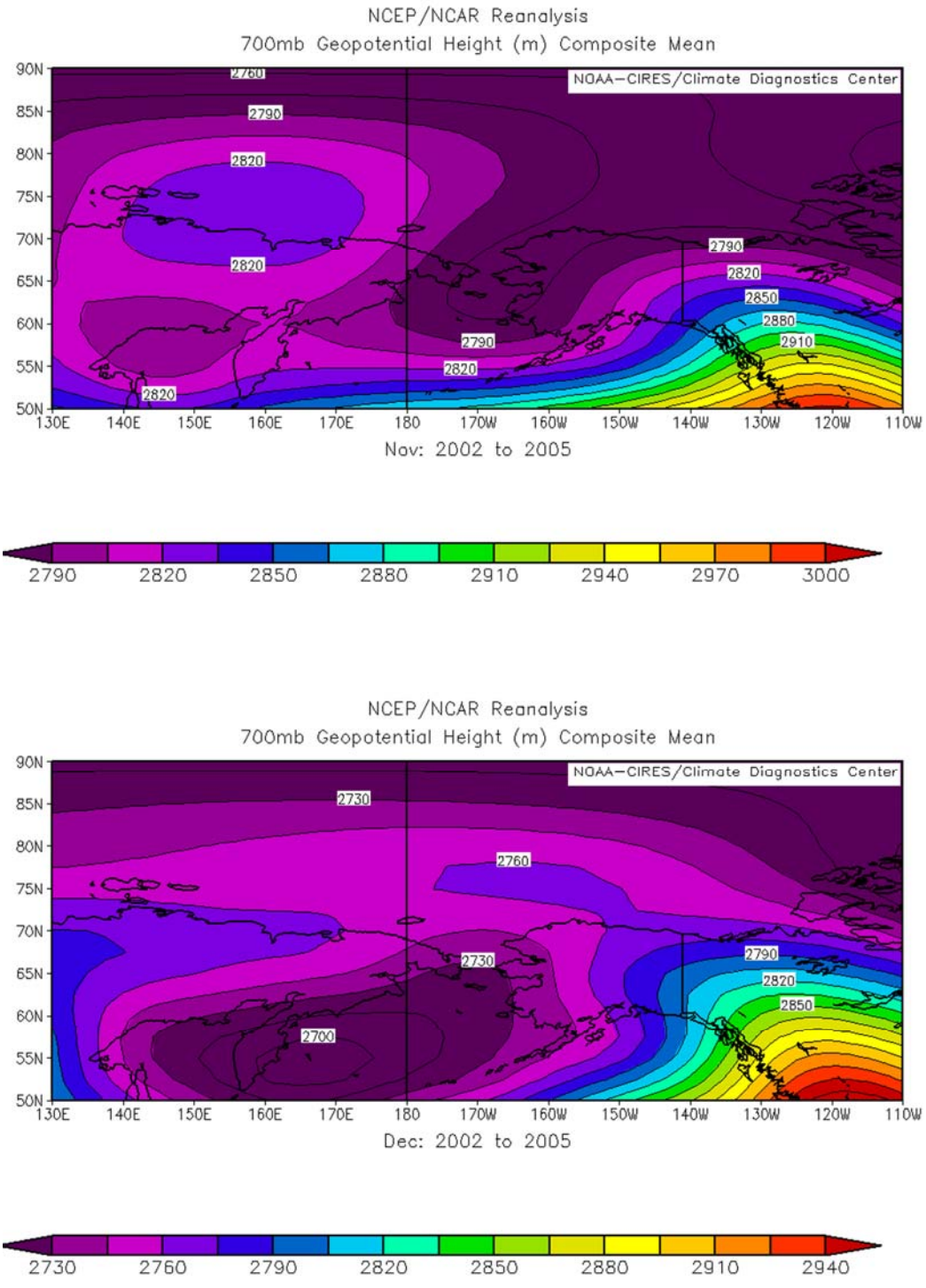

Figure B.12: NCEP/NCAR reanalysis of the three year (2002-2005) composite mean of the 700mb geopotential height from November and December.

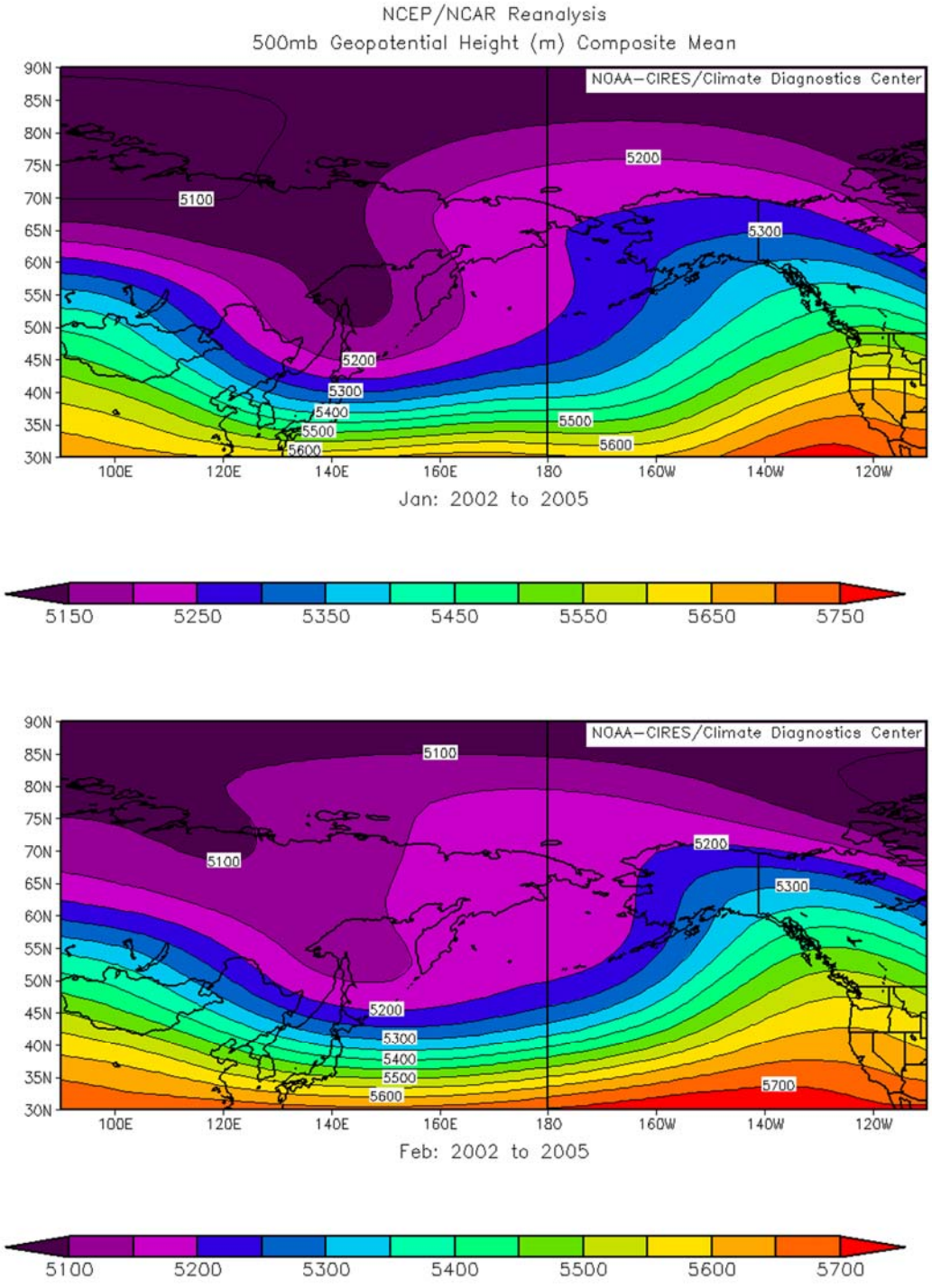

Figure B.13: NCEP/NCAR reanalysis of the three year (2002-2005) composite mean of the 500mb geopotential height from January and February.

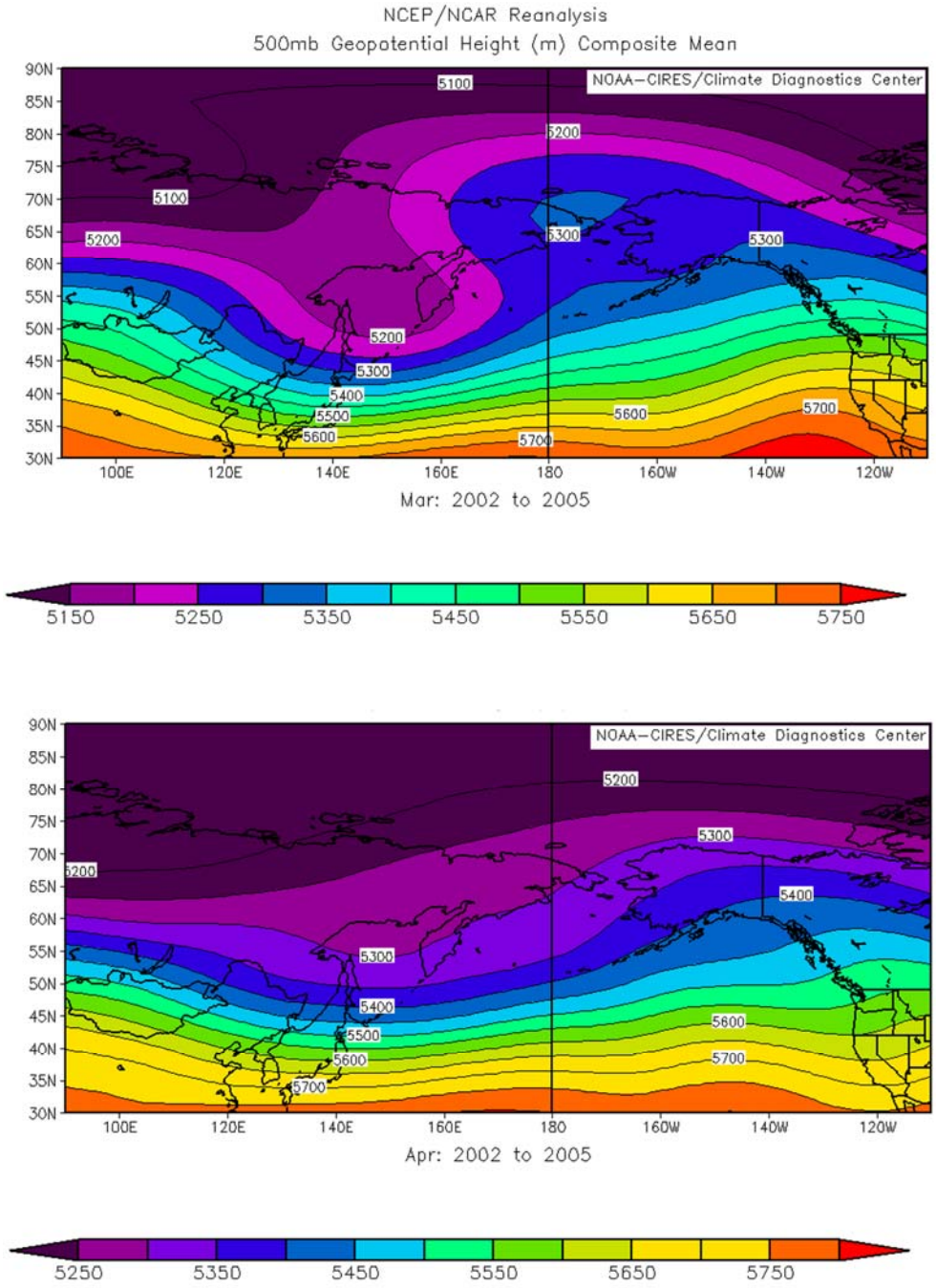

Figure B.14: NCEP/NCAR reanalysis of the three year (2002-2005) composite mean of the 500mb geopotential height from March and April.

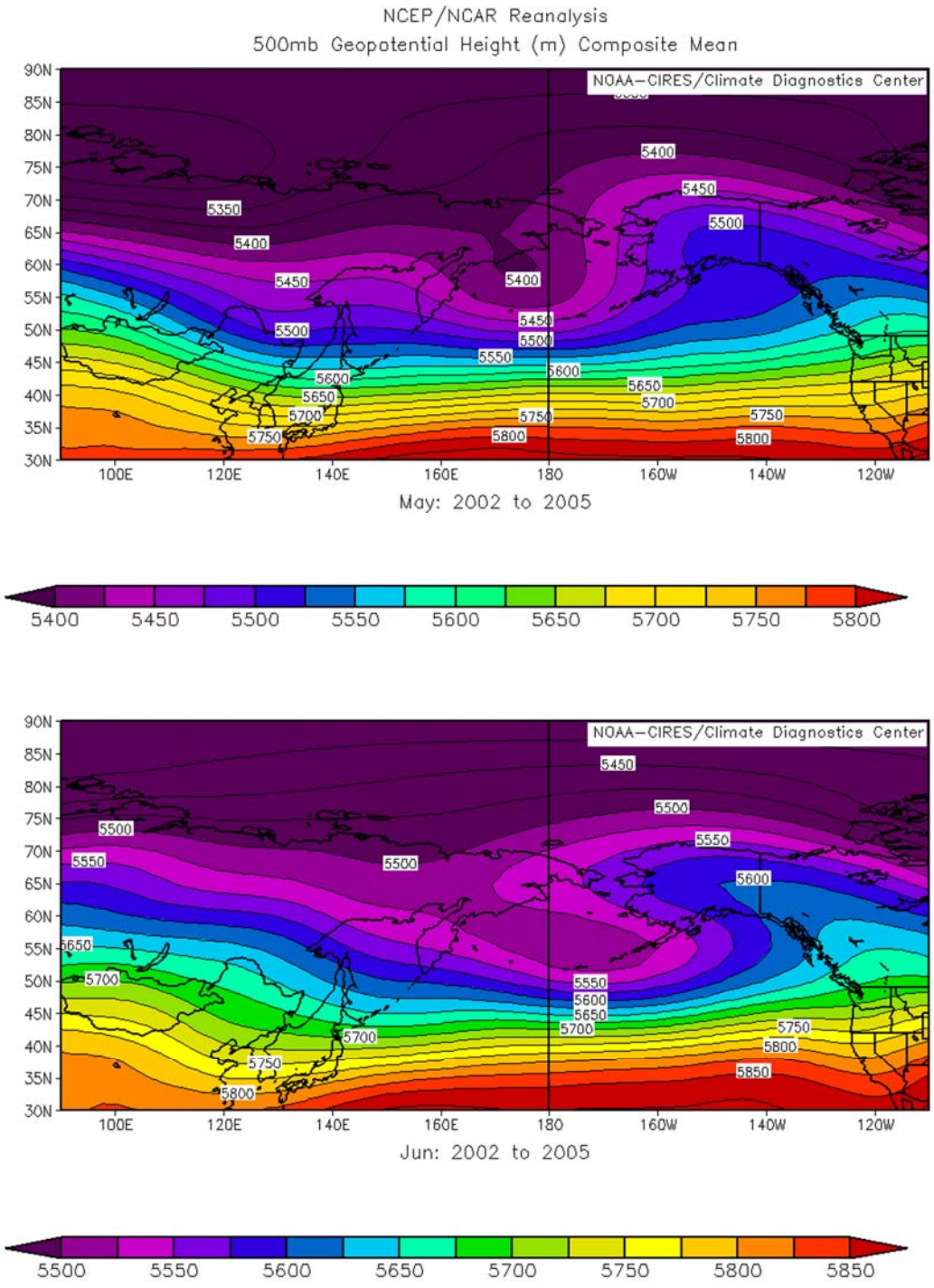

Figure B.15: NCEP/NCAR reanalysis of the three year (2002-2005) composite mean of the 500mb geopotential height from May and June.

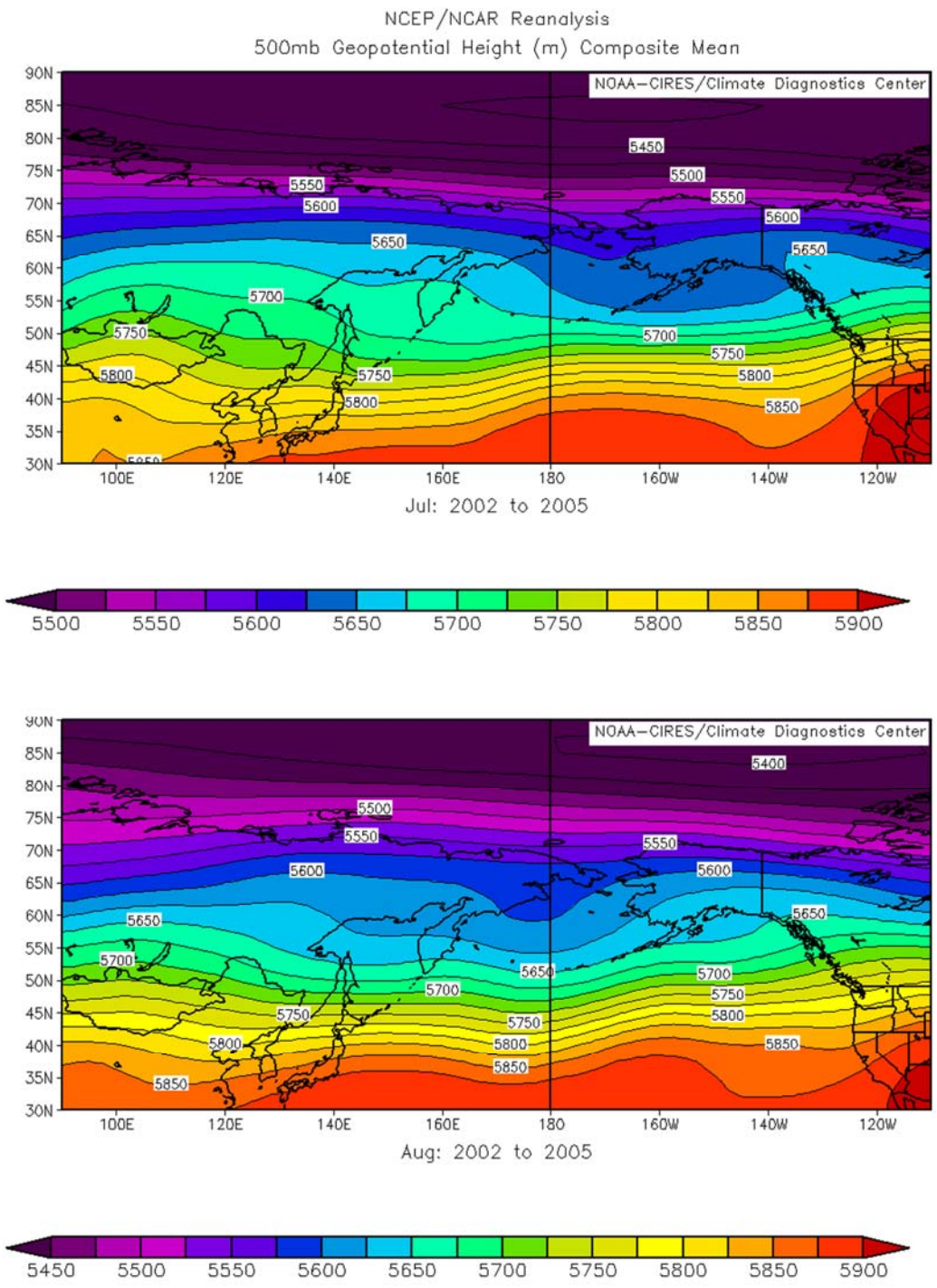

Figure B.16: NCEP/NCAR reanalysis of the three year (2002-2005) composite mean of the 500mb geopotential height from July and August.

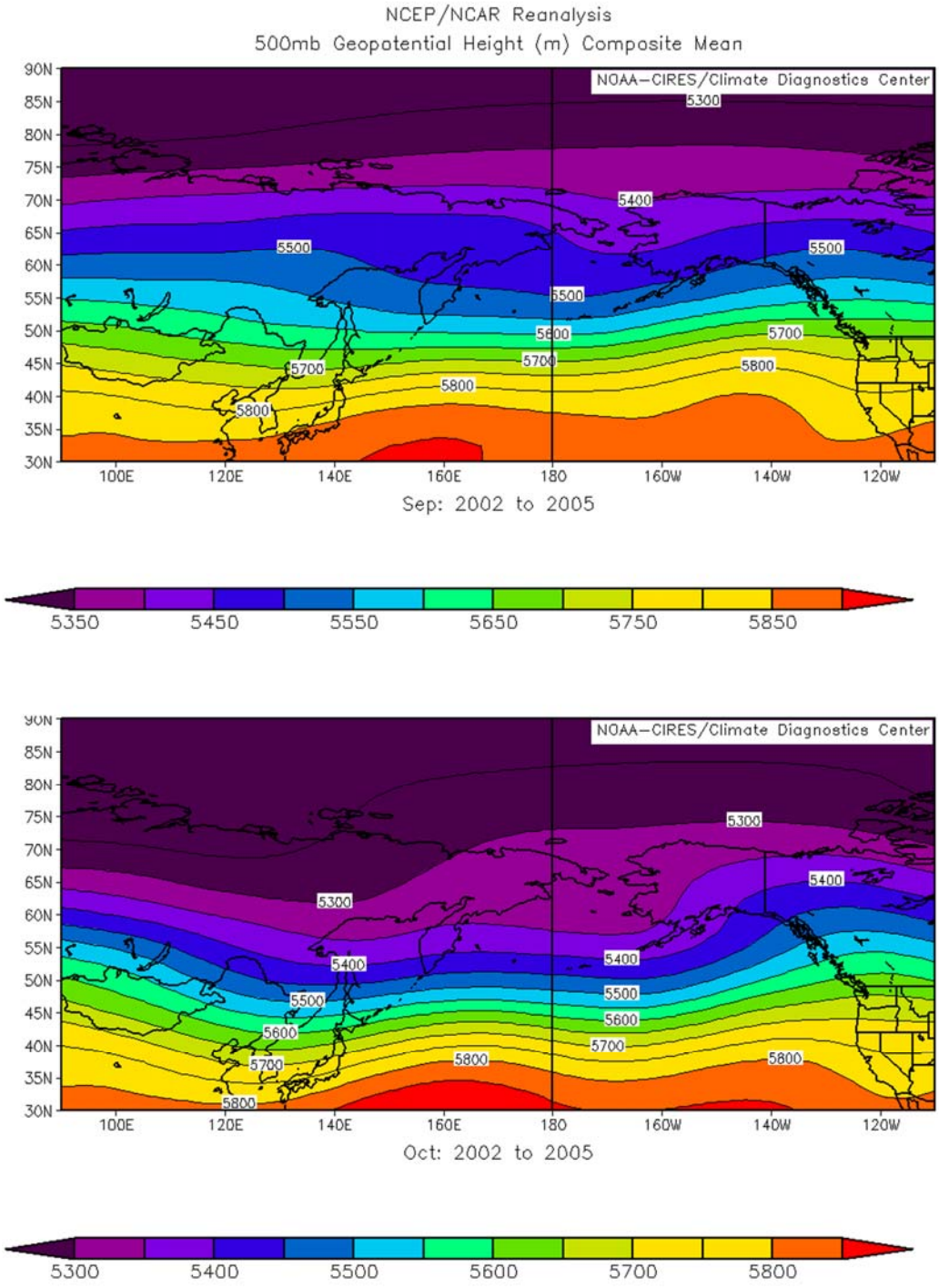

Figure B.17: NCEP/NCAR reanalysis of the three year (2002-2005) composite mean of the 500mb geopotential height from September and October.

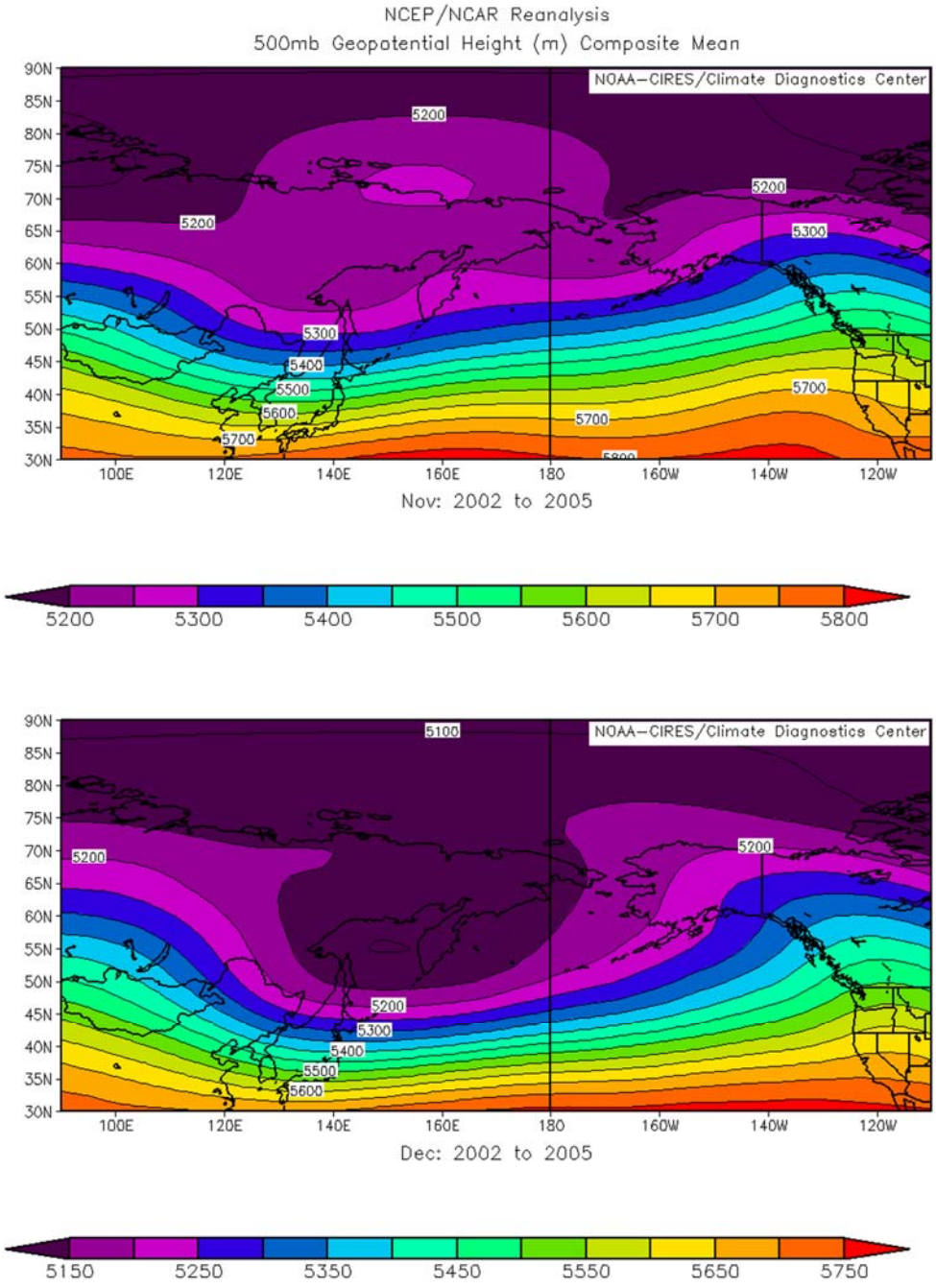

Figure B.18: NCEP/NCAR reanalysis of the three year (2002-2005) composite mean of the 500mb geopotential height from May and June.

References

Barrie, L. A., R.M. Hoff, and S.M. Daggupaty 1981: The influence of mid-latitudinal pollution sources on the haze in the Canadian Arctic. *Atmospheric Environment*, **15,** 1407-1419.

Barry, R. G. and A. M. Carleton, 2001: *Synoptic and Dynamic Climatology*. First Edition ed. Routledge Publications.

Behrendt, A. and T. Nakamura, 2002: Calculation of the calibration constant of polarization lidar and its dependency on atmospheric temperature. *Optics Express*, **10,** 805-817.

Bohren, C. F. and S. B. Singham, 1991: Backscattering by nonspherical particles - A review of methods and suggested new approaches. *Journal Of Geophysical Research-Atmospheres*, **96,** 5269-5277.

Bohren, C. F. and B. A. Albrecht, 1998: *Atmospheric Thermodynamics*. Oxford University Press.

Bond, N. A. and M. A. Shapiro, 1991: Polar lows over the Gulf of Alaska in conditions of reverse shear. *Monthly Weather Review*, **119,** 551-572.

Campbell, J. R., D. L. Hlavka, E. J. Welton, C. J. Flynn, D. D. Turner, J. D. Spinhirne, V. S. Scott, III, and I. H. Hwang, 2002: Full-time, eye-safe cloud and aerosol lidar observation at atmospheric radiation measurement program sites: Instruments and data processing. *Journal of Atmospheric and Oceanic Technology*, **19,** 431-442.

Campbell, J. R., E. J. Welton, J. D. Spinhirne, Q. Ji, S. C. Tsay, S. J. Piketh, M. Barenbrug, and B. N. Holben, 2003: Micropulse lidar observations of

tropospheric aerosols over northeastern South Africa during the ARREX and SAFARI 2000 dry season experiments. *Journal of Geophysical Research-Atmospheres*, **108**.

Chaston, P. R., 2002: *Weather Maps - How to Read and Interpret All the Basic Weather Charts*. Third ed. Chaston Scientific.

Connor, F., K. Sassen, and J. R. Campbell, 2005: Personal Communications.

Djuric, D., 1994: *Weather Analysis*. Prentice-Hall.

Draxler, R.R. and G.D. Hess, 1998: An Overview of the Hysplit_4 Modeling System for Trajectories, Dispersion, and Deposition, *Australian Meteorological Magazine*, **47**, 295-308.

Gerrard, A. J., T. J. Kane, J. P. Thayer, T. J. Duck, J. A. Whiteway, and J. Fiedler, 2002: Synoptic scale study of the Arctic polar vortex's influence on the middle atmosphere, 1, Observations. *Journal of Geophysical Research-Atmospheres*, **107**.

Hartmann, B. and G. Wendler, *2003*: Manifestation of the Pacific Decadal Oscillation shift of 1976 in Alaskan climatology. *Proceedings of the AMS Seventh Conference on Polar Meteorology and Oceanography and Joint Symposium on High-Latitude Climate Variations*, Hyannis, MA, American Meteorological Society.

Heidam, N. Z., 1984: The components of the Arctic Aerosol. *Atmospheric Environment*, **18,** 329-343.

——, 1985: Crustal enrichments in the Arctic Aerosol. *Atmospheric Environment*, **19,** 2083-97.

Heintzenberg and others, 1981: The chemical composition of Arctic haze at Ny-Iesund, Spitsbergen. *Tellus*, **33,** 162-71.

Heintzenberg, J., 1980: Particle size distribution and optical properties of Arctic Haze. *Tellus*, **32,** 251-60.

Heintzenberg, J. and S. Larssen, 1983: SO2 and SO4- in the Arctic: interpretations of the observations at three Norweigian Arctic-Subarctic statios. *Tellus*, **35B,** 255-265.

Hobbs, P. V., 1993: *Aerosol-Cloud-Climate Interactions*. *International Geophysics Series*, Academic Press.

Holton, J. R., 2004: *An Introduction to Dynamic Meteorology*. Fourth Edition ed. Academic Press.

Houghton, J., Ding, Y., Griggs, D., Noguer, M., van der Linden, P., Dai, X., Maskell, K., Johnson, C. (Eds.), 2001. IPCC 2001, Climate Change 2001: The scientific basis. contribution of working group i to the third assessment report of the intergovernmental panel on climate change. Cambridge University Press, Cambridge.

Hu, R. M., J. P. Blanchet, and E. Girard, 2005: Evaluation of the direct and indirect radiative and climate effects of aerosols over the western Arctic. *Journal of Geophysical Research-Atmospheres*, **110**.

Jennings, S. G., 1993: *Aerosol Effects on Climate*. University of Arizona Press.

Liou, K. N., 2002: *An Introduction to Atmospheric Radiation*. Second Edition ed. Academic Press.

Katsoulis, B. D., 1999: The potential for long-range transport of air-pollutants into Greece: a climatological analysis. *Science of The Total Environment*, **231,** 101-113.

Khvorostyanov, V. I. and K. Sassen, 1998: Cirrus cloud simulation using explicit microphysics and radiation. Part II: Microphysics, vapor and ice mass budgets, and optical and radiative properties. *Journal of The Atmospheric Sciences*, **55,** 1822-1845.

McKendry, I. G., J. P. Hacker, R. Stull, S. Sakiyama, D. Mignacca, and K. Reid, 2001: Long-range transport of Asian dust to the Lower Fraser Valley, British Columbia, Canada. *Journal Of Geophysical Research-Atmospheres*, **106,** 18361-18370.

Measures, R. M., 1992: *Laser Remote Sensing: Fundamentals and Applications*. Krieger Publishing Company.

Ottar and Pacyna, 1986: Origin and characteristics of aerosols in the Norwegian Arctic. *Arctic Air Pollution*, B. Stonehouse, Ed., 53-68.

Overland, J. E. and T. R. Hiester, 1980: Development of a synoptic climatology for the Northeast Gulf of Alaska. *Journal of Applied Meteorology*, **19,** 1-14.

Pruppacher, H. R. and J. D. Klett, 1996: *Microphysics of Clouds and Precipitation*. Springer.

Raatz, W. E. and G. E. Shaw, 1984: Long-range tropospheric transport of pollution aerosols into the Alaskan arctic. *Journal of Applied Meteorology*, **23,** 1052-1064.

Rahn, K. A., 1981a: Atmospheric riverine and oceanic sources of seven trace constituents to the Arctic ocean. *Atmospheric Environment*, **15,** 1507-16.

——, 1981b: The arctic air sampling network in 1980. *Atmospheric Environment*, **15,** 1349-52.

——, 1985: Progress in arctic air chemistry, 1980-1984. *Atmospheric Environment*, **19,** 1987-94.

Rinke, A., K. Dethloff, and M. Fortmann, 2004: Regional climate effects of Arctic Haze. *Geophysical Research Letters*, **31**.

Rogers, R. R. and M. K. Yau, 1996: *Short Course in Cloud Physics*. *Series in Natural Philosophy*, Butterworth-Heinemann.

Sassen, K., 1974: Depolarization of laser light backscattered by artificial clouds. *Journal of Applied Meteorology*, **13,** 923-933.

——, 1991: The polarization lidar technique for cloud research - a review and current assessment. *Bulletin of the American Meteorological Society*, **72,** 1848-1866.

——, 1992: Evidence for liquid-phase cirrus cloud formation from volcanic aerosols - climatic implications. *Science*, **257,** 516-519.

——, 1994: Advances in polarization diversity lidar for cloud remote-sensing. *Proceedings of the IEEE*, **82,** 1907-14.

Sassen, K. and G. C. Dodd, 1988: Homogeneous nucleation rate for highly supercooled cirrus cloud droplets. *Journal Of The Atmospheric Sciences*, **45,** 1357-1369.

Sassen, K. and J. D. Horel, 1990: Polarization lidar and synoptic analyses of an unusual volcanic aerosol cloud. *Journal of the Atmospheric Sciences*, **47,** 2881-2889.

Schotland, R. M., K. Sassen, and R. Stone, 1971: Observations by lidar of linear depolarization ratios for hydrometeors. *Journal of Applied Meteorology*, **10,** 1011-1017.

Shaw, G. E., 1975: The vertical distribution of atmospheric aerosols at Barrow, Alaska, *Tellus*, **27**, 39-50.

——, 1976a: Properties of the background aerosols and their effects on climate. *Science***, 192,** 1334-1336.

——, 1976b: Comparison of Arctic and Antarctic haze. *Antarctic Journal of the U.S.*, **11,** 151.

——, 1980: Arctic Haze. *Weatherwise*, **33,** 218-221.

——, 1995: Arctic pollution (in Russian), *Proceedings of the Russian Geographical Society*

Shaw, G. E. and K. Stamnes, 1980: Arctic haze: Perturbations of the polar radiation budget. *Annals of the New York Academy of Sciences*, **338,** 533-39.

Spinhirne, J. D., 1993: Micropulse Lidar. *IEEE Transactions on Geoscience and Remote Sensing*, **31,** 48-55.

Spinhirne, J. D., J. A. R. Rall, and V.S. Scott, 1995: Compact Eye Safe Lidar Systems, *Review of Laser Engineering,* **23**, 112-118.

Stohl, A., 1998: Computation, accuracy and applications of trajectories - A review and bibliography. *Atmospheric Environment*, **32,** 947-966.

Stohl, A., S. Eckhardt, C. Forster, P. James, N. Spichtinger, and P. Seibert, 2002: A replacement for simple back trajectory calculations in the interpretation of

atmospheric trace substance measurements. *Atmospheric Environment*, **36,** 4635-4648.

Stonehouse, B., 1986: *Arctic Air Pollution*. *Studies in Polar Research*, Cambridge University Press.

Twomey, S. A., M. Piepgrass, and T. Wolfe, 1984: An Assesment of the Impact of Pollution on Global Cloud Albedo. *Tellus Series B-Chemical And Physical Meteorology*, **36,** 356-366.

Weitkamp, C., 2005: *Lidar: Range-Resolved Optical Remote Sensing of the Atmosphere*. *Springer Series in Optical Sciences*, Springer, 460 pp.

Welton, E. J. and J. R. Campbell, 2002: Micropulse lidar signals: Uncertainty analysis. *Journal of Atmospheric and Oceanic Technology*, **19,** 2089-2094.

Welton, E. J., K. J. Voss, H. R. Gordon, H. Maring, A. Smirnov, B. Holben, B. Schmid, J. M. Livingston, P. B. Russell, P. A. Durkee, P. Formenti, and M. O. Andreae, 2000: Ground-based lidar measurements of aerosols during ACE-2: instrument description, results, and comparisons with other ground-based and airborne measurements. *Tellus Series B-Chemical And Physical Meteorology*, **52,** 636-651.

Whitby, K. T., 1978: The physical characteristics of sulfur aerosols. *Atmospheric Environment*, **12**, 135–159.